

Experiments and modelling for by-pass pigging of pipelines

Hendrix, Maurice

DOI

[10.4233/uuid:3b3856c6-9eac-4599-be8b-b64fe73e5a5a](https://doi.org/10.4233/uuid:3b3856c6-9eac-4599-be8b-b64fe73e5a5a)

Publication date

2020

Document Version

Final published version

Citation (APA)

Hendrix, M. (2020). *Experiments and modelling for by-pass pigging of pipelines*. [Dissertation (TU Delft), Delft University of Technology]. <https://doi.org/10.4233/uuid:3b3856c6-9eac-4599-be8b-b64fe73e5a5a>

Important note

To cite this publication, please use the final published version (if applicable).
Please check the document version above.

Copyright

Other than for strictly personal use, it is not permitted to download, forward or distribute the text or part of it, without the consent of the author(s) and/or copyright holder(s), unless the work is under an open content license such as Creative Commons.

Takedown policy

Please contact us and provide details if you believe this document breaches copyrights.
We will remove access to the work immediately and investigate your claim.

M.H.W. HENDRIX

EXPERIMENTS AND MODELLING FOR BY-PASS PIGGING OF
PIPELINES

**EXPERIMENTS AND MODELLING FOR BY-PASS
PIGGING OF PIPELINES**

PROEFSCHRIFT

ter verkrijging van de graad van doctor
aan de Technische Universiteit Delft,
op gezag van de Rector Magnificus prof. dr. ir. T.H.J.J. van der Hagen,
voorzitter van het College voor Promoties,
in het openbaar te verdedigen op vrijdag 31 januari 2020 om 12:30 uur

door

Maurice Hans Willem HENDRIX

Ingenieur Technische Natuurkunde
geboren te Helmond, Nederland.

Dit proefschrift is goedgekeurd door de promotors:

prof. dr. ir. R.A.W.M. Henkes

dr. ir. W.-P. Breugem

Samenstelling promotiecommissie:

Rector Magnificus voorzitter

prof. dr. ir. R.A.W.M. Henkes Technische Universiteit Delft

dr. ir. W.-P. Breugem Technische Universiteit Delft

Onafhankelijke leden:

prof. dr. O.J. Nydal NTNU, Trondheim, Norway

prof. dr. ir. C.H. Venner Universiteit Twente

prof. dr. ir. E. H. van Brummelen Technische Universiteit Eindhoven

prof. dr. ir. C. Vuik Technische Universiteit Delft

prof. dr. ir. C. Poelma Technische Universiteit Delft

This research was supported by Shell Projects & Technology.

Cover by: Zoltan Korai

Printed by: Gildeprint - Enschede

Copyright © 2020 by M.H.W. Hendrix, all rights reserved

ISBN 978-94-64020-56-4

An electronic version of this dissertation is available at

<http://repository.tudelft.nl/>.

CONTENTS

SUMMARY	ix
SAMENVATTING	xi
1 INTRODUCTION	1
1.1 Multiphase flow transport in pipelines	2
1.2 A brief history of pipelines and pigs	4
1.3 Pig types	5
1.4 Piggings simulations	7
1.5 Research questions	9
2 CHARACTERIZATION OF THE PRESSURE LOSS COEFFICIENT USING A BUILD- ING BLOCK APPROACH	13
2.1 Introduction	14
2.2 Building block approach	17
2.2.1 Disk pig	18
2.2.2 Speed controlled pig	19
2.3 Numerical setup	20
2.4 Results	21
2.4.1 Disk pig	23
2.4.2 Parameter study	26
2.4.3 Speed controlled pig	28
2.5 Conclusions	30
3 FRICTIONAL FORCES FOR DISC-TYPE PIGGING OF PIPELINES	33
3.1 Introduction	34
3.2 Methods	37
3.2.1 Static pig pull facility	39
3.2.2 Dynamic pig pull facility	44
3.2.3 Measurement procedure	44
3.2.4 Finite Element Model	46
3.3 Results	47
3.3.1 Shape comparison	48
3.3.2 Parameter study	50
3.3.3 Results from dynamic pig pull experiments	53
3.3.4 Relation between static and dynamic results	58
3.4 Conclusions	60
4 EXPERIMENTS AND MODELLING OF BY-PASS PIGGING UNDER LOW PRES- SURE CONDITIONS	63
4.1 Introduction	64

4.2	Models	66
4.2.1	Simplified model	68
4.2.2	Full numerical model	71
4.3	Experimental setup	72
4.4	Results	75
4.4.1	Overall behaviour	76
4.4.2	Local behaviour	79
4.4.3	Control	83
4.5	Conclusions	87
5	ANALYSIS OF TIME INTEGRATION METHODS FOR THE COMPRESSIBLE TWO- FLUID MODEL	89
5.1	Introduction	90
5.2	Governing equations and characteristics	91
5.2.1	Compressible two-fluid model	91
5.2.2	Characteristics	92
5.2.3	Stability	93
5.2.4	Flow pattern map	94
5.3	Spatial and temporal discretization	96
5.3.1	Finite volume method on a staggered grid	96
5.3.2	Temporal discretization	98
5.4	Von Neumann analysis on the fully discrete equations	99
5.4.1	Introduction	99
5.4.2	Extension to BDF2 and Crank-Nicolson	101
5.4.3	Amplification factor from simulation data	102
5.5	Results for various test cases	103
5.5.1	Kelvin-Helmholtz: linear wave growth	104
5.5.2	Kelvin-Helmholtz: nonlinear wave growth	107
5.6	Conclusions	111
6	MODELLING OF BY-PASS PIGGING IN TWO-PHASE STRATIFIED PIPE FLOW	113
6.1	Introduction	114
6.2	Numerical method	115
6.2.1	Spatial discretization	116
6.2.2	Regridding	117
6.2.3	Boundary conditions	119
6.3	Pig motion	122
6.3.1	A smooth function for the pig friction with the pipe wall	123
6.4	Test cases	125
6.4.1	Pig-generated slug for pigs without by-pass	125
6.4.2	Pig-generated slug for pigs with by-pass	128
6.5	Conclusions	131

7	CLOSURE	133
7.1	Conclusions	134
7.1.1	Pressure loss due to by-passing fluid	134
7.1.2	Friction between the pig and the pipe wall	135
7.1.3	Lab-scale pigging experiments	136
7.1.4	Numerical method for the 1D two-fluid model	136
7.1.5	Pig simulation with the 1D two-fluid model	137
7.2	Recommendations for further research	137
7.2.1	Numerical simulations	137
7.2.2	Lab experiments and field data	138
7.2.3	Implementation of new results	139
A	TWO SOLUTION REGION	141
B	MATERIAL TESTS	143
C	DERIVATION OF AN ANALYTIC SOLUTION TO THE SIMPLIFIED MODEL	147
D	TWO-FLUID MODEL DETAILS	149
D.1	Geometry	149
D.2	Friction models	150
	REFERENCES	151
	ACKNOWLEDGMENTS	159
	CURRICULUM VITÆ	161
	LIST OF PUBLICATIONS	163

SUMMARY

The maintenance of pipelines for the production of oil or gas is usually done with a pig (Pipeline Inspection Gauge), which is a cylindrical device that just fits the pipe and propagates through the pipe along with the transport of fluids. While a conventional pig completely seals the pipeline and travels with the same velocity as the production fluids, a by-pass pig has an opening which allows the fluids to partially by-pass the pig. The purpose of the present study is to get a better understanding of the physics of the pigging of a pipeline with multiphase flow transport. The focus is on pigs with by-pass.

An important factor in determining the ultimate travel velocity of a by-pass pig is the pressure drop over the by-pass pig, which is characterized by a pressure loss coefficient. We investigate the pressure loss coefficient of three frequently used by-pass pig geometries in a single phase pipeline with Computational Fluid Dynamics (CFD). We present a building block approach for systematic modelling of the pressure loss through the by-pass pigs, which takes the geometry and size of the by-pass opening into account. The CFD results are used to validate the simple building block approach for systematic modelling of the pressure loss through a by-pass pig. It is shown that the models for the pressure loss closely resemble the CFD results for each of the three pig geometries.

In addition to the pressure loss coefficient, we investigate the frictional force which is acting between the pig and the pipe wall. Two complementary experimental setups have been designed and used to study the sealing disc of a pig, which is responsible for the frictional force between the pig and the pipe wall. Six 12'' standard sealing discs from two different vendors have been used. The first setup is a static setup in which the sealing disc is subjected to a normal wall force and a tangential friction force. A unique feature of the setup is that the ratio between the friction force and the wall force can be readily adjusted. This allows to experimentally determine the force ratio which is directly related to the Coulomb friction coefficient, which is often a difficult parameter to predict. Furthermore, the static setup is used to systematically study the effect of oversize, thickness, and Young's modulus of the sealing disc on the frictional force. A direct comparison with Finite Element (FE) calculations is made. The second experimental facility consists of a dynamic setup in which a sealing disc is pulled through a vertical 1.7 m long pipe. The effect of possible lubrication on the frictional force is studied by applying water to the sliding contact and comparing the results with dry pull tests for different sliding velocities. The corresponding difference in the Coulomb friction coefficient was quantified using FE calculations, which were successfully verified with the static setup. The sensitivity of possible wear of the sealing disc on the frictional force was also considered.

Furthermore, we have obtained experimental and numerical results for by-pass pigging under low-pressure conditions. These are meant to help the design of a speed-controlled

pig; this is a pig in which the by-pass area is controlled during its propagation to maintain a desired velocity. Our study was carried out using air as working fluid at atmospheric pressure in a 52 mm diameter pipe with a length of 62 m. The experimental results have been used to validate simplified 1D models commonly used in the oil and gas industry to model transient pig behaviour. Due to the low-pressure conditions oscillatory behaviour is observed in the pig speed, which results in high pig velocity excursions. The oscillatory motion is described with a simplified model which is used to design a simple controller aimed at minimizing these oscillations. The controller relies on dynamically adjusting the by-pass area, which allows to release part of the excess pressure which builds up in the gas pocket upstream of the pig when the motion of the pig is arrested. Subsequently, the control algorithm is tested by a 1D transient numerical model, which was shown to successfully reduce the pig velocity excursions.

In order to accurately solve the time dependent 1D two-fluid equations for multiphase flow in pipelines, either with or without a pig, different time integration schemes have been investigated. The BDF2 method (Backward Differentiation Formula using 2 levels) is proposed as the preferred method to simulate transient compressible multiphase flow in pipelines. Compared to the prevailing Backward Euler method, the BDF2 scheme has a significantly better accuracy (second order) while retaining the important property of unconditional linear stability (A-stability). In addition, it is capable of damping unresolved frequencies such as acoustic waves present in the compressible model (L-stability), opposite to the commonly used Crank–Nicolson method. A method for performing an automatic von Neumann stability analysis is proposed that obtains the growth rate of the discretization methods without requiring symbolic manipulations and that can be applied without detailed knowledge of the source code. The strong performance of BDF2 is illustrated via several test cases related to the Kelvin–Helmholtz instability. A novel concept called Discrete Flow Pattern Map (DFPM) is introduced, which describes the effective well-posed unstable flow regime as determined by the discretization method. BDF2 accurately identifies the stability boundary, and reveals that in the nonlinear regime ill-posedness can occur when starting from well-posed unstable solutions. The well-posed unstable regime obtained in nonlinear simulations is therefore in practice much smaller than the theoretical one, which might severely limit the application of the two-fluid model for simulating the transition from stratified flow to slug flow.

The 1D code has been subsequently extended to model the propagation of a by-pass pig in a two-phase pipeline. The liquid slug that is accumulated in front of the pig, the so-called pig-generated slug, has been modelled and characterized. Under the assumption of a stratified flow, the academic case of liquid slug accumulation where we neglect the viscosity of the fluids has been analyzed. We also consider the more realistic case that includes the viscosity of the fluid. Finally, the effect of the presence of a by-pass in the pig on the accumulated liquid slug is investigated and compared to a simplified model.

SAMENVATTING

Voor het onderhoud van pijpleidingen in de olie- en gasindustrie wordt normaliter gebruik gemaakt van een pig (pipeline inspection gauge), een cilindrisch instrument dat exact in de pijpleiding past en door de pijpleiding heen gaat samen met de productie van gas en/of vloeistoffen. In tegenstelling tot de conventionele pig – die de pijpleiding compleet afsluit en voortbeweegt met dezelfde snelheid als de geproduceerde gas/vloeistoffen – heeft een by-pass pig een opening die het mogelijk maakt om een deel van het gas of de vloeistof door de by-pass heen te laten stromen. Het doel van het huidige onderzoek is om een beter inzicht te krijgen in de fysica van het piggen van een pijpleiding in een meergefasenstroming, waarbij de nadruk van het onderzoek ligt op pigs met een by-pass.

Een belangrijke factor voor het bepalen van de uiteindelijke voortbewegingssnelheid van de by-pass pig is de drukval over de by-pass pig, die gekarakteriseerd wordt door de drukvalcoëfficiënt. We onderzoeken de drukvalcoëfficiënt voor drie veelgebruikte by-pass geometrieën in een één-fasepijpleiding door gebruik te maken van Computational Fluid Dynamics (CFD). We presenteren een modulair opgebouwd systematisch model van de drukval over de by-pass pig, dat rekening houdt met de geometrie en afmeting van de opening van de by-pass. De CFD-resultaten worden gebruikt om de eenvoudige, modulaire aanpak voor het systematisch modelleren van de drukval over de by-pass pig te valideren. Er wordt aangetoond dat de modellen voor de drukval goed overeenkomen met de CFD-resultaten van elk van de drie by-passgeometrieën.

Naast de drukvalcoëfficiënt doen we ook onderzoek naar de wrijvingskracht tussen de pig en de pijpwand. Hiervoor zijn twee complementaire experimentele opstellingen ontworpen om de afsluitschijf van de pig, die verantwoordelijk is voor de wrijvingskracht tussen de pig en de pijpwand, te bestuderen. Hierbij is gebruik gemaakt van een zestal standaard 12'' afsluitschijven, afkomstig van twee verschillende leveranciers. De eerste experimentele opstelling is een statische opstelling, waarbij de afsluitschijf van de pig is onderworpen aan een normale wandkracht en een tangentiële wrijvingskracht. Een uniek kenmerk van deze opstelling is de mogelijkheid om de verhouding tussen de wrijvingskracht en de wandkracht eenvoudig bij te stellen. Dit maakt het mogelijk om experimenteel de krachtenverhouding te bepalen welke direct gerelateerd is aan de Coulomb wrijvingscoëfficiënt – een parameter die normaliter lastig te voorspellen is. Verder wordt de statische opstelling gebruikt om op systematische wijze het effect van de overmaat, dikte en Young's modulus van de afsluitschijf op de wrijvingskracht te bestuderen. Hierbij wordt een directe vergelijking met eindige elementen berekeningen gemaakt. De tweede experimentele opstelling is een dynamische opstelling, waarbij de afsluitschijf door een pijpleiding (met een lengte van 1.7 m) wordt getrokken. Het effect van mogelijke smering op de wrijvingskracht is bestudeerd door water aan te brengen op het schuivende contact

en door de testresultaten te vergelijken met de droge trekproef voor verschillende treksnelheden. Het gevonden verschil in de Coulombwrijving is gekwantificeerd door gebruik te maken van de eindige elementen berekeningen, die succesvol waren geverifieerd door de statische opstelling. Hierbij is de gevoeligheid van mogelijke slijtage van de afsluitschijf op de wrijvingskracht ook in beschouwing genomen.

Verder hebben we experimentele en numerieke resultaten voor by-pass pigging onder lagedrukcondities verkregen. Deze resultaten zijn bedoeld om te helpen bij het ontwerp van een pig met snelheidsregeling; dit is een pig waarbij de opening van de by-pass geregeld wordt gedurende de voortbeweging door de pijpleiding om een gewenste snelheid te blijven houden. De studie is uitgevoerd met lucht op atmosferische druk in een pijpleiding met een diameter van 52 mm en een lengte van 62 m. De experimentele resultaten zijn gebruikt voor het valideren van vereenvoudigde 1D-modellen die typisch in de olie- en gasindustrie gebruikt worden. Door de lagedrukcondities wordt een oscillerend gedrag van de pigsnelheid waargenomen, wat resulteert in uitschieters in pigsnelheid. De oscillerende beweging is beschreven door middel van een vereenvoudigd model dat gebruik maakt van een simpele regelaar gericht op het verminderen van deze oscillaties. De regelaar zorgt voor de dynamische aanpassing van de by-passopening, waarbij een deel van de opgebouwde overdruk in het gas aan de stroomopwaartse zijde van de pig kan worden vrijgelaten. Vervolgens is het regelalgoritme getoetst door middel van een tijdsafhankelijk 1D numeriek model, waarbij is aangetoond dat dit algoritme met succes de uitschieters in de pigsnelheid kan verminderen.

Om de tijdsafhankelijke 1D vergelijkingen voor twee fluida bij meergefasenstroming in pijpleidingen op te lossen, zowel met als zonder pig, zijn er verschillende tijdsintegratieschema's onderzocht. De BDF2-methode (Backward Differentiation Formula, gebruikmakende van 2 niveaus) is voorgesteld als de voorkeursmethode om de dynamische compressibele meergefasenstroming in pijpleidingen te simuleren. In vergelijking met de gangbare Backward-Euler methode heeft het BFD2-schema een aanzienlijk betere nauwkeurigheid (tweede orde) terwijl dit schema het belangrijke kenmerk van onvoorwaardelijke lineaire stabiliteit (A-stabiliteit) behoudt. Ook is het schema, in tegenstelling tot de veelgebruikte Cranck-Nicolson methode, in staat om onopgeloste frequenties, zoals geluidsgolven in het compressibele model (L-stabiliteit), te dempen. Een methode voor het uitvoeren van een automatische von Neumann-stabiliteitsanalyse is voorgesteld, waarbij het groeipercentage van de discretisatiemethode wordt gevonden zonder dat symbolische manipulaties zijn vereist. Deze methode kan worden toegepast zonder gedetailleerde kennis van de broncode. De sterke prestatie van BFD2 is gedemonstreerd door middel van verschillende simulaties gerelateerd aan de Kelvin-Helmholtz instabiliteit. Een nieuw concept genaamd Discrete Flow Pattern Map (DFPM) is geïntroduceerd, dat het effectieve goedgestelde onstabiele stromingsregime beschrijft zoals bepaald door de discretisatiemethode. BDF2 geeft een nauwkeurige bepaling van de stabiliteitsgrens en laat zien dat in het niet-lineaire regime slechtgesteldheid kan optreden wanneer gestart wordt vanuit goedgestelde onstabiele oplossingen. Het goedgestelde onstabiele regime in niet-lineaire simu-

laties is om die reden in de praktijk vele malen kleiner dan het theoretische regime, hetgeen de toepassing van het twee fluida model voor de simulatie van de gelaagde stroming naar zogenaamde "slug" stroming mogelijk ernstig beperkt.

De 1D code is vervolgens uitgebreid om de voortbeweging van een by-pass pig in een tweefasenpijpleiding te modelleren. De vloeistof die zich ophoopt voor de pig, de zogenoemde pig-gegenereerde slug, is gemodelleerd en gekarakteriseerd. Met de aanname van een gelaagde stroming is de academische casus geanalyseerd van de vloeistofophoping onder verwaarlozing van wrijving. We hebben ook de meer realistische casus, die rekening houdt met wrijving, in beschouwing genomen. Tenslotte is het effect van de aanwezigheid van een by-pass in de pig op de vloeistofophoping onderzocht en vergeleken met een vereenvoudigd model.

INTRODUCTION

1.1 MULTIPHASE FLOW TRANSPORT IN PIPELINES

Onshore or offshore pipelines provide an economic solution to the transport of fluids in the oil and gas industry. Offshore pipelines can transport the fluids from the reservoir and well to an offshore production platform or to an onshore separator or slug catcher. Particularly gas-condensate pipelines (or trunklines) can have a large diameter (typically 30'' to 42'') and they can be long, with existing examples between 100 and 200 km [15]. Depending on the gas production rate, significant amounts of condensate and water can accumulate in the pipeline (so-called liquid holdup). Therefore, the flow through these pipelines is typically characterized as multiphase flow. This means that gas, oil (or condensate), and water (possibly accompanied by solids) are transported simultaneously through the same pipeline.

Pipelines need regular maintenance. This is often by the use of so-called pigs. A pig (the term is sometimes seen as an abbreviation for Pipeline Inspection Gauge) is a device that is launched at the inlet of the pipeline and is received back in the pig trap, located at the outlet of the pipeline. The pig is propelled by the production fluids that are transported in the pipe. The pig can serve multiple maintenance purposes, which include: cleaning the inner pipe wall, removing liquids, distribution of corrosion inhibitor along the pipe wall, and pipe wall inspection. Figure 1.1a shows a schematic of a pig inside a multiphase pipeline.

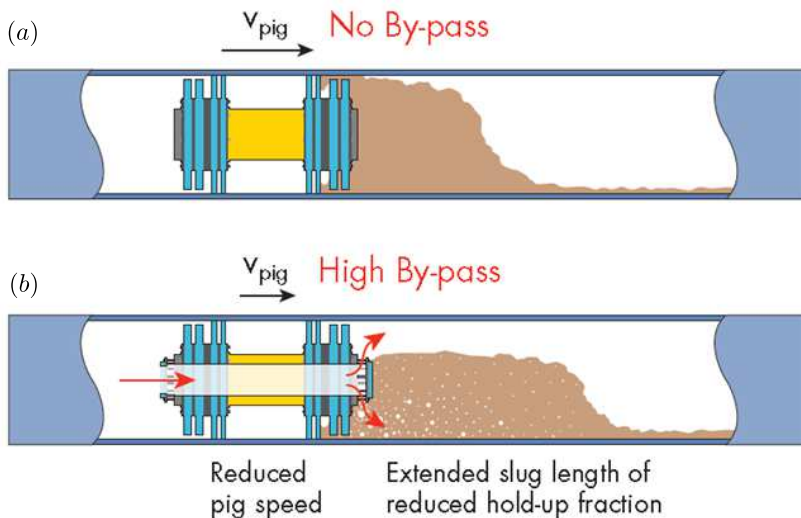


Figure 1.1: (a) Conventional pig. (b) By-pass pig. Adapted from [21].

During the time that the pig resides in the pipeline it collects liquid in front of it, see figure 1.1. This gives the so-called pig-generated volume. When this liquid arrives at the outlet of the pipeline (i.e. just before the pig is received back in the trap), the liquid surge

will be stored in the downstream slug catcher. This pig-generated volume is about equal to the liquid holdup in the pipeline (present at the moment that the pig is launched) minus the product of the normal liquid outflow rate with the pig residence time. As the onshore gas plant requires an uninterrupted supply of gas, a storage unit is needed onshore (downstream of the pipeline and upstream of the plant) to temporarily park the liquid slug. An example of such a slug catcher is given in figure 1.2. The slug catcher consists of an inlet header and splitter, which distribute the liquid over a number of bottles, whereas the gas leaves the bottles at the upstream end through vertical gas legs. Liquid is drained at the downstream liquid header. When a liquid slug arrives, the gas is displaced from the bottles and replaced by liquid. This guarantees uninterrupted supply of gas to the plant. The design of the slug catcher size needs to be such that the pig-generated slug can indeed be stored in the bottles. Therefore the size can easily become as large as 5000 m^3 . These slug catchers can be costly (50 to 150 million dollars) and require a significant plot space.

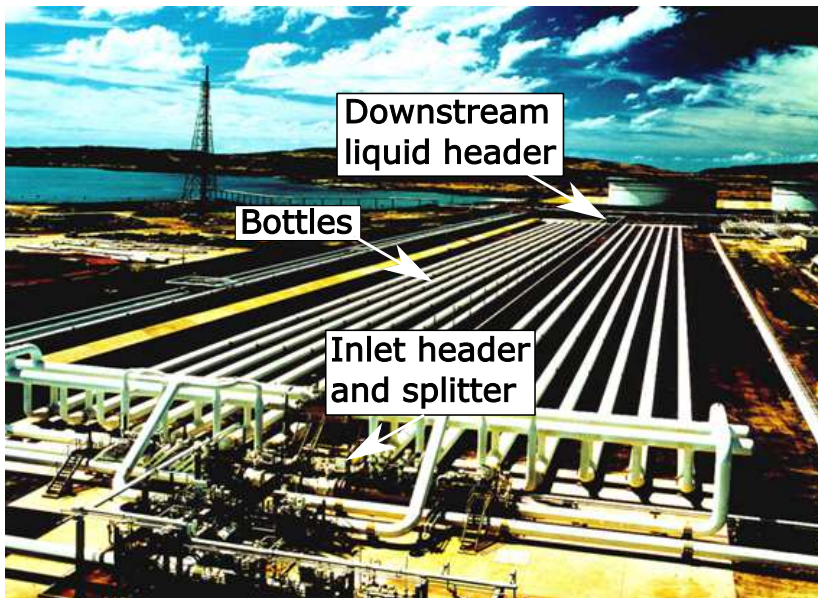


Figure 1.2: Example of a slug catcher with 5000 m^3 liquid storage volume. Adapted from [39].

In an effort to reduce the pig-generated volume, so-called by-pass pigs have been designed. Whereas a conventional pig completely seals the pipeline, a by-pass pig has holes in the pig body which allows the gas to flow through (i.e. by-pass) the pig body. Figure 1.1b shows a schematic of a by-pass pig. As a result of the by-pass, the travel velocity of the by-pass pig will be lower as compared to a conventional pig. The longer residence time of the by-pass pig results in more time to drain the liquid slug from the slug catcher, which will in turn result in a smaller pig-generated volume that needs to be stored in the slug catcher. In addition, the gas which flows through the by-pass pig drags the liquid in front

of the pig, which results in a more elongated liquid slug and thus a smaller pig-generated volume, see figure 1.1b. In the most optimum situation the by-pass area is such large that the pig velocity is equal to the liquid velocity. In that case the pig-generated volume will be reduced to zero. The typical size of the by-pass area ranges up to about 15% of the total cross-sectional area of the pipe.

1.2 A BRIEF HISTORY OF PIPELINES AND PIGS

Pipes have been in use over many centuries. The Egyptians used clay pipes for drainage purposes as early as 4000 B.C. [56]. The Romans used lead and ceramic pipelines in their famous aqueducts more than 2000 years ago. The use of iron pipelines dates back to the 18th century, which were used to transport water and gas. The subsequent advent of steel pipes in the 19th century allowed for much longer pipelines, as the steel could sustain much higher pressures than the iron pipelines. The discovery of oil in Pennsylvania in 1859 was followed by the construction of the first long-distance steel pipeline in 1879. The pipeline had a diameter of 6'' and a length of 109 miles. A major improvement in the construction of steel pipelines occurred in the late 1920s with the introduction of electric arc welding, which allowed for leakproof connections of (large) pipe diameter segments [56]. The pipeline network has since then expanded rapidly in the U.S. and counts a total of 2.23 million kilometer in length and is thereby the most extensive pipeline network of any country in the world [1]. The Netherlands has a total length around 20 thousand kilometer of pipelines [1].

An inevitable consequence of the operation of pipelines that transport large amounts of fluids is appropriate internal maintenance. This was noted shortly after the first oil pipelines were taken into service in the 1870s. Higher pumping pressures and decreased overall efficiency reflected internal flow restriction due to build-up of wax and other debris in the line [17]. The first pigs, which consisted of nothing more than a bundle of rags tied together, were then used and resulted in immediate flow improvement. Later the rags were replaced by bundles of leather which were stronger and could absorb the fluids and thereby swell, which guaranteed a good seal between the pig and the inner pipe wall. Later on pigs were more purposefully built, consisting of a steel body with urethane cups or discs, possibly equipped with brushes and scrapers. In the 1960s the polyurethane foam pig was introduced. Many other industries also adapted the use of foam pigs, including the water and processing industry. From the late 1960s onwards pigs became instrumented with various sensors which can inspect the condition of the inner pipe wall while the pig is travelling through the pipe [17]. These developments have lead to so-called smart (or intelligent) pigs.

It is unclear where the term 'pig' is originating from. As mentioned some people refer to pig as an abbreviation of Pipeline Inspection Gauge [15]. But as pigs were initially not used for inspection purposes, this is unlikely. A more accepted explanation is that the term

pig is attributed to the screeching sound that the pig can make when it moves inside the pipeline [15, 17, 74].

1.3 PIG TYPES

Pigs were originally developed to remove deposits which could obstruct or retard the flow through a pipeline. Today pigs are widely used during all phases in the life of a pipeline for many different reasons in various industries, including water, oil, food, and chemicals. While there are more than 350 different pig types [15], three main categories can be distinguished:

- **Cleaning/maintenance pigs.** These are used to clean the pipeline to ensure continuous flow and maintain operational efficiency or to prepare the pipeline for intelligent inspection.
- **Intelligent inspection tools.** These are used to inspect the pipeline, to provide information on the condition of the line and to assess the extent and location of any integrity concerns.
- **Gel pigs.** These are pumpable liquid gels sealed between two cleaning/maintenance pigs to remove the solid debris or water from the pipeline.

A pig that enters a pipeline is driven forward by the higher pressure of the fluid behind it, which pushes the pig from one end to the other end of the pipeline. During its residence in the pipeline, the pig sweeps out the entire content of the pipeline. Some of the reasons to send a pig through a pipeline are:

- **Corrosion management.** To reduce the corrosion rate of the pipeline, a pig can remove corrosion products, stagnant water, and corrosion causing microbes in the low spots. Pigging can also help to more uniformly distribute the corrosion inhibitor throughout the pipeline, such as to enable wetting of the top pipe wall with corrosion inhibitor in the liquid. When using a by-pass pig for corrosion distribution in wet gas pipelines, one needs to make sure that the flow regime ahead of the pig still gives top-of-line wetting; this is ensured by the liquid slug created ahead of the pig if a standard pig is used (no by-pass), but this will depend on the rate of the by-passing gas flow if a by-pass pig is used.
- **Removal of solids.** These solids can be for example wax or scale sticking to the inside of the pipeline or sand or corrosion products that have accumulated in the pipeline.
- **Removal of liquids.** The build-up of liquid in a pipeline to reach the steady-state liquid hold-up can take days or weeks. By pigging at regular intervals, and thus through

regular liquid removal, one can keep the liquid hold-up below the steady-state equilibrium liquid hold-up, for example to ensure that the liquids in the pipeline can always fit within the slug catcher.

- **Pipeline inspection to determine the integrity.** A pig equipped with special measuring equipment like ultrasonic transducers or Magnetic Flux Leakage (MFL) can determine the integrity of the pipeline by measuring the remaining wall thickness [27].

In a multiphase flow pipeline, gas travels on average faster than liquid. A conventional pig (i.e. a pig without by-pass) travels at the mixture velocity through the pipeline, as no fluid can by-pass the pig. This mixture velocity is in between the gas and liquid velocity. A conventional pig travels thus faster than the liquid. The pig will collect the liquid in front of it as it moves faster than the liquid velocity, see figure 1.1. Behind the pig, there will only be gas present, as liquid is travelling slower than the pig and the liquid is staying behind to re-establish the steady-state liquid hold-up in the pipeline. As explained in section 1.1, a by-pass pig travels at a lower velocity compared to a conventional pig. The by-pass area can be created in various ways. Figure 1.3 shows two examples of a by-pass pig. The first example (figure 1.3a) shows a by-pass pig with a concentric by-pass area in the centre, whereas in the second example (figure 1.3b) a deflector plate is included at the downstream side of the by-pass. The small space between the pig body and the plate creates the by-pass. The main function of the deflector plate is providing a pulling force, which is especially needed when the pig is launched [96].



Figure 1.3: (a) By-pass pig with by-pass in the centre (taken from [53]). (b) By-pass pig with a deflector disc (taken from [96]).

Many other by-pass configurations do exist. The advantage of using a by-pass pig compared to a conventional pig is not only the reduction of the pig-generated volume (as explained in section 1.1). Also for the removal of solids, which may be attached to the wall in liquid pipelines, the use of a by-pass pig can be beneficial: due to the flow through the by-pass liquid jets can emerge, which help to remove the solids from the wall and transport them as a slurry further downstream. The lower travel speed of a by-pass pig is also beneficial for intelligent pigs. The inspection of the pipe wall, which is carried out

by the intelligent pig, is much more accurate at a lower travel speed, and may even be impossible in case no by-pass is present and the pig travels at the mixture velocity. For example, a high velocity of the inspection pig can cause low pipe wall thickness locations to be missed.

Although the advantages of using a by-pass pig are clear, the use of a by-pass pig does not come without any risks. The most important risk is that, due to the by-pass area, not enough differential pressure across the pig is generated and the pig gets stuck in the pipeline. The costs associated with locating and removing a stuck pig in combination with the production deferment caused by such an event are high. This makes the choice of the by-pass area, which needs to be made upfront of carrying out the pigging run, a challenging task. The main uncertainty for calculating the right by-pass opening is the friction between the pig and the pipe wall. To overcome this problem, inspection pigs have been designed that have an *adjustable* by-pass area to regulate the pig speed through the pipeline to a constant velocity [63, 89]. These so-called speed-controlled pigs have an onboard controller, which reacts on the changes in the friction between the pig and the pipe wall along the pipeline, as this leads to a change in the pig velocity. For example, a local increase in friction could cause the pig to slow down. The by-pass opening is then reduced by the control algorithm and as a result the pressure drop across the pig increases and therefore the pig velocity increases as well. Speed-controlled pigs have normally been applied in single-phase pipelines, but there are also some first field applications to use them under multiphase flow conditions. So far speed-controlled by-pass pigging has been mainly found on intelligent pigs in order to improve inspection quality. But there is a potential to apply similar technology to other pig types as well.

1.4 PIGGING SIMULATIONS

As explained in the previous section, it is important to have a proper design of the pigging operation before carrying out the actual pigging run. Some typical questions that could be addressed during such a design phase are:

- What will be the additional pressure drop in the pipeline as a result of the presence of a pig?
- What will be the size of the pig-generated liquid slug, and at what time will it arrive at the slug catcher?
- What is the optimal size of the by-pass area?
- At what travel speed will the pig traverse the pipeline?

In almost all cases the most important question is: Will the pig arrive at the outlet of the pipe at all? In an attempt to answer these questions the industry uses various simplified models. We will outline a few of the existing modelling approaches below.

In order to estimate the friction of the pig with the pipe wall (or equivalently: the driving differential pressure that is needed to overcome the frictional force), the following empirical relationship has been proposed by Cordell [14]: $\Delta P_{\text{pig}}(\text{bar}) = \frac{K}{D_{\text{nom}}(\text{in})}$. Here ΔP_{pig} is the required differential pressure (in bar unit) needed to drive the pig, D_{nom} is the nominal pipeline diameter (in inch unit), and K is an empirical constant. Figure 1.4 depicts different K -values for different pig types. For example: a value of $K = 1$ corresponds to a foam pig, a value of $K = 19$ corresponds to an ultrasonic technique in line inspection tool, whereas $K = 24$ would correspond to a magnetic flux leakage (MFL) in line inspection tool. It is clear that the K -values are indicative only. Many pigs have a sealing disc that guarantees a tight seal between the pig and the inner pipe wall, see figure 1.3b. It is this sealing disc that is responsible for the frictional force. No information on the material properties nor on the size of the sealing disc is present in the aforementioned model.

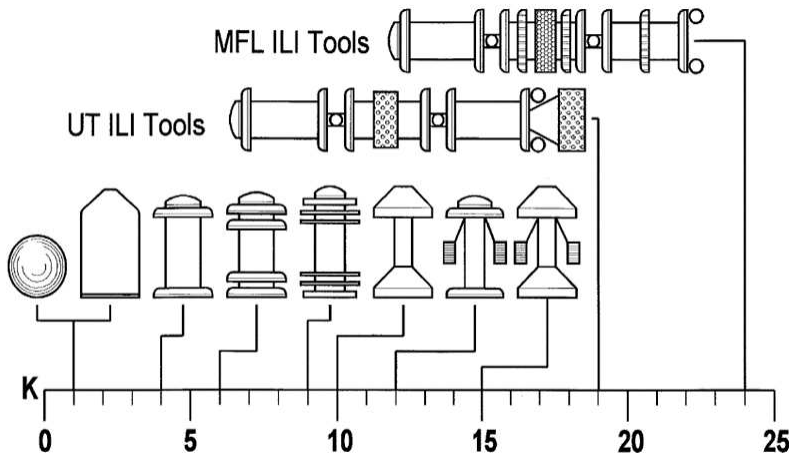


Figure 1.4: Proportionality factor to calculate the differential pressure that is required to drive various types of pigs. Adapted from [14].

In many cases the precise value of the friction is not very important for conventional pigs (i.e. no by-pass) as usually the pressure drop across the pig (a few bar maximum) is much smaller than the total pressure drop along the pipeline. However, when a by-pass pig is used it is an important factor, as the pressure drop that is generated as a result of the by-passing fluids must overcome the frictional force. When the by-pass is too large not enough pressure drop is generated, and the pig stalls. It is this balance between the driving pressure force and the frictional force that ultimately determines the travel velocity of a by-pass pig. Not many models exist for predicting the pressure drop due to the by-passing fluids across a by-pass pig, and often a simple geometry, like the one presented in figure 1.3a, is assumed [68, 82].

In order to model the pig trajectory through the pipe, the industry frequently uses one-dimensional transient pipeline models to simulate the multiphase flow with the pigging operation. Two examples of commercial simulation tools are OLGA [8] and LedaFlow [28]. These tools solve the conservation equations for mass, momentum, and energy for each of the phases. The equations have been averaged over the cross-sectional area of the pipeline, which means that the 3D spatial equations are converted into 1D spatial equations. The averaging leads to closure relations for the wall friction and for the interfacial stress between the phases. The 1D models also include empirical correlations for the different multiphase flow regimes (e.g. stratified flow, hydrodynamic slug flow, bubbly flow, or annular dispersed flow). The pipeline is split up in a number of spatial grid cells, and a numerical time step has to be chosen. The propagation of the pig can also be simulated with these 1D tools. User input is required for the friction between the pig and the pipe wall (both for conventional pigs and for by-pass pigs) and for the pressure loss due to by-passing fluid (for the case with by-pass pigs). The precise details on how the conservation equations are numerically solved, as well as how the fluid-pig interaction is handled, are proprietary to the vendors of these commercial tools. Academic codes do exist, but are often limited to single-phase flow. Only a few consider two-phase flow [47, 50, 61, 97], but among those only a pig without by-pass is considered.

1.5 RESEARCH QUESTIONS

The purpose of the present PhD project is to get a better fundamental understanding of the physics of pigging of a pipeline with multiphase flow transport in order to improve engineering models used in the industry for pigging operations. Although pigs have been used for decades in the industry, by-pass pigs are relatively new, and the use of pigs with speed control has emerged just recently. As explained, many empirical relations exist but some fundamental knowledge about the physics is lacking. The emphasis in our research will be on by-pass pigs, either without or with speed control. The results can be used for implementation in the engineering design tools that are used to prepare a pigging operation. In this way a better design can be made for by-pass pigs, either without or with speed control. This reduces the risk that something will go wrong with the actual operation of the pig, such as serious oscillations in the pig movement or a stalled pig. In case of speed-controlled by-pass pigs this will also help to determine the range of the by-pass opening that should be available for control. The reduced, or eliminated, operational risks of by-pass pigging will help to safely reduce the size of the required slug catcher that would be required for conventional pigging.

The focus will be on various aspects which are important for the motion of a by-pass pig in a single phase or multiphase pipeline:

1. **Fluid flow aspects.** The flow will be calculated with both a 1D approach, using a newly developed numerical-physical model, and with 2D and 3D Computational

Fluid Dynamics (using the existing third-party tool Fluent). Lab experiments were carried out in the water/air flow loop at the Delft University of Technology.

2. **Friction between the pig and the pipe wall.** Finite element simulations were carried out for the deformation of the oversized discs that are part of the by-pass pig configuration. Also pull tests with such discs were carried out in a newly built set-up at the Shell Technology Centre Amsterdam (STCA).
3. **Control of the by-pass opening to obtain the desired pig velocity.** Some small-scale tests with pigs were carried out in the water/air flow loop at the Delft University of Technology. In parallel simulations were carried out with the 1D model.

The results of the study are described in 5 technical chapters. These chapters are based on publications that appeared either in conference proceedings or in journals.

Chapter 2. CFD simulations with Fluent to obtain the pressure loss coefficient for the by-pass fluid through the by-pass area. The effect of different by-pass configurations is studied in single phase flow. The work was carried with the support of two Master students [4, 54], and the work was presented at a conference and published in a journal [5, 35].

Chapter 3. Experiments and modelling for the friction between the pig and the wall. The work was carried out with the support from two Master students [29, 32]. This included experiments at STCA (both steady state and dynamic pull tests, with dry gas, and with lubrication using water and air). The forces and disc deformation as measured were compared with Finite Element simulations for the stresses and deformations. The results were presented at a conference and published in a journal [34, 58].

Chapter 4. Lab experiments in water/air 2", 130 m flow loop at the Delft University of Technology. The work was carried out with the support from a Master student [44] and from a team of 4 undergraduate students. The pressure drop over the pig and its velocity were measured using air only at atmospheric pressure. Various configurations (without and with by-pass) were measured, and the observed slip-stick behaviour (that is typical for low pressure pigging) was reproduced with a simple analytical model. The results were presented at a conference and published in a journal [36, 37].

Chapter 5. Numerical modelling of two-phase pipe flow (still without the presence of a pig). An accurate spatial and temporal finite volume scheme to solve the 1D two-fluid model was developed and tested in Matlab. Simulations were carried out for the stability of stratified gas-liquid flow. The growth of roll waves and slugs was simulated. A numerical flow pattern map could be established. Part of the results have been published in a journal [80].

Chapter 6. Numerical modelling of pigs with the help of an accurate two-fluid model. Thereto the newly developed finite volume code was extended with the propagation of pigs. The results from the other parts of the study (such as the pressure loss coefficient determined with CFD for the by-passing fluid, and the friction between the pig and the pipe wall) were used as input correlations to the pigging model in the 1D numerical model. The results have been published at a conference [38].

2

CHARACTERIZATION OF THE PRESSURE LOSS COEFFICIENT USING A BUILDING BLOCK APPROACH

This chapter is adopted from M. H. W. Hendrix, X. Liang, W.-P. Breugem, and R. A. W. M. Henkes, "Characterization of the pressure loss coefficient using a building block approach with application to by-pass pigs". In: *Journal of Petroleum Science and Engineering* 150 (2017), pp. 13-21.

2.1 INTRODUCTION

In the oil and gas industry, pipeline networks are used to transport production fluids from wells to production plants. During normal operation, these pipelines need regular cleaning and inspection. Ideally, this pipeline maintenance should interrupt the production as little as possible. Typically, pipeline maintenance is done with a pig (Pipeline Inspection Gauge). This is a cylindrical or spherical device that is launched at the inlet of the pipe and subsequently travels through the pipeline while being propelled by the production of fluids. The pig is trapped in a receiver at the end of the pipeline. While a conventional pig completely seals the pipeline and travels with the same velocity as the production fluids, a by-pass pig has an opening hole which allows the production fluids to partially flow through the pig body. Figure 2.1a shows an example of a by-pass pig. A by-pass pig will typically travel with a lower pig velocity compared to a conventional pig that completely seals the pipeline, as the velocity of the by-pass pig is not dictated by the velocity of the production fluids anymore, but depends on the overall force balance for the pig. In steady state this means that the driving pressure force F_p of the production fluids balances with the frictional force F_{fric} of the pig with the pipe wall, see figure 2.1b. The driving pressure force F_p depends on the pressure drop Δp over the pig and is expressed as $F_p = \Delta p A_{pig}$, where A_{pig} is the frontal area of the pig (which is equal to the cross sectional area of the pipe).

The reduction of the pig velocity has proven to be beneficial for both inspection and cleaning purposes [63, 96]. In addition, a lower pig velocity is necessary for safe operation, as a too high pig velocity may damage the insides of the pipe or the pig itself. As the travel velocity of the by-pass pig is important for the efficiency and safety of the pigging operation, detailed knowledge of the pressure drop Δp over the pig is needed in order to predict its velocity. This study focuses on quantifying the pressure drop Δp over various types of by-pass pigs which is characterized by a pressure loss coefficient K , defined as:

$$K = \frac{\Delta P}{\frac{1}{2} \rho U_{bp}^2}, \quad (2.1)$$

where ρ is the density of the fluid and U_{bp} is the fluid velocity in the horizontal by-pass region relative to the pig motion, see figure 2.1. The pressure loss coefficient K depends on the size of the by-pass opening as well as on the design of the by-pass geometry, which may vary depending on the application of the pig. A good description of K is not only important for a steady state calculation of the pig velocity, but is also a relevant input parameter for 1D transient tools. Examples include 1D codes which are described in [22, 47, 69, 91] and commercial tools such as OLGA [8] or LedaFlow [28], which are commonly used in the oil and gas industry. In these transient tools the trajectory of the pig through a pipeline can be monitored, and a relation for K needs to be known in advance. So far reliable correlations for K are missing, and the present study is aimed at providing one.

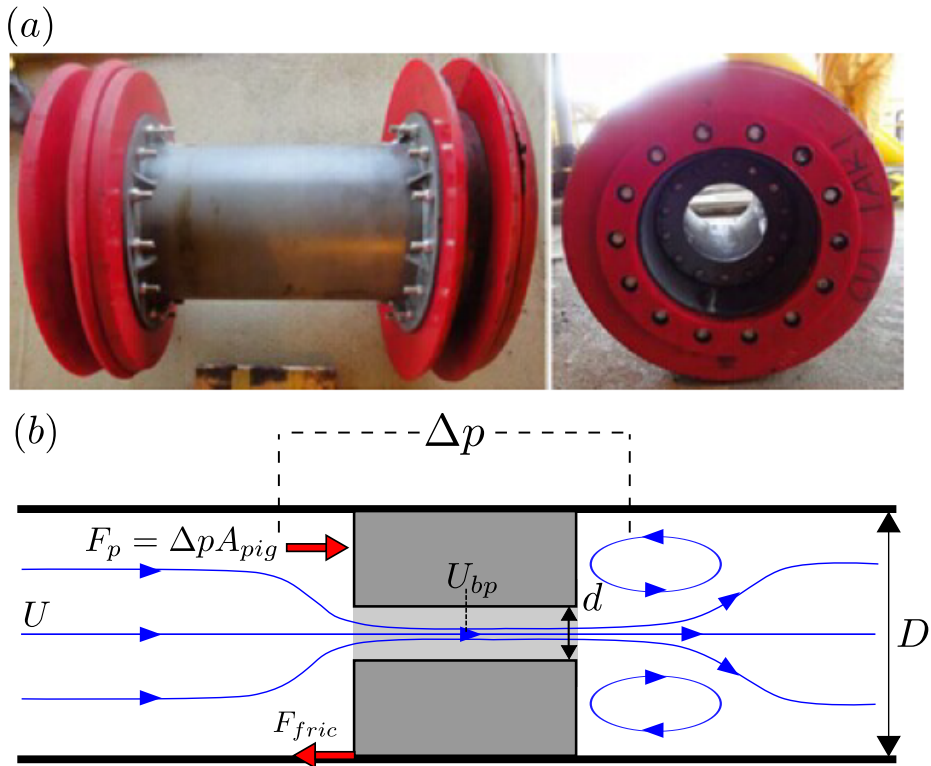


Figure 2.1: (a) A bi-directional by-pass pig, taken from [53]. (b) A schematic of the forces on a by-pass pig in a horizontal pipeline. In steady state the driving force F_p due to the by-passing fluids is balanced by the frictional force F_{fric} of the pig with the pipe wall. In this schematic D indicates the pipe diameter, d the diameter of the by-pass hole, U the upstream bulk velocity, and U_{pig} the pig velocity.

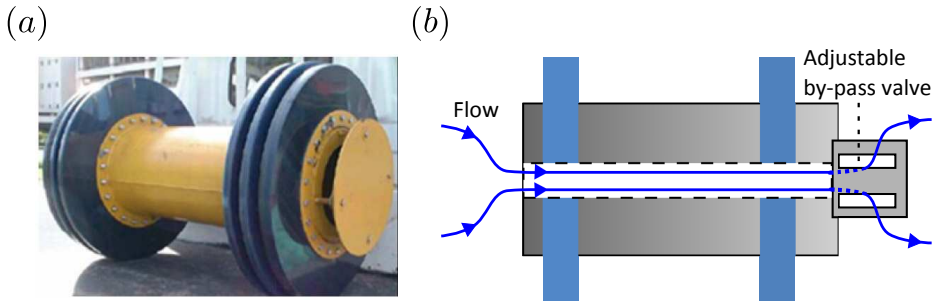


Figure 2.2: (a) A by-pass pig with a deflector disk, taken from [96]. (b) Schematic of a by-pass pig with speed control. The by-pass valve can be adjusted to regulate the by-pass area.

As the geometry of a pig varies depending on its application, a building block approach is used in order to provide a general framework for determining the corresponding pressure loss coefficient. The building block approach relies on a geometrical decomposition of the by-pass pig, and accounts for the contribution of the individual components of the by-pass pig geometry to the overall pressure loss. It is thus assumed that the flow patterns are uncorrelated between building blocks, i.e. the local flow pattern within a building block depends solely on geometrical characteristics of that building block. In order to validate the building block approach a CFD (Computational Fluid Dynamics) approach is applied to model fully turbulent single phase flow through various types of by-pass pigs. The bulk Reynolds number is fixed at $Re = UD/\nu = 10^7$, where ν is the kinematic viscosity of the fluid, U is the average velocity, and D is the pipe diameter. A similar Reynolds number has been used in a previous CFD study on by-pass pigs [82], which allows for a direct comparison of the new results obtained in this work. From the CFD results the pressure loss coefficient K can be extracted.

The building block approach is tested on three different by-pass pig geometries encountered in the industry. First the relatively simple design of the bi-directional by-pass pig is revisited, which is shown in figure 2.1a. Furthermore, the by-pass pig shown in figure 2.2a is considered, which is referred to as the disk pig. This pig has a deflector plate, or disk, added at the exit of the by-pass pig. The deflector plate helps to get the pig into motion when the pressure drop over the pig is relatively small [96]. Finally, a by-pass pig design which is shown in figure 2.2b is considered. This by-pass pig has an adjustable by-pass area by making use of a rotatable valve. The angular position of the valve determines the opening of the by-pass holes. The adjustable by-pass enables control of the pressure drop over the pig and thus control of the speed of the pig. This by-pass pig is therefore referred to as the speed controlled pig. Examples of speed controlled pigs can be found in [63, 89].

The structure of the paper is as follows. In section 2.2 a literature review is given on theory and correlations for by-pass pig geometries and the building block approach is explained. Section 2.3 describes the numerical setup which is used for the CFD calculations.

Results obtained from the CFD simulations are discussed in section 2.4. A summary of the results and possibilities for future research are given in section 2.5.

2.2 BUILDING BLOCK APPROACH

In previous research the pressure loss coefficient of a bi-directional by-pass pig, K_{bidi} , was studied using CFD [82]. It was found that K_{bidi} can be successfully described by the Idelchik correlation for a thick orifice, as the bi-directional by-pass pig has a shape comparable with a thick orifice, see figure 2.1. For sufficiently thick orifices ($\frac{L_{\text{pig}}}{d} > 3$) the Idelchik correlation for a thick orifice reads [45]:

$$K_{\text{bidi}} = 0.5 \left(1 - \frac{A_0}{A_1}\right)^{0.75} + \frac{4fL_{\text{pig}}}{d} + \left(1 - \frac{A_0}{A_1}\right)^2, \quad (2.2)$$

where $A_0 = \frac{1}{4}\pi d^2$ is the cross-sectional area of the by-pass and $A_1 = \frac{1}{4}\pi D^2$ is the cross-sectional area of the pipe. The length of the pig is denoted by L_{pig} and f is the Fanning friction coefficient, which is determined by the Churchill relation [13] using the Reynolds number defined in the horizontal by-pass area, that is $f = f(U_{\text{bp}} d/\nu)$. Here it is assumed that the walls of the by-pass area are hydrodynamically smooth, which implies that the friction factor is not a function of the wall roughness. This correlation for a thick orifice can be regarded as a linear combination of the loss associated with the inlet of the pig (contraction loss), the by-pass area of the pig (wall friction), and the outlet of the pig (expansion loss), see figure 2.3.

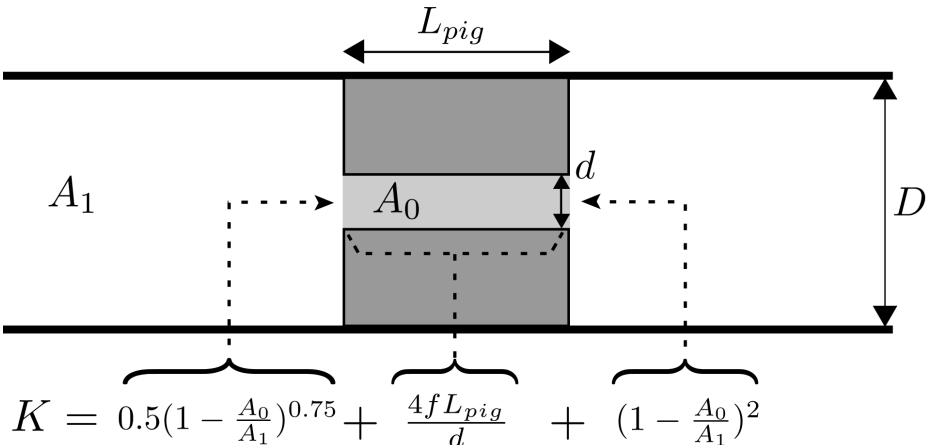


Figure 2.3: Break down of the pressure loss coefficient of a bi-directional by-pass pig in a round pipe. Symbols are explained in the text.

The use of this 'building block' approach to model the pressure loss coefficient of a by-pass pig has been suggested in previous work [67, 68], and was validated recently with

CFD for a bi-directional by-pass pig [5, 82]. In this study it is attempted to use this building block approach for a more general class of by-pass pigs, namely the disk pig and the speed controlled pig, as depicted in figure 2.2. In order to model these more complex shaped pigs it is suggested to modify the last term of equation 2.4. This last term is associated with the pressure loss of a sudden expansion, which is also known as the Borda-Carnot equation. This equation holds very well for a fully turbulent flow [60, 87]. It is important to note that the Borda-Carnot equation, along with the other contributions in equation 2.2, is associated with irreversible losses. It thus describes the change in total pressure P_t :

$$\Delta P_t = \frac{1}{2} \rho U_{bp}^2 K_{bidi} \quad (2.3)$$

As the pipe area is considered constant, the dynamic pressures upstream and downstream of the pig are equal. Therefore, the static pressure drop ΔP over the pig can be considered equal to the total pressure drop ΔP_t .

The fact that for both the disk pig and the speed controlled pig the exit of the pig can no longer be regarded as a sudden expansion emphasizes the need for a different correlation than equation 2.2. A new correlation for the disk pig and the speed controlled pig is now suggested.

2.2.1 DISK PIG

In order to replace the last term in the original Idelchik correlation 2.2 the geometry of a disk valve depicted in figure 2.4a is considered first.

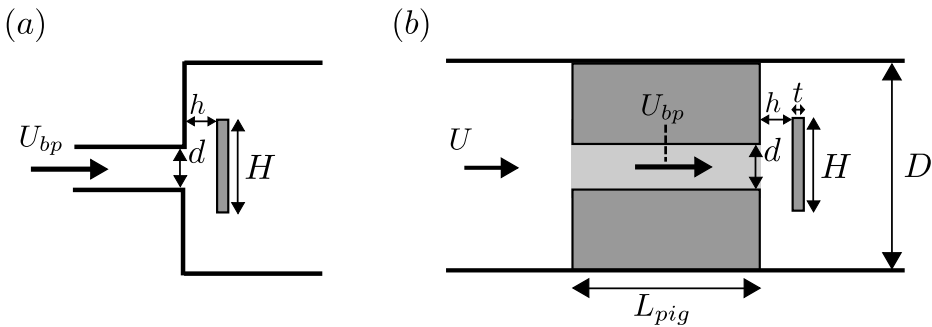


Figure 2.4: (a) Disk valve geometry, adopted from [45] (b) Schematic of the disk pig.

The geometry is taken from [45], in which the following correlation for the pressure loss coefficient of this geometry is proposed:

$$K_{dv} = \frac{2H}{d} + \frac{0.155d^2}{h^2} - 1.85. \quad (2.4)$$

This equation is reported to be valid within the range:

$$0.1 < \frac{h}{d} < 0.25, \quad (2.5)$$

and

$$1.2 < \frac{H}{d} < 1.5. \quad (2.6)$$

The validity of equation 2.4 outside this range has not been established. K_{dv} is associated with the velocity scale U_{bp} , see figure 2.4a. A schematic of the disk pig shown in figure 2.2a is depicted in figure 2.4b. The outlet of the disk pig can be represented by a disk valve as shown in figure 2.4a. The by-pass area of the disk pig A_{dv} , which is defined by the smallest by-pass area of the pig, is given by:

$$A_{dv} = \pi dh. \quad (2.7)$$

Replacing the last term of equation 2.2 with the loss coefficient of a disk valve, equation 2.4, the following correlation for the pressure loss coefficient of a disk pig K_{dp} is proposed:

$$K_{dp} = 0.5 \left(1 - \frac{A_0}{A_1}\right)^{0.75} + \frac{4fL_{pig}}{d} + \left(\frac{2H}{d} + \frac{0.155d^2}{h^2} - 1.85\right). \quad (2.8)$$

Note that the thickness of the disk t is not appearing in the proposed correlation. It is assumed that the flow is separating from the edge of the disk and will not reattach to the disk. This implies that the thickness is sufficiently small to neglect its influence on the flow.

2.2.2 SPEED CONTROLLED PIG

The speed controlled pig with a by-pass regulating valve as shown in figure 2.2b is modelled as a valve consisting of a disk with four adjustable opening slots, see figure 2.5a. The angle ω defines the opening angle of the slots in degrees. In figure 2.5b a cross-section of the speed controlled pig is shown.

The smallest by-pass area of the speed controlled pig A_{sp} is defined as:

$$A_{sp} = \pi H_i h \frac{n\omega}{360}, \quad (2.9)$$

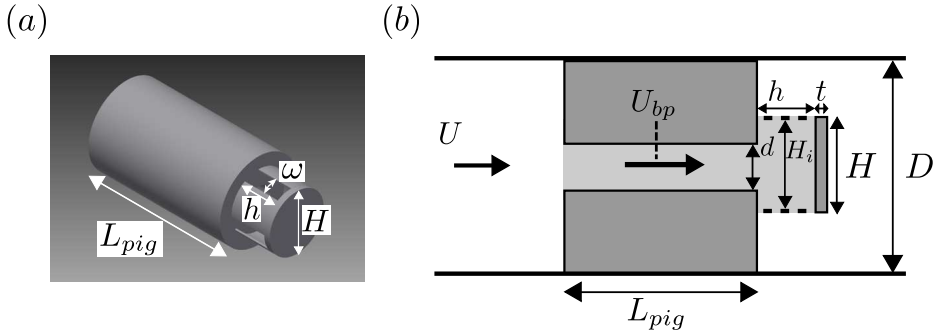


Figure 2.5: (a) 3D schematic of the speed controlled pig. (b) Schematic of a cross-section of the speed controlled pig.

where $n=4$ is the number of slots. No explicit relation for the pressure drop of such a geometry was found in the literature. As the speed controlled by-pass pig still resembles features of the geometry of the disk pig, the following correlation for the speed controlled pig is proposed:

$$K_{sp} = 0.5 \left(1 - \frac{A_0}{A_1} \right)^{0.75} + \frac{4fL_{pig}}{d} + \left(\frac{2H}{d} + \frac{0.155d^2}{h_{eqv}^2} - 1.85 \right). \quad (2.10)$$

Here h_{eqv} is the equivalent disk-to-pig distance such that the by-pass area of the speed controlled pig equals the by-pass area of a disk pig given by equation 2.7:

$$h_{eqv} = H^* \frac{h n \omega}{d 360}, \quad (2.11)$$

where H^* is the diameter of the slots, which can be taken as the inner diameter, $H^* = H_i$, or as the outer diameter $H^* = H$, see figure 2.5. Although this difference may be small in practice, these two approaches will both be treated and the result will be compared.

2.3 NUMERICAL SETUP

This section deals with the numerical setup of the by-pass pig CFD model. In this research, all the CFD simulations are performed with ANSYS Fluent (version 14.5). The pig is modelled for operation at steady state with a constant pig velocity U_{pig} . To solve the flow around the pig the Reynolds-Averaged Navier-Stokes (RANS) equations are used. To close the RANS equations the realizable $k-\epsilon$ model is used. This turbulence model was tested in previous work and was found suitable to predict the re-attachment length of the flow in the wake of backward facing step [82] as well as the pressure loss contribution of the different building blocks of the bi-directional pig [5]. Since the Reynolds number is high

($Re = 10^7$) in the CFD calculations, standard wall functions are applied for the near wall region treatment. The effect of wall roughness is neglected. It is thus assumed that the walls are hydrodynamically smooth.

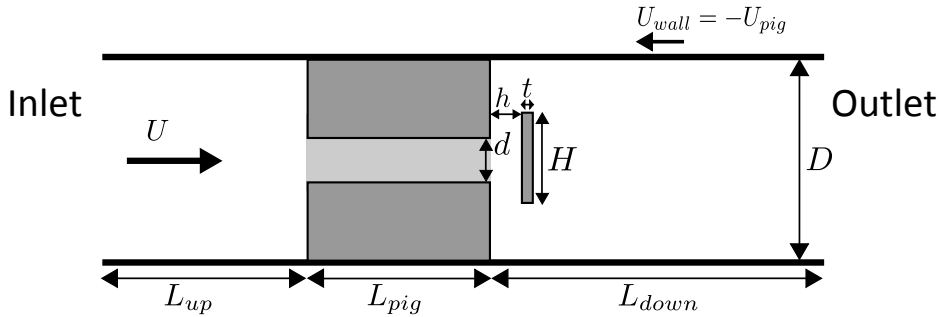


Figure 2.6: Numerical setup. The inlet is located at the left. The equations are solved in a reference frame that moves with the pig. As a result, the pipe wall moves with a velocity $U_{wall} = -U_{pig}$.

Figure 2.6 shows a schematic of the numerical setup. The RANS equations are solved in a moving reference frame of the pig [5, 82]. This means that the walls have a nonzero velocity U_{wall} equal to $U_{wall} = -U_{pig}$. A User Defined Function (UDF) is applied at the inlet to prescribe a fully developed turbulent pipe flow profile. At the outlet a constant value for the static pressure is prescribed. In figure 2.7 the mesh that is used is shown. A structured mesh for all the simulations is employed which is constructed by dividing the domain in different sub-domains with a controlled number of nodes on each edge. This way the number and shape of the computational cells in each region can be controlled. Figure 2.7b shows the mesh in the cross-sectional plane indicated by the dashed black line in figure 2.7a. An enlargement of the region within the white square is shown in figure 2.7c. The black arrow indicates a region of mesh refinement. The location of this mesh refinement corresponds to the radius of the horizontal by-pass area in order to refine the grid near the wall of the by-pass area. The same procedure is applied to the mesh at the inner pipe wall. The typical maximum value of y^+ in the simulation is around 4500, which is well within the range $30 < y^+ < 20000$ for which the flow is in the logarithmic layer, and standard wall function can be used to predict the velocity profile, see [24, 51].

2.4 RESULTS

In this section the CFD results for the disk pig are discussed first. The obtained values for the pressure loss coefficient K are compared with the correlation suggested in equation 2.8. Next, the CFD results for the speed controlled pig are discussed. The obtained K values will be compared with equation 2.10. For the disk pig axi-symmetry is assumed and the

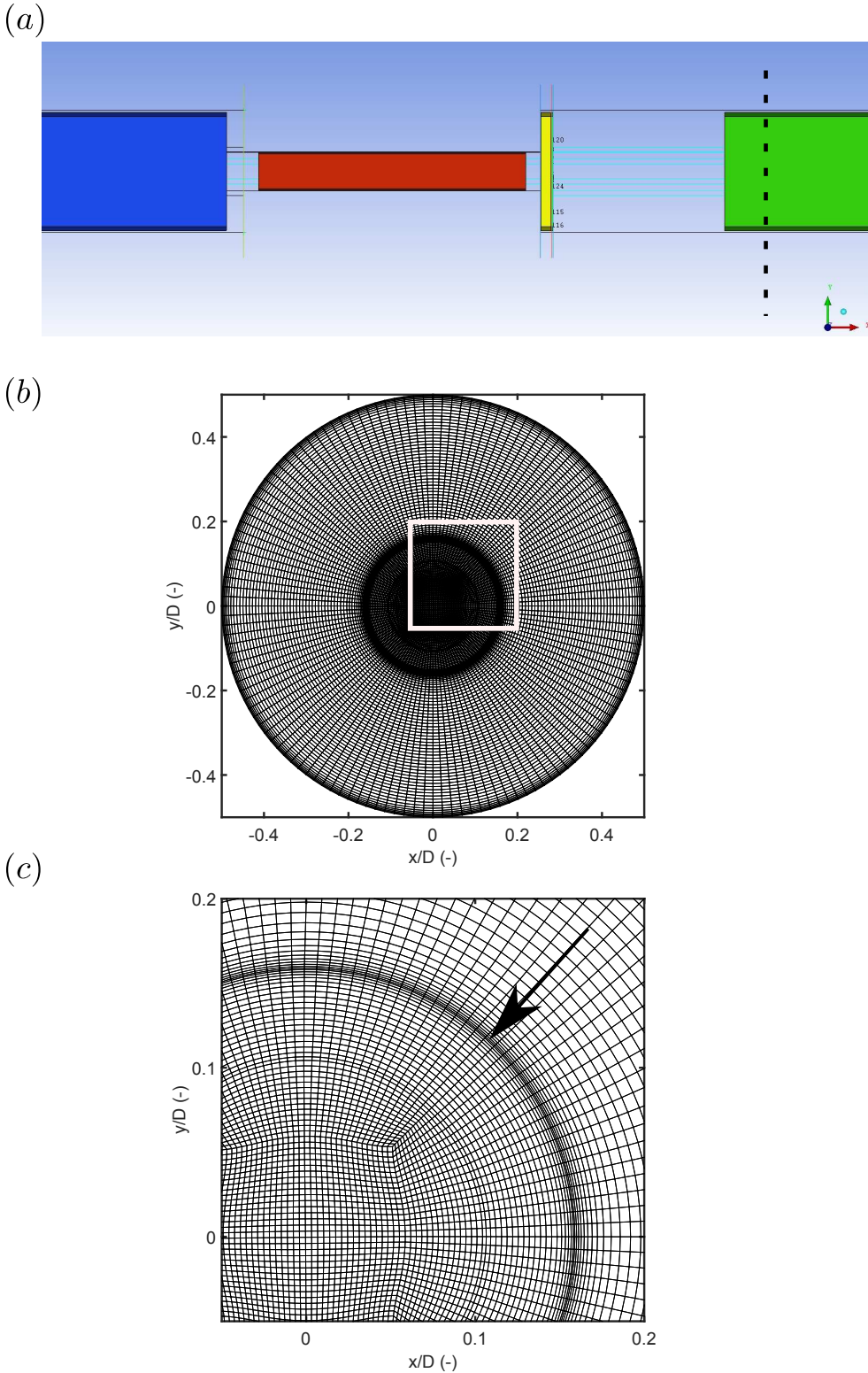


Figure 2.7: (a) Blocks that represent different regions in streamwise direction. (b) Details of the mesh on the cross-sectional plane indicated by the dashed line in panel a. (c) Enlargement of the area indicated by the white square.

CFD simulation is 2D, but for the speed controlled pig no axi-symmetry exists and the CFD simulation is 3D.

2.4.1 DISK PIG

The flow around a disk pig has already been studied by Korban et al. [5]. In their study, the relation between the pressure loss coefficient K and the parameters which govern the disk pig model, was investigated. The K value of the disk pig was found to be around 2 to 3 times higher than the typical value that is found for a bi-directional pig (without disk). However, a general correlation to predict the pressure loss coefficient K for a disk pig was not given. Thus, in the present research, the flow around the disk pig is further investigated. Table 2.1 summarizes the key parameters which define a base case for the disk pig simulations. These parameters are based on a realistic scenario, which can be found in [96]. The parameters will be varied through using the following dimensionless numbers which define the disk pig geometry:

- Horizontal by-pass area fraction: $(\frac{d}{D})^2$
- Dimensionless disk height: $\frac{H}{D}$
- Disk by-pass area fraction: $\frac{4dh}{D^2}$

As discussed in section 2.2, the effect of the dimensionless disk thickness t/D as well as the dimensionless pig length L_{pig}/D are not studied here.

First of all, the flow features of the disk pig are presented. Interestingly, two different types of flow behaviour around the disk pig have been observed in the simulation results. Secondly, various parameter studies are carried out, in order to study the relation between the pressure loss coefficient K and the governing parameters of the disk pig model.

2.4.1.1 Flow features of disk pig

Figure 2.8 shows the streamlines that represent the mean flow around the disk pig. The fluid enters the pig through a sudden contraction. The flow behaviour in this region is similar to that of the conventional bi-directional pig [5]. After the horizontal by-pass region, the flow moves around the disk. In the disk by-pass region, the flow expands radially outward and has a jet-like structure. The flow subsequently detaches from the disk creating a recirculation zone downstream of the pig. To give insight in the pressure loss for the disk

Table 2.1: Key parameters that govern the disk pig study.

Parameter	Value
Bulk velocity U	2.87 m/s
Horizontal by-pass area (%)	10%
Disk by-pass area (%)	8%
Pipe diameter D	1.16 m
By-pass pig diameter d	0.3668 m
Upstream pipe length L_{up}	5D
Downstream pipe length L_{down}	20D
Pig length L_{pig}	2 m
Pig velocity	2 m/s
Distance between the pig body and the disk h	0.06303D
Disk diameter H	0.396D
Disk thickness t	0.00862D
Density ρ	68 kg/m ³
Viscosity μ	2.264 E-5 kg/ms
Reynolds number Re	1 E+7

pig, the streamlines in figure 2.8 are colour coded with the local value of the total pressure coefficient C_{tp} . Here C_{tp} is defined as:

$$C_{tp} = \frac{P_t - P_{t\infty}}{\frac{1}{2}\rho U_{bp}^2}, \quad (2.12)$$

where P_t is the local total pressure and $P_{t\infty}$ is the total pressure downstream of the pig. As the total pressure is the sum of the static pressure and the dynamic pressure, C_{tp} can be associated with the irreversible losses in the system. As can be seen in figure 2.8, the recirculation zone is associated with dissipation in the flow, which is reflected in the low value of the total pressure coefficient C_{tp} after the flow has detached from the pig.

In general, two different types of flow behaviour are found. Figure 2.8a shows the first flow behaviour. A jet is formed in the disk by-pass region. After the jet has moved away from the disk by-pass region, it first contacts the pig wall. Then, the jet moves along the pig wall towards the pipe wall. There is a small recirculation zone between the jet and the pig wall upstream of the disk. Another large recirculation zone is observed downstream of the disk. Figure 2.8b shows the second flow behaviour around the disk pig. After the disk by-pass region, the jet does not first contact the pig wall, but it contacts the downstream pipe

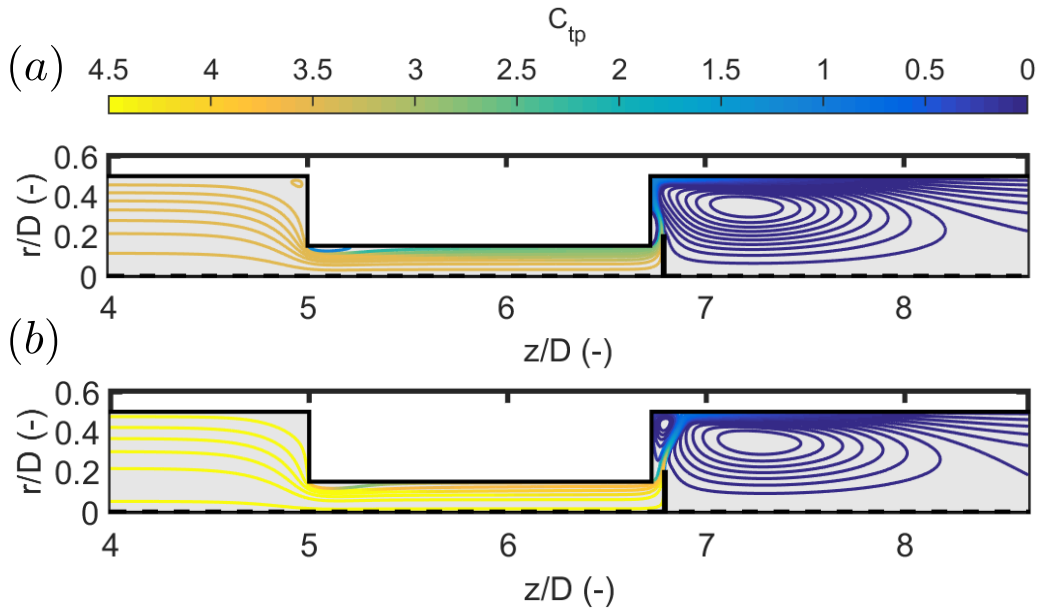


Figure 2.8: (a) Flow behaviour A. (b) Flow behaviour B. The streamlines are colour coded by the value of the total pressure coefficient.

wall directly. Thus, the recirculation zone between the pig body and the jet is located in the corner of the pig wall and the downstream pipe wall. The main recirculation zone is still located downstream of the pig. In this research, the flow behaviours shown in Figure 2.8a and Figure 2.8b are referred to as “flow behaviour A” and “flow behaviour B”, respectively. Most importantly, the pressure drop across the disk pig is strongly dependent on the flow behaviour around it, which is reflected in the higher value of C_{tp} upstream of the pig for flow behaviour B compared to flow behaviour A.

Interestingly, the two flow solutions depicted in figure 2.8 are found for the same geometrical by-pass pig model subjected to the same boundary and inlet conditions. The equations thus allow for multiple steady state solutions. The applied parameters are as summarized in Table 2.1 but with a horizontal by-pass of 9% instead of 10%. The difference in steady state flow behaviour is caused, however, by a difference in initial condition. Flow behaviour A is part of the converged iterative solution of the steady state equations that are solved in Fluent using the default initialization scheme. Also another approach was taken in which the transient solver was used to reach steady state. In this case flow behaviour B was found. This solution was verified to indeed obey the steady state equations by initializing the steady state solver with flow behaviour B obtained from the transient simulation. Thus, for a disk pig model with certain governing parameters, two completely different numerical solutions can be achieved, and both solutions are in steady state. More details for the two solution region are provided in A. Multiple stable solutions for flow over a confined axisymmetric sudden expansion have been observed before, see for ex-

ample [81]. The direct attachment of the jet (behaviour A) can be induced by the Coanda effect and can cause hysteresis in the flow behaviour [92, 93]. According to the literature, it is also possible that an emerging jet in a confinement shows persistent oscillatory behaviour, instead of the two distinct steady states [77]. This oscillation, however, was not observed in the current study.

2.4.2 PARAMETER STUDY

In this section the parameters which govern the disk pig model are varied to investigate the effect on the pressure loss coefficient K . Figure 2.9a shows the value of C_{tp} along the centreline of the disk pig shown in figure 2.8. The pressure loss coefficient K can now readily be determined:

$$K = C_{tp,up} - C_{tp,down}, \quad (2.13)$$

where $C_{tp,up}$ and $C_{tp,down}$ are the total pressure coefficients upstream and downstream of the pig, respectively. As was already shown in the previous section, flow behaviour B is associated with a higher loss coefficient compared to flow behaviour A, which amounts to a difference of 30%. The effect of the dimensionless parameter $(d/D)^2$ on the two solutions and on K is also investigated by changing $(d/D)^2$ from 5% to 12.5%. This result is shown in figure 2.9b. The two solution region was found to be in the region:

$$7.8\% < \left(\frac{d}{D}\right)^2 < 11.3\%. \quad (2.14)$$

More details on the exploration of the two solution region can be found in A. Furthermore, the values of K obtained from the CFD simulations are compared with the correlation given by Equation 2.8. Good agreement between the correlation for the disk pig and the CFD values was found, provided that the flow exhibits behaviour B.

Next, the effect of the disk diameter H is investigated through changing the dimensionless number H/D from 0.325 to 0.55, while keeping the other parameters fixed. Figure 2.9c shows that when the disk has a relatively small disk height (when $H/D < 0.35$), the flow around the disk pig has behaviour B, while for $H/D > 0.375$, the flow around the disk pig has behaviour A.

The obtained CFD results are again compared with Equation 2.8 (the latter is represented by the black solid line in figure 2.9c). Similar as was found for the parametric study of the horizontal by-pass area it can be concluded that Equation 2.8 describes K_{dp} accurately if the flow around the disk pig has behaviour B. When H/D is larger than 0.375 and when the flow around the disk pig exhibits behaviour A, the pressure loss coefficient is found to have a constant value around $K_{dp} = 3.83$.

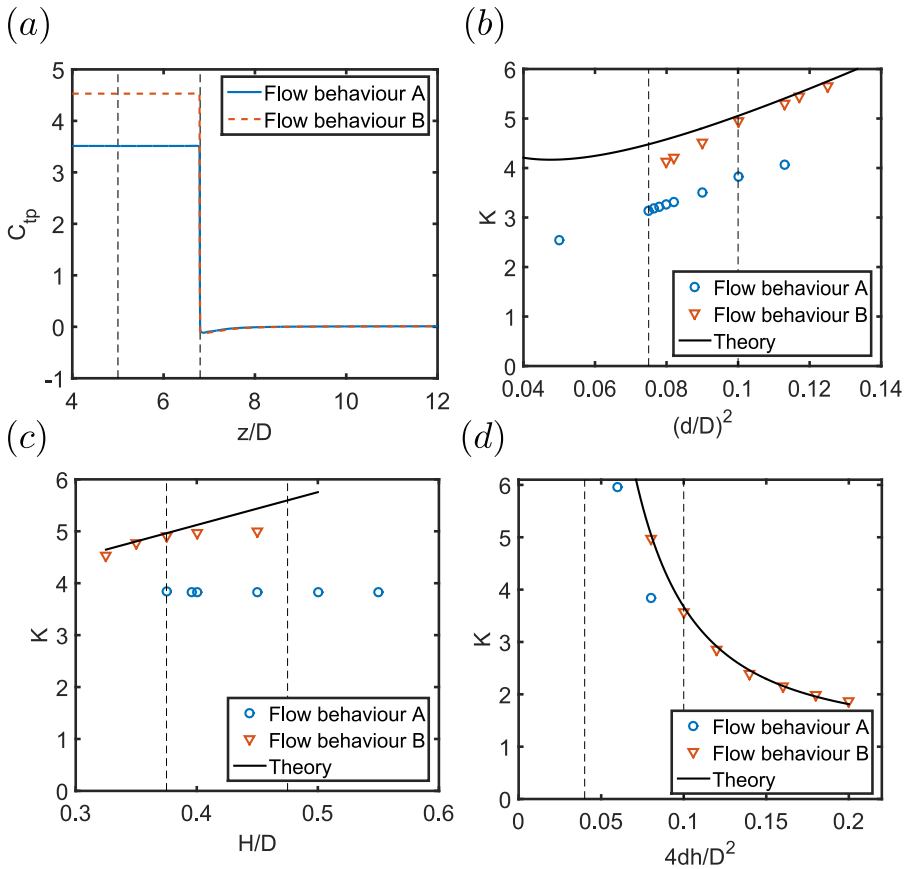


Figure 2.9: (a) Total pressure coefficient along the centerline. (b) Pressure loss coefficient as function of the horizontal by-pass area $(d/D)^2$. (c) Pressure loss coefficient as function of H/D (d) Pressure loss coefficient as function of the disk by-pass area $4dh/D^2$. Values between the vertical dashed lines in b-d indicate the validity of Equation 2.8.

Finally, the parameter study of the disk by-pass area fraction $4dh/D^2$ is carried out. In this parameter study, the parameters are again kept fixed as shown in table 2.1, and change the distance between the pig body and the disk h , in order to change the dimensionless parameter disk by-pass area $4dh/D^2$ from 6% to 20%. Figure 2.9d shows the result of the obtained loss coefficient K_{dp} as a function of the disk pig by-pass area $4dh/D^2$. It is found that when the parameter h is relative small (when $4dh/D^2 < 8\%$), the flow around the disk pig has behaviour A, and when $4dh/D^2 > 10\%$, it changes to behaviour B. Equation 2.8 is represented by the black solid line. Similar as found in the two previous parameter studies, Equation 2.8 can predict K_{dp} accurately if the flow around the disk pig has behaviour B. Even though the points with flow behaviour B are partially out of the range for which Equation 2.8 is reported to be valid, good agreement with the CFD results is found.

Table 2.2: Key parameters that govern the speed controlled pig study.

Parameter	Geometry 1	Geometry 2
Horizontal by-pass area (%)	10%	30%
By-pass pig diameter d	0.3668 m	0.6354 m
Upstream pipe length L_{up}	2D	2D
Distance between the pig body and the disk h	0.1118D	0.2236D
Disk diameter H	0.4835D	0.7071D
Inner diameter holes H_i	0.4472D	0.4472D
Disk thickness t	0.07071D	0.07071D
Number of holes n	4	4

2.4.3 SPEED CONTROLLED PIG

This section is focused on the pressure drop coefficient of the speed controlled pig with the geometry depicted in figure 2.5. For the speed controlled pig four by-pass adjusting holes are generated to represent the by-pass adjusting device (which gives the dimensionless parameter $n = 4$). The angle of the by-pass adjusting holes ω is changed to represent the speed control process. Through changing ω the dimensionless number $\frac{4hH_i(n\omega/360)}{D^2}$ is changed. This number represents the by-pass area fraction of the holes of the speed controlled pig. This dimensionless number is additional to the ones which already have been studied for the disk pig in the previous section. The effect of this dimensionless number on the pressure loss coefficient of the speed controlled pig is studied for two base geometries: one with a horizontal by-pass area of 10% and one with a horizontal by-pass area of 30%. The specific parameters of these two models are summarized in Table 2.2. The other parameters used in the simulation are unchanged with respect to the ones used in the previous section and can be found in Table 2.1. The maximum opening angle of the by-pass holes is 45 degrees. This means that the total opening with 4 holes is 180 degrees which is the maximum that can be achieved with a rotating valve. The distance of the disk to the pig body is matched in such a way that for an opening angle $\omega = 45$ degrees the by-pass area of the holes is equal to the horizontal by-pass area. When the holes close, the by-pass area of the holes decrease, and will be smaller than the horizontal by-pass area. This ensures that the main pressure drop occurs through the holes, which enables control over the pressure loss as intended. As a consequence the maximum velocity in the system will always be located at the by-pass holes.

Figure 2.10 shows a typical result obtained for the flow around the speed controlled pig. This model has a horizontal by-pass area of 30% and the opening angle of the holes ω is 45 degrees. As can be seen from Figure 2.10a, the jets formed in the by-pass adjusting holes contact the pipe wall directly, and there is a recirculation zone both at the corner of

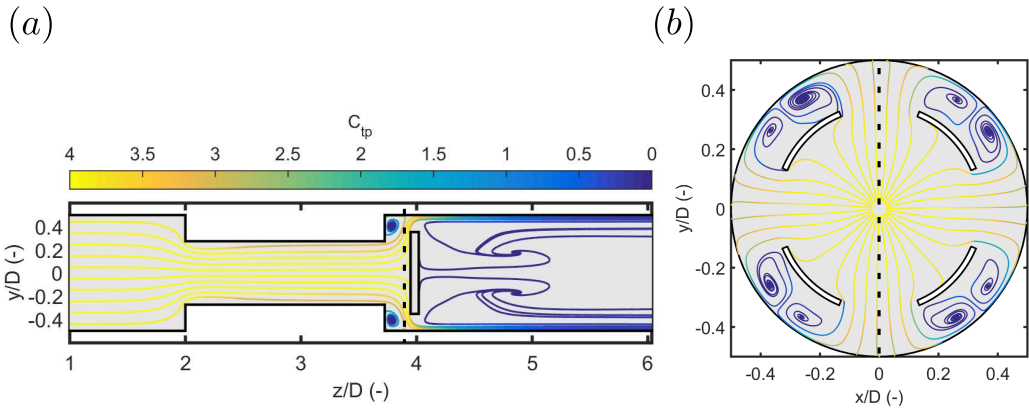


Figure 2.10: (a) Streamlines around the speed controlled pig. (b) Streamlines in the region of the by-pass holes. The dashed black line indicates the same position in both panels.

the pig body and at the pipe wall. This is thus similar to flow behaviour B for the disk pig. This flow behaviour is observed for all the cases which were investigated for the speed controlled pig. This is mainly due to the location of the disk, which is typically placed at a larger distance from the pig body for the speed controlled pig compared to the disk pig. The main recirculation zone is in the downstream pipe and is much more complex than in the disk pig case. This is because there are four three-dimensional main jets formed in the four by-pass adjusting holes, and when the jets bend around the disk, the jet-like flow mixes again in the downstream pipe. A close up of the jets emerging from the by-pass holes is depicted in figure 2.10b. Similar to the disk pig, the main pressure drop occurs at the exit of the by-pass pig, which is shown by the streamlines which are colour coded with the value of the total pressure coefficient.

Next, a parameter variation of the two by-pass geometries listed in table 2.2 is carried out. As the maximum velocity is always located in the holes it is intuitive to use this velocity to scale the pressure drop coefficient. Note that until now, the velocity in the horizontal by-pass area U_{bp} has been used to scale the pressure drop. Therefore, a modified pressure loss coefficient K' is defined which uses the velocity in the holes as a velocity scale. K' can thus be related to K as:

$$K' = \left[\frac{4hH_i(n\omega/360)}{d^2} \right]^2 K. \quad (2.15)$$

The parametric study is carried out by choosing the following values for ω : 11.25° , 22.5° , 37.75° and 45° . The results are depicted in figure 2.11.

It is noted that for $\omega = 45^\circ$ the by-pass area of the holes is equal to the horizontal by-pass area. In addition, the proposed correlation Equation 2.10 is included. This correlation is based on treating the speed controlled pig as an effective disk pig, as explained in section 2.2. The proposed correlation, despite the simplified approach, is able to predict the

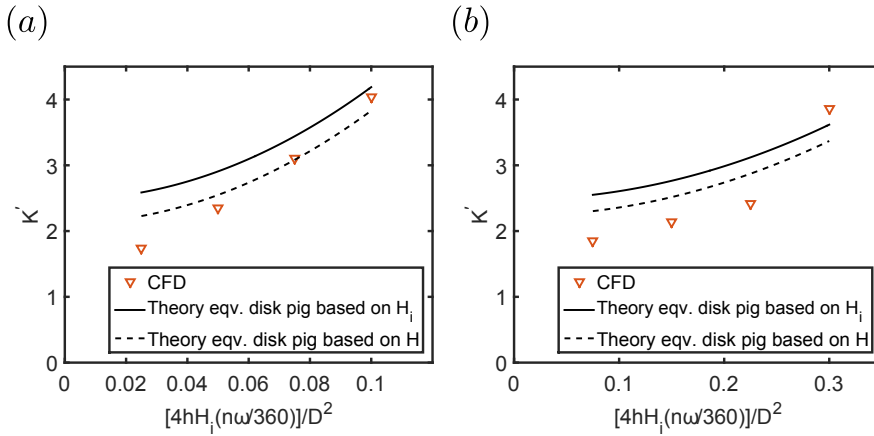


Figure 2.11: (a) Pressure loss coefficient as function of the by-pass area fraction of the holes for a horizontal by-pass area fraction of 0.1. (b) Pressure loss coefficient as function of the by-pass area fraction of the holes for a horizontal by-pass area fraction of 0.3.

right trend that is given by the CFD results. However, especially for lower values of the by-pass area, the suggested correlation overpredicts the results. Nonetheless the correlation can help to give a first estimation of the pressure loss coefficient of a speed controlled pig with a geometry as approximated by the schematic as shown in figure 2.5.

2.5 CONCLUSIONS

In this chapter a building block approach was applied to describe the pressure loss coefficient K of various by-pass pig geometries. First of all, K of the conventional bi-directional by-pass pig has been revisited. Subsequently, new correlations for more complex geometries have been proposed and compared with CFD simulations using the building block approach. This building block approach allowed to construct correlations and for the disk pig geometry and the speed controlled pig geometry. A two solution region was found for the disk pig geometry, which means that there are two stable flow behaviours (type A and type B) within the RANS framework of the current study. Good agreement was found between the proposed correlation for the disk pig and the CFD results, provided that the flow exhibits flow behaviour B. In addition, the pressure loss coefficient of the speed controlled pig was characterized. It was found that a correlation based on an equivalent disk pig gives qualitatively the right trend, but deviates quantitatively for small opening angles of the holes of the speed controlled pig. Further research is needed to predict K also for small opening angles of the holes. It is also of interest to further investigate the two solution region that was found for the disk pig. The boundary of the two solution region may be sensitive to the parameters of the RANS model, most notably the turbulence model. It would also be interesting to investigate the existence and stability of the two solution

region experimentally in order to further verify the CFD modelling. The proposed building block approach has been successfully applied to describe the pressure loss coefficient of various by-pass pig geometries, and may also be applied to systematically model the pressure loss coefficient of complex flow geometries in general.

3

FRictionAL FORCES FOR DISC-TYPE PIGGING OF PIPELINES

This chapter is adopted from M.H.W. Hendrix, C.M. Graafland, and R. van Ostayen, "Frictional forces for disc-type pigging of pipelines". In: *Journal of Petroleum Science and Engineering* 171 (2018), pp. 905-918.

3.1 INTRODUCTION

Pipelines that are used for the transport of fluids represent significant costs and need regular maintenance [78, 79]. In the oil and gas industry this is usually done by sending so-called pigs through the pipeline, see Figure 3.1a. Such a pig travels along with the production fluids through the pipe and can serve multiple maintenance purposes. For example pigs are used to remove wax particles that may have been deposited at the pipe wall [74, 85, 94, 95] or to sweep out unwanted liquid accumulation in a pipeline that is used for multiphase gas-liquid transport [21, 96]. Apart from cleaning purposes, pigs can be equipped with sensors which inspect the condition of the pipe wall. This is also referred to as intelligent pigging [63, 74]. For a detailed overview of pigging applications and pig types, the reader is referred to [15, 90]. In any case the pig is driven by the production fluids which are transported through the pipeline. This means that the pressure difference that is generated over the pig has to overcome the frictional force between the pig and the pipe wall. To ensure a safe and effective pigging operation it is thus required to know the frictional force in order to prevent too high pressures in the system.

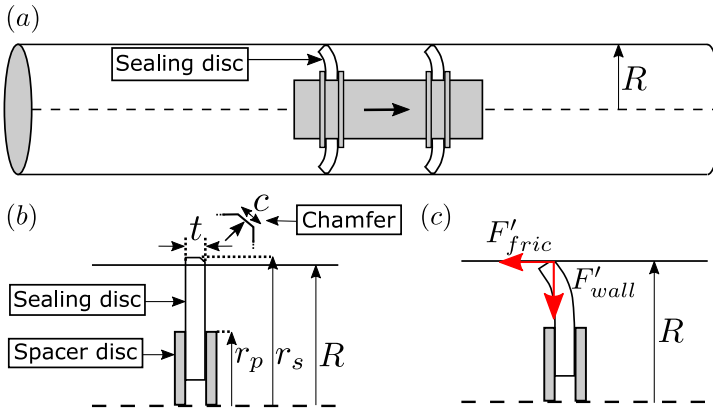


Figure 3.1: (a) A pig travelling inside a pipeline (b) Undeformed sealing disc. (c) Deformed sealing disc.

A conventional pig completely seals the pipeline with a flexible sealing disc, see Figure 3.1. The radius of the sealing disc usually has an oversize compared to the inner pipe radius, which ensures a tight seal between the pig and the pipe wall. The travel velocity of a conventional pig through a pipeline is therefore equal to the mixture velocity of the upstream fluids. In some cases it is desired to lower the travel velocity of the pig, as it may cause damage to the pipeline or the pig itself. Also for cleaning, liquid removal, and inspection purposes it is beneficial to reduce the pig velocity [12, 63, 91, 96]. A solution to achieve a lower pig velocity without causing production loss is the use of by-pass pigs [96]. By-pass pigs have a by-pass hole which allows the production fluids to flow through the

pig. As a result the pig velocity is not dictated by the upstream mixture velocity anymore, but it is, in a horizontal pipe, determined by a balance of the by-passing fluid force and the frictional force of the pig with the pipe wall. The force on a by-pass pig due to the by-passing fluids has been previously studied for various by-pass pig configurations, see [35, 82]. The main focus of the current study is on the frictional forces which are encountered during pipeline pigging. As the pig contacts the pipe wall through the sealing disc, the effect of the properties of the sealing disc on the frictional force is of interest. The external force of the pipe wall on the sealing disc is distributed along the circumference and has unit Newton per meter circumference. The distributed force can be decomposed in a distributed friction force (F'_{fric}) oriented parallel to the direction of movement of the pig and a distributed wall normal force (F'_{wall}), as shown in Figure 3.1c. At the onset of sliding the ratio of these two distributed forces gives the local Coulomb friction coefficient.

Almost no models are available to estimate the frictional force during pipeline pigging: predictions often rely on empirical findings and on field experience [14, 22]. For example Cordell [14] presents a diagram in which the driving pressure that is needed to overcome the frictional force is solely dependent on what type of pig is used (e.g. a cleaning pig versus an inspection pig). However, no information on the geometrical or material properties of the sealing disc is present in this approach. O'Donoghue [70] presents a simplified model which does include geometrical and material properties of the sealing disc into a friction model. This model assumes that the deformed sealing disc adopts the shape of an circular arc and subsequently evaluates the internal stresses in the sealing disc which can be used to predict the frictional force. Despite that the model contains more physics than for example Cordell's model, it is known to systematically underpredict the friction force [34, 70]. Rather than relying on a simplified model, another approach is to perform a full Finite Element (FE) calculation of the sealing disc, which has recently been undertaken in [99, 100]. Clearly, an axisymmetric 2D or even full 3D FE approach has the advantage that it contains more physics than for example a simplified axisymmetric 1D approach, such as for example the model of O'Donoghue [70]. On the other hand, it is more difficult to embed case specific FE calculations in already existing tools.

Two types of laboratory approaches to experimentally study the frictional force of a sealing disc have been found in the literature. One approach consists of a pull test in which a sealing disc/pig is pulled through a pipe while monitoring the pulling force [100, 101]. An advantage is that in steady state motion this pull force can be directly related to the friction force. A disadvantage is that the wall normal force is not directly measured, and therefore the Coulomb friction coefficient is unknown. Another approach relies on fixating the sealing disc while pressing it against a rotating steel plate which mimics the pipe wall, see [86] in which this setup was used to study wax removal from a pipe wall. Such a setup can be used as a tribometer in which the load and friction force can be simultaneously measured which enables to measure the friction coefficient for various contacts [52, 84]. While the Coulomb friction coefficient can be carefully characterized with such a setup,

a disadvantage is that the friction force of a sealing disc in a confining pipe geometry is not directly measured.

In the present research a static experimental setup is presented which is used to simultaneously measure the friction force and the wall normal force acting on a sealing disc in a confining pipe geometry. The static setup is a modified and improved version of the setup described in [34], which will be explained in the Section 3.2. Six 12'' off the shelf sealing discs from two different vendors have been used in the experiment. A flexible hull is wrapped around the sealing disc and F'_{wall} is subsequently generated by reducing the diameter of that hull. F'_{fric} is generated by pulling the disc in the axial direction. The forces are recorded in static equilibrium. The forces that are applied in static equilibrium are the same as for a sealing disc that moves in steady state motion through a pipeline. By changing the force ratio between the friction force and the wall force the Coulomb friction coefficient which would apply to a sealing disc which moves at steady state is thus mimicked. The experimental setup thus allows to study the effect of the friction coefficient which is difficult to study in a dynamic experiment in which a sealing disc is pulled through a pipe and the wall force is generally unknown. The results from the static setup, which is referred to as static pig pull facility, are captured by 2D axisymmetric FE calculations for which appropriate boundary conditions are formulated. A detailed comparison is made for both the involved forces as well as the shape of the deformed sealing disc. Apart from the friction coefficient, the effect of the oversize, the thickness, and the Young's modulus of the sealing disc on the friction force are investigated.

Next to the static pig pull facility, a new dynamic pig pull experiment is designed which is used to present a case example of how the results of the static pig pull facility can be related to a dynamic pull test. In this dynamic experiment the sealing disc is pulled through a 1.7 meter vertical pipe while monitoring the pull force. The effect of possible lubrication by applying water at the sliding contact is investigated. The difference in friction coefficient between a dry and wet contact is quantified.

The outline of this chapter is as follows. In Section 3.2 the experimental setup of the static and the dynamic pig pull facility and the applied measurement procedure are explained. At the end of the section the numerical setup for the FE calculations and the applied boundary conditions are discussed. Section 3.3 presents the results from the static pig pull facility and a direct comparison with the FE calculations is made. Subsequently the results from the dynamic pig pull facility are presented and linked to the results of the static experiments. Section 3.4 concludes and discusses possibilities for future research.

3.2 METHODS

Inspecting Figure 3.1b we can identify two dimensionless numbers pertaining to the undeformed geometry of the sealing disc. There is a dimensionless thickness t' and a dimensionless clamping ratio r'_p , which are defined as:

$$t' = \frac{t}{r_s - r_p}, \quad (3.1)$$

$$r'_p = \frac{r_p}{r_s}. \quad (3.2)$$

Here t is the thickness of the sealing disc, r_s is the outer radius of the sealing disc, and r_p is radius of the spacer discs which are used to attach the sealing disc to the pig body. A third geometrical dimensionless number could take the presence of a possible chamfer into account, see Figure 3.1b. The dimensionless chamfer height can be for instance defined as $c' = c/t$, where c is the length of the chamfer which is for simplicity assumed to be under an angle of 45 degrees. The effect of a variation in chamfer size is discussed in Section 3.3.4. Two additional dimensionless numbers can be introduced for the sealing disc which is deformed due to the confinement of the pipe wall, see Figure 3.1c. We define the oversize parameter Δ and the force ratio μ as follows:

$$\Delta = \frac{r_s - R}{R} \times 100\%, \quad (3.3)$$

$$\mu = \frac{F'_{\text{fric}}}{F'_{\text{wall}}}. \quad (3.4)$$

Here R is the inner pipe radius, F'_{fric} is the distributed friction force and F'_{wall} is the distributed wall normal force. Most sealing discs are made of polyurethane. This elastomer has a high abrasion resistance, tear strength and resistance to hydrocarbons [70]. The chemical composition of the sealing disc is proprietary to the manufacturer of the pig and it influences the Young's modulus of the material, which is also referred to as E-modulus. The E-modulus is usually an input parameter for deformation models. Unfortunately, manufacturers do not specify the E-modulus of their product. Instead they specify the Shore A hardness, which is a measure of the resistance of a material to indentation. Typical values for the Shore A hardness of sealing discs are in the range of 60 - 85 [15].

In this study a total of six sealing discs have been studied, see Table 3.1. These discs have been obtained from two different pigging vendors, here anonymously named X and Y. The discs from both vendors are intended for pigging of 12'' pipelines. From vendor X,

Table 3.1: Overview of the sealing discs used in this study. Both the geometry and the material properties of the discs are listed. One set of spacer discs is used for all experiments ($r_p = 86$ mm).

	Disc A	Disc B	Disc C	Disc D	Disc E	Disc F
Batch	X ₁	Y	X ₂	X ₂	X ₂	X ₃
r_s (mm)	163.3	161.2	155.2	155.0	154.7	155.4
t (mm)	15.9	15.2	13.6	15.5	17.4	15.4
r'_p (-)	0.527	0.533	0.554	0.555	0.556	0.553
t' (-)	0.203	0.202	0.197	0.224	0.254	0.221
Shore A hardness	75 (75.6) ^b	75 (79.6) ^b	75	75	75	65
E-modulus (MPa)	8.5	13.7	10.1 ^a	10.1	10.1 ^a	6.0

^a The E-modulus of this disc is not obtained in a test, but assumed to be equal to the E-modulus of disc D. This disc is from the same batch as disc D, and only has a different thickness.

^b Values as measured according to ASTM D2240, see Appendix B.

three different batches were obtained: X₁, X₂, and X₃. The Shore hardness as specified by the manufacturer is listed. As the E-modulus was not specified it was determined by material tests. These tests consisted of a stress strain analysis using representative dog bone samples from the disc. In addition to the stress strain tests, the Shore hardness of disc A and disc B was determined. A value of respectively 75.6 and 79.6 was found, which are put in between brackets in Table 3.1. The value of disc A is within the specification of the manufacturer, but the value of disc B is slightly higher. The details of the material tests can be found in Appendix B. In any case it is clear that the value of the specified Shore hardness cannot be used to deduce the E-modulus, for example by using the Gent equation [26], as discs with the same specified Shore hardness turn out to have different values for the E-modulus. The radius of the spacer discs is kept constant in the experiments and is equal to 86 mm. All experiments have been performed at room temperature.

Disc A and disc B are the main discs that are used in our experiments. They have similar properties except that they come from a different vendor and have a different E-modulus. Disc C, D, and E are from the same vendor and from the same batch. They have similar properties, except for the variation in the thickness of the discs. These discs are used to study the effect of the thickness on the friction force. Discs C and disc F have similar properties except for the E-modulus. These discs are thus used to study the effect of the E-modulus on the friction. The effect of the oversize Δ and of force ratio μ are investigated for all the discs, as the experimental setup is designed to easily vary these parameters, which will be explained in the next section.

3.2.1 STATIC PIG PULL FACILITY

Deformation of the sealing disc is caused by the external forces F'_{wall} and F'_{fric} . In static equilibrium these forces are balanced by internal stresses in the polyurethane disc. The ratio of the external forces F'_{fric} and F'_{wall} gives the force ratio μ , see equation 3.4. This force ratio would be equal to the Coulomb friction coefficient of a sealing disc which moves at steady state through a pipeline on which the same forces act. The friction coefficient is a difficult parameter to predict, since it depends on both the material properties of the sealing disc and the local conditions of the inner pipe wall. Furthermore, it also depends on the type of fluids that are being transported, as these fluids may act as lubricant which can decrease the friction coefficient [72, 84]. Instead of trying to predict this force ratio, an experiment is designed in which the force ratio can be imposed, see Figure 3.2. The experimental setup is a modified version of the setup presented in [34] and works as follows.

The setup consists of a flexible hull which is wrapped around the sealing disc, see Figure 3.2a. By applying a force F_1 on the hull, the diameter of the hull will be reduced. As a result the sealing disc will deform and the corresponding force F_1 is recorded by a force sensor. The diameter reduction of the hull mimics the confinement of the pipe wall which determines the oversize parameter Δ , see equation 3.3. The oversize can thus be easily varied by changing the diameter of the hull. We define the magnitude of the distributed wall force and friction force integrated along the edge of the pipe as F_{wall} and F_{fric} respectively:

$$F_{\text{wall}} = 2\pi R |F'_{\text{wall}}|, \quad (3.5)$$

$$F_{\text{fric}} = 2\pi R |F'_{\text{fric}}|. \quad (3.6)$$

The unit of F_{wall} and F_{fric} is Newton. By applying the principle of virtual work, F_{wall} can be related to the circumferential force F_1 :

$$\begin{aligned} F_{\text{wall}} dr &= F_1 2\pi dr \\ F_{\text{wall}} &= 2\pi F_1. \end{aligned} \quad (3.7)$$

Here r represents the radial coordinate. A second force F_2 is generated by displacing the centre of the disc in axial direction, see Figure 3.2a/b. The force sensor which records F_2 is located at the back of the setup. This force is equal to the friction force F_{fric} in the axial direction between the hull and the sealing disc:

$$F_{\text{fric}} = F_2. \quad (3.8)$$

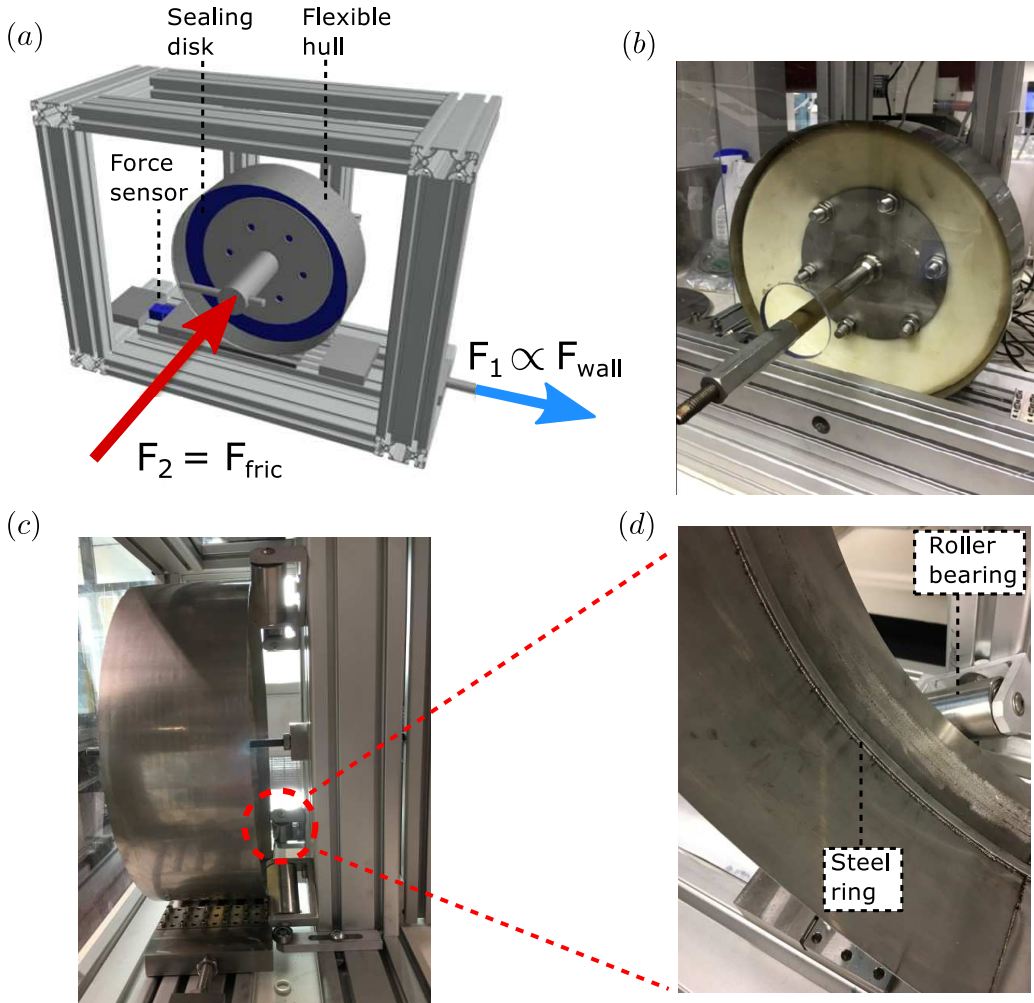


Figure 3.2: (a) Schematic of the setup. (b) Front view of the setup. (c) Side view of the setup. (d) Close-up of the steel ring and roller bearing.

The force ratio can now be expressed in terms of F_1 and F_2 :

$$\mu = \frac{F_{\text{fric}}}{F_{\text{wall}}} = \frac{F_2}{2\pi F_1}. \quad (3.9)$$

By changing F_2 and F_1 the force ratio can be readily varied. In order to be able to obtain higher values of the force ratio as compared to [34], a 2 mm steel ring has been welded onto the hull in the circumferential direction, see Figure 3.2d. This ring prevents that the disc slides in the axial direction when F_2 is increased.

A side view of the setup is shown in Figure 3.2c. Here it is visible that the back of the flexible hull is supported by roller bearings which are mounted on the frame. Figure 3.2d shows a close-up of one of the six roller bearings which are used. The addition of roller bearings is an improvement compared the setup as presented in [34]. The roller bearings ensure that very little friction exists between the hull and the frame. This is especially important when the axial force F_2 is increased, which effectively pushes the hull against the roller bearings. Without the roller bearings a friction force between the hull and the frame could exist which would result in an under prediction in the value of F_1 . The setup is operated in such a way that static equilibrium is reached. The corresponding values for F_{fric} and F_{wall} in this static situation represent the same force balance that would apply to a sealing disc on a pig that moves in steady state motion in a pipeline.

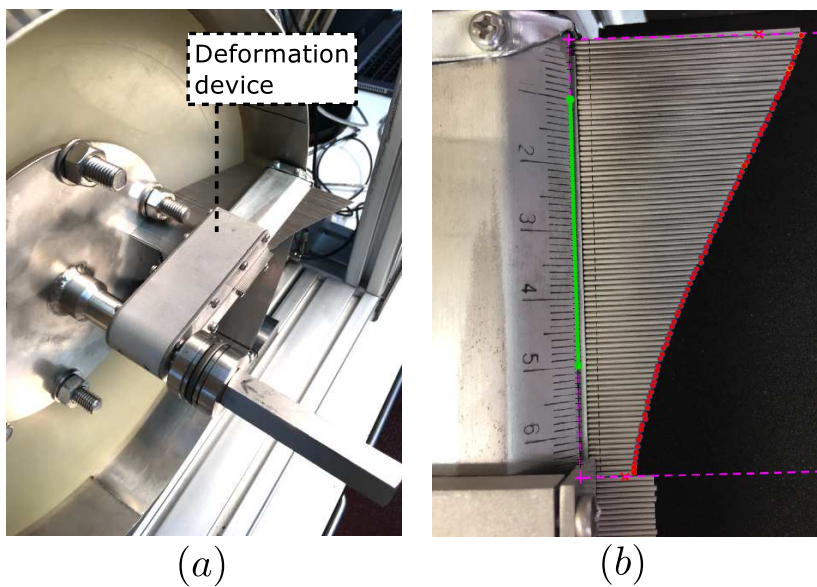


Figure 3.3: (a) Profile comb. (b) Deformation extracted from the profile comb.

Next to the forces that act on the sealing disc also the deformation of the sealing disc is measured. This is done by mounting a profile comb on the spacer disc, see Figure 3.3. The profile comb is subsequently pressed against the sealing disc in order to measure the shape. The rotation of the profile comb can be adjusted which allows to measure the deformation at different positions. Deformation measurements in addition to force measurements provide a more complete set of results compared to force measurements alone, as was done in [34]. Figure 3.3a shows the profile comb in a 3 o'clock position, but also the 12 o'clock and 6 o'clock position have been employed. These different positions allow to verify if the deformation of the sealing disc is axisymmetric. A camera holder is used to take a photo in the same plane as the profile comb. Subsequently the deformation is obtained by extracting the position of the pins using image processing. The detected location of the

pins is shown by the red dots in Figure 3.3b. Even though this study focuses on pigs with a sealing disc, the experimental setup could be used to study other types of pigs, such as pigs with cups or foam pigs [74]. In case of foam pigs it however makes less sense to attempt to measure any deformation in axial direction, as a foam pig is mainly compressed in radial direction. In the next section the measurement procedure and a typical result obtained from the force sensors are discussed.

3.2.1.1 Measurement procedure

The measurements were performed with two 24-bit GSV-2TSD-DI data acquisition devices connected to a 1 kN and 2 kN load cell (KD40S, ME-Systeme) which record the circumferential force F_1 and the axial force F_2 , respectively. The measurements were performed at a sample frequency of 10 Hz and logged onto a computer. The procedure of a typical measurement is as follows. First, the disc is brought to a specific oversize by applying a force F_1 which reduces the diameter of the hull. The oversize is kept fixed within one experiment. Subsequently, the disc is step-wise displaced in axial direction resulting in a force F_2 . One step corresponds to a rotation of the screw that can be seen in Figure 3.2b. The lead of the screw is 1.5 mm. One rotation is made in approximately 30 seconds to maintain static equilibrium. The axial force F_2 is increased up to a predetermined maximum which is just below the value which would result in the disc moving over the steel ring, see Figure 3.2d. After reaching a maximum value, F_2 is decreased in steps to come back at a value of 0 N. This procedure is repeated three times per measurement. Figure 3.4a shows one typical time series of measurement data which were obtained by applying the procedure to disc B subjected to an oversize $\Delta = 4\%$.

Figure 3.4a clearly shows the stepwise behaviour in the forces, which corresponds to the stepwise adjustment of F_2 as explained above. It is noted that an increase in F_2 corresponds to a decrease in F_1 and vice versa. This is expected as the disc is not only deformed by a wall normal force (related to F_1), but also by a friction force (equal to F_2). The corresponding value of the force ratio μ according to equation 3.9 is included in Figure 3.4a. For the axial force F_2 three zones can be distinguished: a rise zone, where F_2 increases, a rest zone, where F_2 does not change and a relax zone, where F_2 decreases. The rest zone lasts longer and is noisier compared to when F_2 is increasing, because here the profile comb is used to determine the deformation at three different positions on the sealing disc: 12 o'clock, 3 o'clock and 6 o'clock.

Figure 3.4b shows an alternative way of plotting the same data. The forces F_1 and F_2 are now plotted as function of μ . The data are colour coded to distinguish between the rise, relax, and rest zones. In this plot now all three time series of the measurement are included. The inset in Figure 3.4b shows a close up of the data. The data from the three data sets are very close to each other, which thus confirms the excellent reproducibility of the experiment. It can also be seen that the data from the relax zone, as shown in blue,

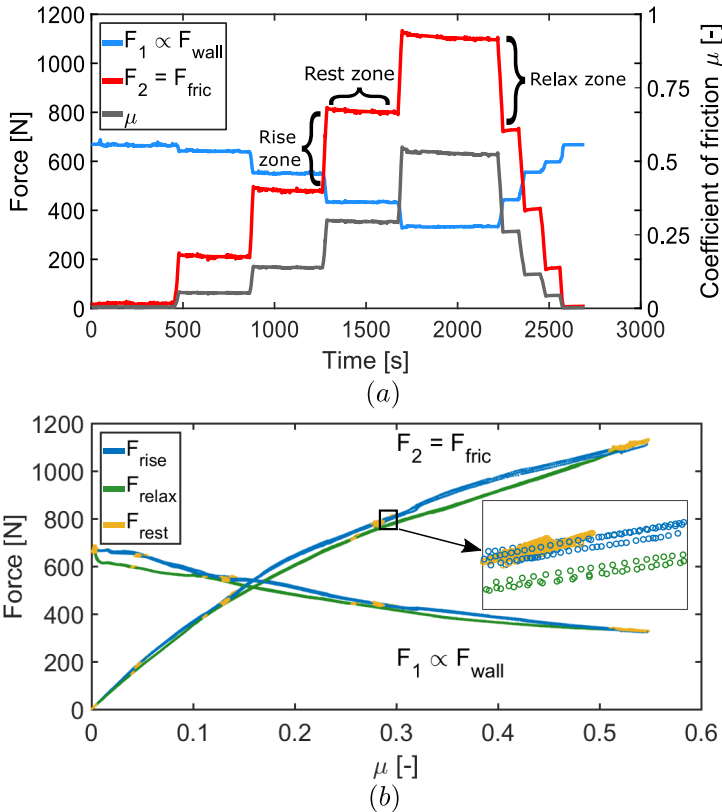


Figure 3.4: (a) Time series of typical force data and corresponding force ratio as obtained in the experiment. (b) Force data plotted as function of the force ratio μ . A close-up of the data between μ equal to 0.29 and 0.31 is included.

differ from the data from the rise zone, which points out that a small hysteresis is present in the experiment.

A total of six different sealing discs have been used in the experiments as listed in table 3.1. Disc A and disc B were tested at four oversizes: 1%, 2%, 3% and 4%. Deformations were measured for disc A and disc B. Similar sets of experiments are conducted for disc C till disc F at oversizes of 3% and 4%. Deformations are not measured for these discs. Comparing the results for disc C, D and E will show how the thickness affects the friction force at different μ values, as the discs are identical except for their thickness. Comparing the results of disc D and disc F will show how the E-modulus affects the friction force at different μ values, as these discs are identical except for their E-modulus. The results of the static measurements will be presented and discussed in Sections 3.3.1 and 3.3.2.

3.2.2 DYNAMIC PIG PULL FACILITY

To study the dynamic friction force a new dynamic pig pull facility has been designed, see Figure 3.5. The setup consists of a 1.7 m vertical carbon steel pipe through which a sealing disc can be pulled at a preset velocity using a linear actuator. The inner radius of the pipe is 157 mm. The linear actuator (Thomson, ECT130) is connected to a brushless AC servomotor (AKM63), which is located at the top end of the pipe. The actuator is able to translate a spindle which has a total length of 2 m and a lead of 20 mm. At the lower end of the spindle a 5 kN load cell (AXH Scaime) is connected to which the sealing disc is attached, see Figure 3.5a/b. The load cell is able to directly measure the propulsive force which is needed to pull the sealing disc through the pipe. Simultaneously the position, velocity and acceleration are monitored with a logging frequency of 200 Hz. The speed of the sealing disc can be varied between 5 and 300 mm/s. The pipeline is placed vertically which makes it possible to add liquids uniformly on top of the sealing disc, see Figure 3.5a. Herewith the effect of possible lubrication on the frictional force caused by the presence of a liquid can be investigated. For a sealing disc moving in an upwards direction in the pipe, the steady state force balance reads:

$$F_m = F_{\text{fric}} + F_g, \quad (3.10)$$

where F_m is the propulsive force of the servomotor, F_{fric} is the friction force between the sealing disc and the pipe wall and F_g is the gravitational force. In dry experiments F_g is due to the mass of the sealing disc and of the spacer discs. In wet experiments also the mass of the lubricant supply on top of the disc has to be taken into account.

A by-pass is created by drilling three holes in the spacer discs, see Figure 3.5a. For the wet experiments, this allows the lubricant to flow through the disc into the leakage tray when the liquid level equals the height of the upper spacer disc. With a minimum amount of lubricant a wet sliding contact can be obtained.

3.2.3 MEASUREMENT PROCEDURE

Rather than a parameter study, as is conducted with the static pig pull facility, only one disc (disc A) is used in the dynamic pig pull experiments as case study. A measurement commences with the spindle in its most extended position with the sealing disc mounted on it (approximately 30 cm below the pipe), see Figure 3.5b. This is called the home position of the disc. From here the sealing disc is pulled slowly at a velocity of 5 mm/s to the initial position, which is 50 mm into the pipe. The disc is kept in this position for 60 seconds to make sure that possible settling effects are no longer present. After this delay time the actual pull test begins and the disc accelerates, moves up through the pipe at the preset velocity, and then decelerates until rest in its final position at the top of the pipe.

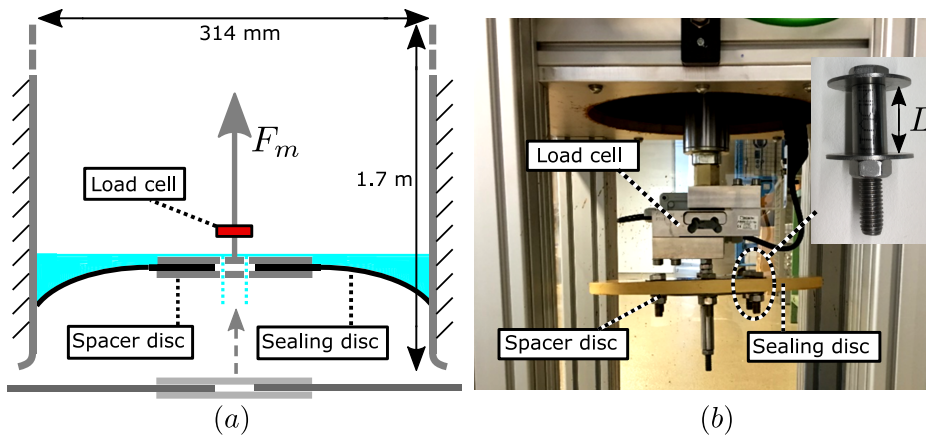


Figure 3.5: (a) Schematic of the dynamic pig pull facility (b) Photograph of the dynamic pig pull facility

Three preset velocities have been used: 100, 200, and 300 mm/s. The spindle acceleration and deacceleration are set to 100 mm/s^2 . When the disc is moving up, both the motion (position, velocity, and acceleration) and the propulsive force are monitored. No data are logged when the disc moves back down, as only pull tests are considered in this study.

In the wet experiments an additional step is added to the procedure. After the disc is positioned in the start position, water is inserted from a small tap at the top of the pipeline until it starts leaking through the by-pass holes, see Figure 3.5a. The top part of the sealing disc and the adjacent pipe wall are now wetted. Subsequently, the tap is closed and the leakage tray is emptied before it is put back under the pipe. The pull test can now begin. When the disc is moving upwards the water leaking past the sealing disc or through the by-pass holes is negligible. In this way it is thus possible to create a wet contact between the pipe wall and the sealing disc. At the end of the pull test the disc is returned back to its start position. When the disc starts moving down it buckles to the opposite side and as a result the water flows through the by-pass holes and is collected into the leakage tray. The mass of the water (approximately 1 litre in volume) is determined and used in the force balance, see Equation 3.10. In this study only water is used as lubricant.

The two spacer discs are separated by a small length of tube, and this tube therefore determines how tight the sealing disc is clamped between the spacer discs. Three configurations are created by selecting three values for the length L of the tube which is shown Figure 3.5b. To the best knowledge of the authors the effect of this parameter on the frictional force of a sealing disc of a pig has not been reported in previous studies. As will become clear in Section 3.3.3 the length L of the tube influences the outer diameter of the sealing disc, and therefore the oversize, due to the nearly incompressible behaviour of the polyurethane. For all three configurations wet and dry experiments are conducted at varying speeds. Each separate experiment is repeated five times for reproducibility purposes;

the first two runs are used to mitigate any settling effects of the disc and the last three runs are used in the actual analysis. Next to the variation of L the disc is placed in both a face up and face down orientation to investigate the presence of any possible asymmetries.

3.2.4 FINITE ELEMENT MODEL

Comsol Multiphysics (version 5.2) is used in this study for the Finite Element (FE) analysis. We solve the structural mechanics problem in which we solve for the deformation of the sealing disc which is caused by the wall force and the friction force which act on the chamfer of the sealing disc, see Figure 3.6. We consider static equilibrium, in which case Newton's second law reads:

$$\nabla \cdot \sigma = 0. \quad (3.11)$$

Here σ is the Cauchy stress tensor. The stresses are calculated using a linear isotropic material model. The E-modulus which is used has been determined by material tests and can be found in Table 3.1. The Poisson's ratio ν is taken equal to 0.49. Since the typical deformation which occurs can be in the order of a few times the thickness of the sealing disc, a nonlinear geometry model is used. We assume an axisymmetric geometric model.

Figure 3.6 shows the typical mesh which is used for the calculations. Second order quadratic elements are used. The meshing is adapted on the thickness of the disc to guarantee appropriate meshing for both thick and for thin discs. In the thickness direction the size of the element is controlled between a minimum size of $t/6$ and a maximum size of 1.2 times $t/6$. In the radial direction the edges have a length equal to the edges in the thickness direction multiplied by a factor 1.5. The mesh consists of approximately 400 elements, which was verified to be sufficiently fine by making a comparison with simulation results with a smaller number of elements.

The green lines in Figure 3.6 represent roller boundary conditions on both sides of the sealing disc between $r = 0$ and $r = r_p$, due to the spacer discs. Here the sealing disc is constrained to move in the normal direction, but it is allowed to move parallel to the spacer discs. The freedom to move, however, is limited, due to the axisymmetric geometry. It was found that this boundary condition is appropriate to model the confinement of the spacer discs, even though a finite, non-zero clamping force of the spacer discs on the sealing disc exists. An alternative boundary condition could be a completely clamped boundary condition [69], which would prohibit any movement of the disc in the region of the spacer discs. This was found to be unsuitable, as a finite deformation was observed in the region of the spacer discs, which will become clear in Section 3.3. The blue square represents the chamfer of the disc, where the wall force and the friction force act. The chamfer size c is set to 1.4 mm, as measured from the sealing disc. The remaining edges have a free boundary condition.

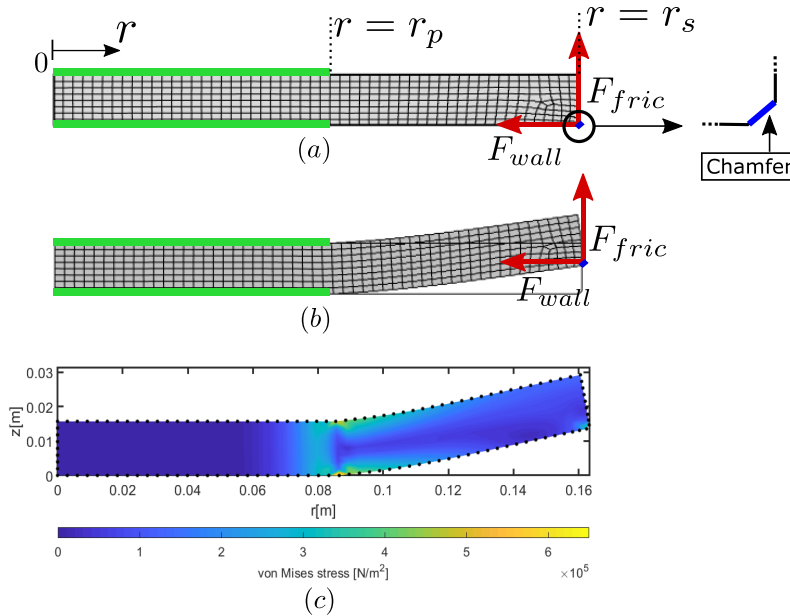


Figure 3.6: Geometry and boundary conditions of the finite element model. (a) Initial geometry. (b) Deformed geometry. (c) Typical simulation result.

For low μ values high wall forces are involved when a sealing disc is confined inside a pipe. In reality and in the experiments in this study a sealing disc automatically buckles backwards with respect to the moving direction. To ensure that in the FE model the disc buckles to the correct side the FE model is solved in multiple steps. First the friction force is added and then the wall force is increased in steps to its final value. Within the solution process, the result of the previous calculation step is used as an initial condition for the next calculation step. This helps to buckle the disc in the direction of the friction force. Figure 3.6c shows a typical simulation result of disc A subjected to a wall force $F_{wall} = 400$ N and a friction force $F_{fric} = 200$ N. The interior of the disc is color coded by the von Mises stress. High stress points typically occur near the outer edge of the spacer discs.

3.3 RESULTS

In this section the results are presented which are obtained by the methods described in the previous Section 3.2. First the results from the static experiment are presented. In Section 3.3.1 the deformations obtained in the experiments and the deformations found using the FE model are compared for disc A and disc B, see Table 3.1. In Section 3.3.2 the friction force as a function of μ and oversize is shown, both for disc A and for disc B. In addition, Section 3.3.2 shows the friction force for different values of the E-modulus and the thickness of the disc. For this purpose discs C to F are used. Section 3.3.3 present the

results which are obtained with the dynamic pig pull experiment. Section 3.3.4 discusses how the results from the static and dynamic pig pull experiments are related.

3.3.1 SHAPE COMPARISON

We have obtained the shape of the sealing disc using the deformation device as described in Section 3.2.1. Figure 3.7 shows the results for disc A subjected to 3% oversize. In Figure 3.7a a time series is shown, where the blue line denotes the wall force F_{wall} and the red line denotes the friction force F_{fric} . In the first five rest zones, where the forces are constant, the deformation of the disc is measured. To show how the measured shapes compare with the FE model, data from the last three rest zones are shown in Figure 3.7b-d. The last three rest zones which correspond to sub-figure b-d are indicated in Figure 3.7a.

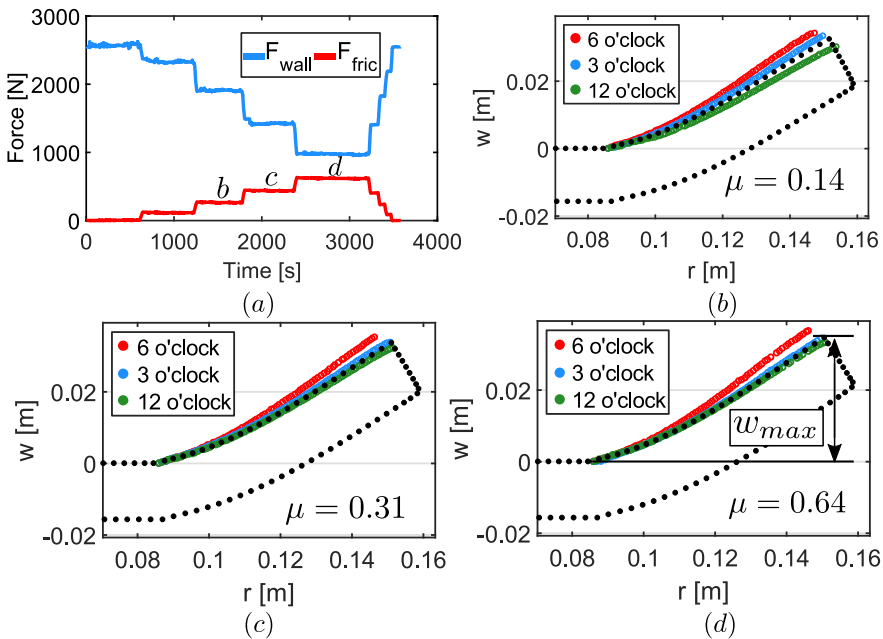


Figure 3.7: Experimental results for disc A at 3% oversize. The black dotted shape in sub-figures b-d represents the FE model. (a) A time series showing the wall force and the friction force. Deformations are measured in the rest zones labeled b-d. (b) $F_{\text{wall}} = 1908$ N and $F_{\text{fric}} = 266$ N. (c) $F_{\text{wall}} = 1429$ N and $F_{\text{fric}} = 439$ N. (d) $F_{\text{wall}} = 977$ N and $F_{\text{fric}} = 620$ N.

It can be seen that the FE results, which are shown by the black dots, agree very well with the average measured deformation. The FE results were obtained by applying the forces that were measured in the experiment to the chamfer of the disc in the FE model, as described in Section 3.2.4. It can also be noted from the measured data that the sealing

disc does not deform perfectly axisymmetrically in the hull. The largest deflection occurs when the deformation device is at 6 o'clock, followed by 3 o'clock and 12 o'clock. This is a consequence of the position of the tensioning mechanism located at 6 o'clock, see Figure 3.2a. This breaks the axisymmetry of the hull, resulting in a slightly non perfect circular shape. No attempt has been made to correct this, since adding new forces to the system was not desired. The gravity force is assumed to play a minor role as it is only a small fraction of the encountered wall forces.

In Figure 3.7b-d the force ratio μ varies from 0.14 to 0.64 which corresponds to a substantial variation in F_{wall} and F_{fric} , see Figure 3.7a. The deformation of the disc during this process, however, only changes slightly. Both the measured data from the deformation device and the FE model show this behaviour. This means that there exists approximately one axisymmetric shape of the sealing disc which is fitted in a pipe, and that the effect of μ on the final shape is only minor. As was discussed in Section 3.2.4 a roller boundary condition was chosen to represent the confinement of the spacer discs. It can be clearly seen that the angle of deformation is not zero at the radius of the spacer disc $r = r_p$, which supports the choice of a roller boundary condition over a fully clamped boundary condition.

The deformation results for disc A at 3% oversize were shown in Figure 3.7 as case example. The deformations results of disc A for all oversizes 1%, 2%, 3%, and 4% are presented in Figure 3.8a. Here the maximum deformation w_{max} , which occurs at the tip of the disc is selected, see Figure 3.7d, and is plotted as function of μ .

The experimental data in Figure 3.8a are plotted as error bars in different colours which correspond to different oversizes. The lower and upper limit of the error bar represent the deformation measurements at 12 o'clock and 6 o'clock, respectively, while the main data point (open circle) of the error bar represents 3 o'clock, see Figure 3.7. The green error bars connected with the black line in Figure 3.8a link to the deformation results in Figure 3.7, as here an oversize of 3% was shown. The black line shows that w_{max} only increases by a few millimetres while μ increases significantly. At every oversize the experiment was conducted three times. The fact that the three corresponding error bars are lying on top of each other indicates that the experiment is reproducible. The same procedure was applied to disc B. These results are summarized in Figure 3.8b. It can be concluded that the FE model is able to predict the shapes and w_{max} obtained in the experiment. Only for small μ no FE data are plotted. Here the FE model returns a solution buckled to the other side. In general it is found that μ does not have a large effect on how the disc is fitted in the pipeline. It is evident that the oversize does have a large effect on the shape, as a larger oversize means that the disc has to deform more to fit in the pipe. The length of the error bars in Figure 3.8b is longer, indicating that there is a larger spread between the deformation measurements at 3, 6 and 12 o'clock. This can be explained by the larger E-modulus of disc B, as this stiffer disc is more sensitive to any asymmetries in the setup. The results in Figure 3.7 and Figure 3.8 are obtained without using a fitting parameter for the E-modulus. The E-modulus used in the FE model is shown in Table 3.1

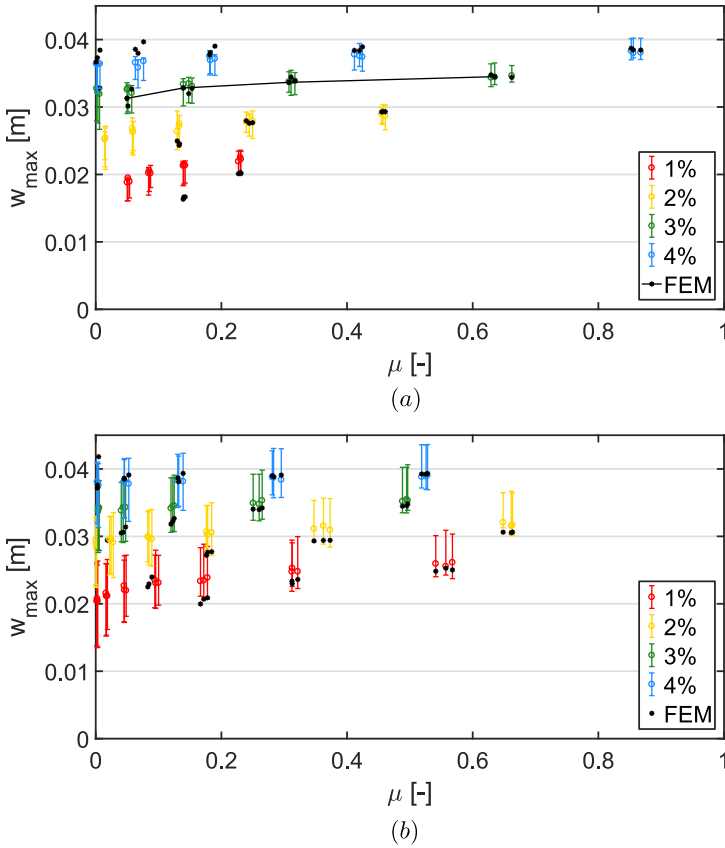


Figure 3.8: Comparison of w_{\max} in the experiments and in the FE model for different oversizes. (a) Disc A. (b) Disc B.

and is obtained in stress and strain tests as described in Table 3.1. In the next section various parametric studies are described, in which also the effect of a variation in the E-modulus on the friction force is discussed.

3.3.2 PARAMETER STUDY

Figure 3.9 shows the friction force in the rise and rest zones as function of the force ratio μ for the four oversizes for disc A and disc B. The corresponding wall force F_{wall} can be obtained as the ratio of F_{fric} and μ .

A first inspection of Figure 3.9 shows that the friction force of disc B is overall higher than the friction force of disc A. This is a consequence of the higher E-modulus of disc B compared to disc A, see Table 3.1. The maximum μ values obtained differ per oversize and per disc, indicating that the discs start to move over the steel ring (Figure 3.2) at a

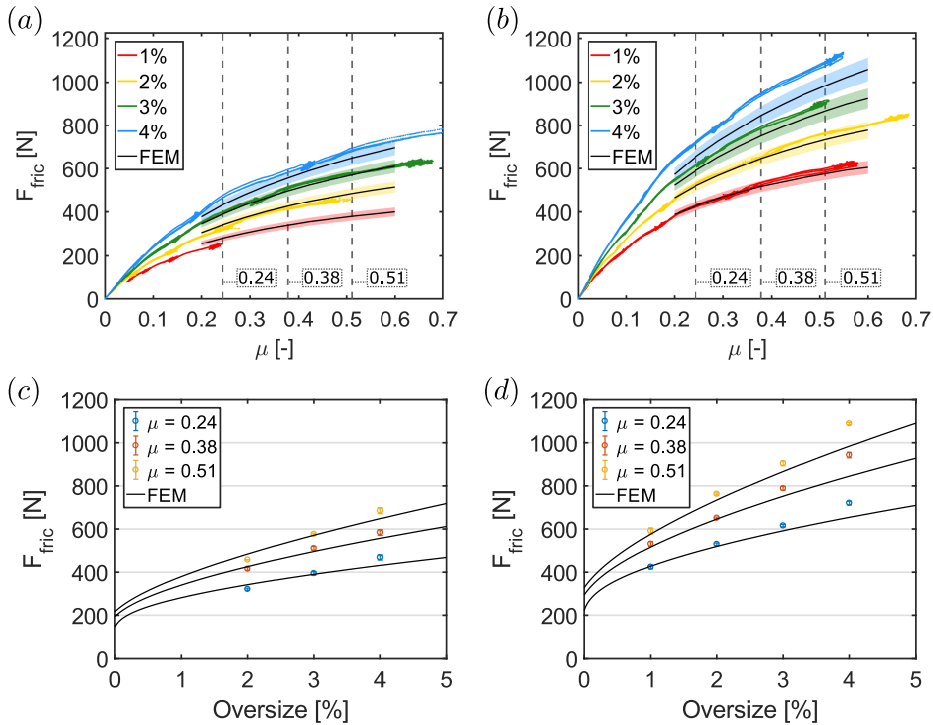


Figure 3.9: (a) Friction force as a function of μ for different oversizes for disc A (b) Idem disc B. (c) The friction force as a function of the oversize for disc A (d) Idem disc B.

different critical value of μ . The generic trends observed for all oversizes are similar for both discs. We focus on the μ regime between 0.2 and 0.6.

In the chosen μ regime also FE simulation results are shown in black. The black lines are fitted through 10 data points. For these data points at different μ the friction force (and thus the wall force as μ is fixed) is increased until the FE model reaches the same oversize (1-4%) as in the experiment. The shaded regions around the black lines show the results of a variation by $\pm 5\%$ of the E-modulus used in the FE model.

The friction forces necessary to bring the disc in the desired oversize in the FE model correspond very well to the experiments. Both the trend and the actual magnitudes are captured accurately by the FE model. Figure 3.9a shows that the experimental results and the FE results agree very well for disc A with oversizes 2% and 3%. The FE model predicts a lower friction force to bring the disc in 4% oversize. The maximum deviation at 4% oversize is only 9.3%. At 1% oversize no experimental data are available in the chosen μ regime. For disc B, shown in Figure 3.9b, the results are in agreement for the 1% and 2% oversizes. For the 3% and 4% oversizes the FE model underpredicts the friction force, with a maximum underprediction by 5.2% and 11.6%, respectively.

Both Figure 3.9a and Figure 3.9b show that the experimental friction force data are approximately evenly spaced when the oversize increases from 1% to 4%. For the FE data the increase in friction force seems to decrease as the oversize increases. A reason for this difference in behaviour might be that the wall force is incorrectly captured at higher oversizes (and thus higher friction forces) in the experiments. To capture the wall force correctly six ball bearings were added to the setup, see Section 3.2.1. This was to make sure that no undesired forces were added in the plane of the hull, affecting F_1 . For high friction forces the contact between the hull and the ball bearings connected to the frame may still not be completely frictionless. Undesired friction between the hull and the frame is difficult to prevent completely. Therefore the force sensor monitoring F_1 may overpredict the wall force. This means that μ is underpredicted for the experimental data in Figure 3.9. There is no reason to assume that the experiment does not capture the friction force correctly. When this hypothesis is true the experimental data would shift to the right for high friction forces. Intuitively, the FE data make sense as one may expect that it is easier to increase the oversize from 3% to 4% than from 1% to 2%. This is also what has been observed in other research [69, 100]. To directly see the effect of the oversize on the friction three values of μ have been highlighted in Figure 3.9a and b. Along these lines of constant μ experimental data have been gathered in a range between $\mu + 0.002$ and $\mu - 0.002$. The error bar represents the standard deviation of the data within this range.

Disc D and disc F are tested to see how the friction force behaves as a function of the E-modulus. Figure 3.10a shows the results when the disc is at 3% oversize and Figure 3.10b for 4% oversize. The discs have similar specifications except for the Shore hardness and the E-modulus, see Table 3.1. The thickness and the sealing disc radius are not exactly the same; therefore in the FE model the average thickness and radius are selected. The results are shown for three different values for μ . For the disc with the lower Shore hardness and E-modulus (disc F) the experimental data agree very well with the FE data for all three values of μ . The maximum deviation in friction force between the FE results and the experiments equals 6.5%. The results of the experiments with the stiffer disc show higher friction forces than predicted by the FE model, especially at 4% oversize. The maximum deviation in friction force between the FE results and the experiments equals 14.7%. This is in line with the observation in the previous section that F_{wall} is not captured correctly in the experiment for high friction forces. When F_{wall} is overpredicted, μ is underpredicted. Figure 3.10 shows that lower μ values would correspond to a smaller gradient in the experimental data. It is worth mentioning that the experimental setup which is designed can actually serve as a tool to predict the E-modulus of a sealing disc in a non destructive way by fitting the experimental data on the FE results.

Disc C, disc D and disc E are tested to see how the friction force behaves as a function of the disc thickness. The discs have the same manufacturer and are from the same batch. Only the thickness of the discs is different, see Table 3.1. Therefore the E-modulus of disc C and disc E have not been obtained in a stress and strain test, but are assumed to be equal to the E-modulus of disc D. Figure 3.10c shows the friction force with μ being equal to

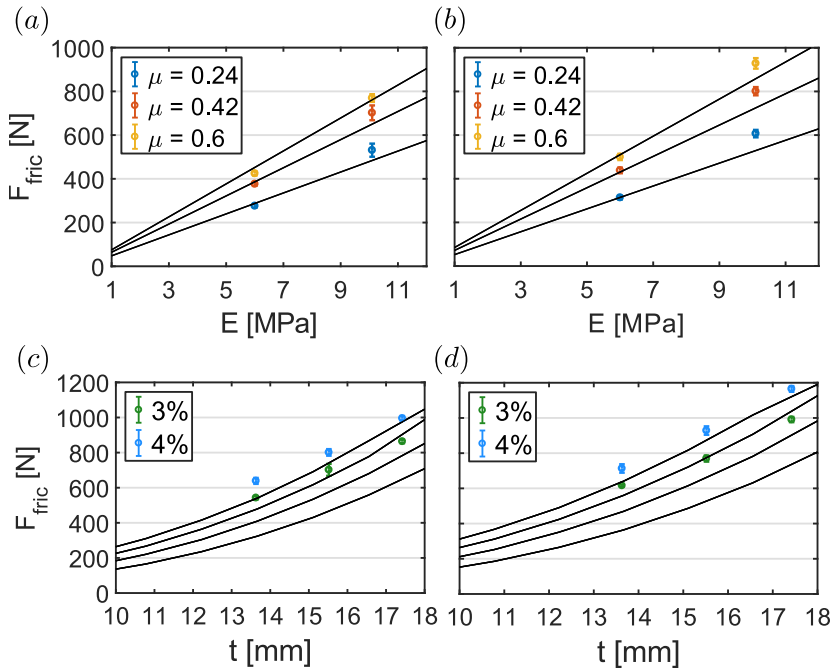


Figure 3.10: The black line represents results from FE calculations. (a) The friction force as a function of the E-modulus at 3% oversize. (b) The friction force as a function of the E-modulus at 4% oversize. The experimental results are compared to the FE results at three μ values: 0.24, 0.42 and 0.6. (c) The friction force as a function of the thickness at μ equal to 0.42. (d) The friction force as a function of the thickness at μ equal to 0.6. Disc C, disc D and disc E are tested at 3% and 4% oversize. The FE results correspond to, from top to bottom, 4%, 3%, 2% and 1% oversize.

0.42. Experimental data are shown at 3% and 4% oversize. The FE model is shown for an oversize of 1%, 2%, 3% and 4%. The maximum deviation in friction force between the FE results and the experiments equals 18.1%. This deviation occurs for disc C at 4% oversize. Figure 3.10d shows similar data with μ equal to 0.6. Here the maximum deviation in friction force between the FE results and the experiments equals 11.2%, also occurring for disc C at 4% oversize. For the two thicker discs the FE model agrees very closely with the experimental data while the friction forces for the thinnest disc are underpredicted.

3.3.3 RESULTS FROM DYNAMIC PIG PULL EXPERIMENTS

In this section the experimental results from the dynamic pig pull experiments are presented. All experiments are conducted with disc A. As was discussed in Section 3.2.3 the length of the tubes L which defines the distance between the spacer discs was varied. Thereby the clamping force of the spacer discs which squeezes the sealing disc is varied.

The reduction in the length compared to the original length when the clamping force is zero is defined L' . Three values for L' have been studied: 0, 1, and 2 mm. As the original thickness of disc A is equal to 15.9 mm (see Table 3.1), values of L' equal to 0, 1, and 2 mm correspond to a compression of 0%, 6%, and 13% respectively. The compression in the axial direction causes the disc to expand in radial direction, due to the nearly incompressible behaviour of polyurethane. As a result the outer diameter increases. This has been quantified, see Table 3.2. Here it can be seen that for $L' = 0$ the original radius of the disc equals $r_s = 162.2$ mm. As the inner radius of the pipe is 157 mm, this corresponds to an oversize of $\Delta = 3.33\%$. Upon increasing the clamping force by increasing L' the radius and corresponding oversize thus increase.

Table 3.2: Oversizes before and after a first pull test.

L' [mm]	Before pull test		After pull test	
	r_s [mm]	Δ [-]	r_s [mm]	Δ [-]
0	162.2	3.33	162.2	3.33
1	162.7	3.64	162.9	3.74
2	163.3	4.04	163.7	4.24

For the tubes that squeezed the disc by 1 mm or 2 mm the disc oversizes were slightly higher after a first pull test, compared to the oversize measured directly after assembling the spacer discs on the sealing disc. For the tubes that were not squeezing the disc ($L' = 0$ mm) this phenomenon was not observed. This indicates that a small settling effect is present which can be explained by the forces that occur in the experiment that are able to pull the disc radially outward. When the clamping force is zero ($L' = 0$) the disc is able to retract to its original position, but with a non zero clamping force ($L' = 1$ and $L' = 2$) the disc remains radially extended. This settling effect is not investigated further in this work.

The effect of L' on the frictional force is investigated for various disc speeds. Also the effect of a dry versus a wet contact is investigated, as described in Section 3.2.3. The experiments and corresponding parameters are summarized in Table 3.3. Here it is also shown that also a face up and face down orientation of the disc is distinguished. The average values of the force data are listed as found when the disc is moving at constant velocity, as described in Section 3.2.3. The sequence of the experimental runs can be deduced from the table: first the runs without squeezing are conducted, followed by the runs with 1 mm and 2 mm squeezing. For one set of tubes we start with the dry runs: first five runs at 100 mm/s followed by five runs at 200 mm/s and 300 mm/s. After this, the dry face down, wet face down and wet face up runs are performed. Before the experiments with the next set of tubes are conducted, the setup is left for an entire day to dry. The experiments in Table 3.3 correspond to approximately 600 m of pipeline pigging (three sets of tubes, four configurations, three speeds, five repetitions, 3.2 m between subsequent

pull tests). The values in Table 3.3 are average values based on the last three runs from each set of five runs, as the first two runs are done to mitigate any settling effects.

Table 3.3: Experiments performed with three sets of tubes: 0 mm (no squeezing), 1 mm and 2 mm. The mean values of the force data are tabulated, averaged over three runs and as found when the disc is moving at constant velocity. In addition, the standard deviation for this period is added between brackets. In total the runs correspond to 600 m of pigging distance.

L' [mm]	Speed [mm/s]	Friction force [N]			
		Dry, face up	Dry, face down	Wet, face down	Wet, face up
0	100	819 (1.2)	815 (1.9)	680 (9.7)	702 (3.9)
	200	824 ^b (1.4)	814 (1.3)	682 (5.3)	710 ^b (2.3)
	300	830 (1.2)	815 (1.0)	685 (1.2)	713 (2.1)
1	100	843 (2.4)	828 (3.1)	701 (3.6)	717 (1.8)
	200	845 ^b (2.2)	828 (1.7)	700 (2.0)	722 ^b (3.0)
	300	844 (1.3)	830 (1.0)	700 (1.9)	720 (2.6)
2	100	836 ^a (2.6)	817 ^a (3.4)	705 (4.8)	733 (3.6)
	200	839 ^{ab} (2.4)	822 ^a (4.1)	716 (3.6)	739 ^b (4.5)
	300	842 ^a (1.6)	827 ^a (2.6)	718 (2.7)	738 (3.0)

^a Figure 3.11 shows one of the three time series on which this value is based.

^b Figure 3.12a shows the three time series on which this value is based.

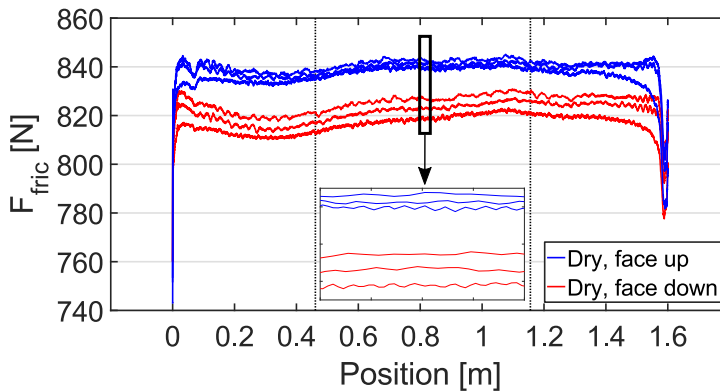


Figure 3.11: Friction force during dry, dynamic tests in two orientations (face up, face down) as function of disc position for $L' = 2$ mm at three pull velocities: 100 mm/s, 200 mm/s, and 300 mm/s. The zoomed section shows the velocity dependence of the friction force; a higher friction corresponds to a higher velocity.

We will now highlight some results from Table 3.3 by looking at the time series on which the values in the table are based. Figure 3.11 compares the dry face up and dry face down

experiments for different velocities. The tubes that are squeezing the disc by 2 mm are used. The black dotted vertical lines indicate the range in which the discs are moving at constant speed. A slight velocity dependence is observed in the friction force. The zoomed section shows that higher velocities correspond to higher friction forces. The increase was, however, not significant. A maximum increase by 1.7% between 100 mm/s and 300 mm/s is found when looking at all experiments in Table 3.3. This means that in this parameter regime the value for the sliding friction can be regarded as approximately constant. At higher velocities, however, this may not be the case, as the friction coefficient will be dependent on the relative velocity of the sliding interfaces [20]. Figure 3.11 and Table 3.3 show that higher friction forces are measured with the face up configurations, compared to the face down configurations. In the dry experiments the friction forces are higher by 0.5%-2.5%, while in the wet experiments the increase is 2.3%-3.9%. The difference in friction forces when comparing the face down and face up configurations can possibly be explained by a different chamfer on both sides of the sealing disc which introduces an asymmetry. Small changes in the size of the chamfer can have a significant effect on the force, as will be discussed in Section 3.3.4.

Figure 3.12a shows the results for the dry and wet experiments (both with a face up configuration) at 200 mm/s for the three values of L' : 0, 1, and 2 mm. The effect of lubrication is clearly visible as the measured friction force for all the wet experiments is lower than for the dry experiments. Looking at the columns with the dry and the wet experiments in Table 3.3, the friction forces decrease between 12% and 16% in the wet experiments compared to the dry experiments. When focusing on the three curves of the wet experiments in Figure 3.12a we note the following trend. An increase by 1.8% for the friction force is observed with 1 mm squeezing compared to the case without squeezing. A further increase by 2.4% is found when the squeezing is increased from 1 mm to 2 mm. This is equivalent to a total increase by 4.2% when the squeezing is increased from no squeezing to 2 mm squeezing in the wet runs at 200 mm/s. This leads to the conclusion that the increase in oversize caused by the clamping force, see Table 3.2, does increase the friction force.

When focusing on the dry experiments in Figure 3.12a we observe an increase in friction force by 2.6% for the dry runs with 1 mm squeezing compared to the dry runs without squeezing. When increasing the squeezing from 1 mm to 2 mm in the dry runs, however, a slight decrease in friction force by 0.6% is observed. This is not expected as the increase in oversize due to the increase in L' is expected to increase the friction force further. This leads to the hypothesis that wear of the sealing disc was not negligible during the course of taking experiments with the different sets of tubes (equivalent to $600/3=200$ m of pigging). The effect of wear is expected to decrease the friction force, which would oppose the increase in friction force due to increasing L' . To test this hypothesis an additional set of dry experiments is performed, in which the runs are performed directly after each other. All runs were conducted at a velocity of 200 mm/s; first five runs without squeezing, followed by five runs with 1 mm and 2 mm squeezing. The results are shown in Figure 3.12b and in

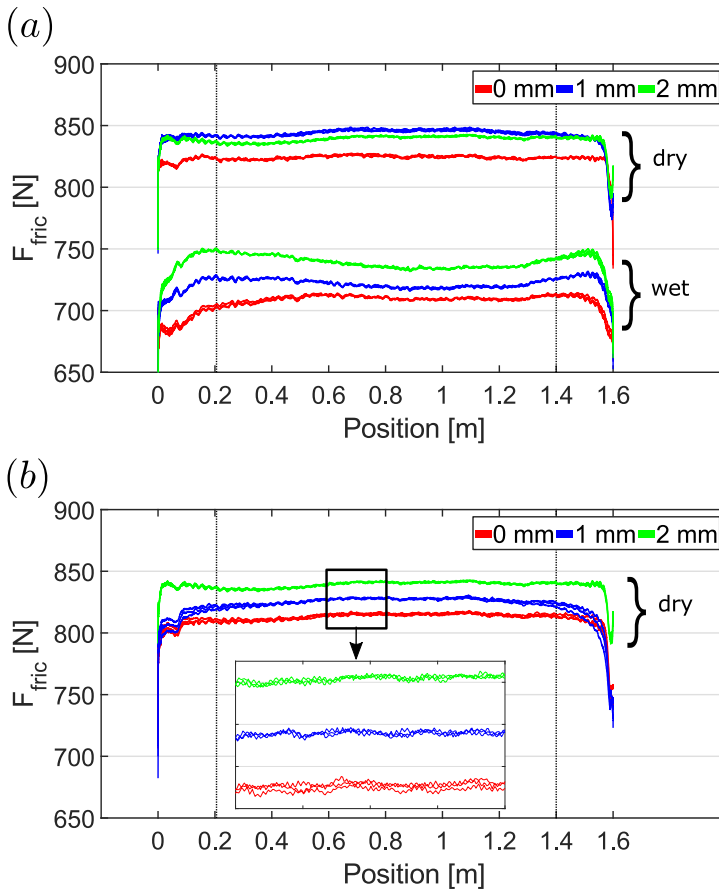


Figure 3.12: (a) Friction force for three different pre-squeeze values and for two lubrication conditions. The pull velocity is 200 mm/s. (b) Friction force for three different pre-squeeze values; the experiments have been conducted directly after each other. The pull velocity is 200 mm/s.

Table 3.4. The inset in Figure 3.12b reveals the individual three time series on which the value in Table 3.4 is based. This shows excellent reproducibility for the subsequent runs. Indeed the friction force increases when the disc is squeezed. An increase by 1.6% is observed with 1 mm squeezing compared to no squeezing and an increase by 1.7% for 2 mm squeezing compared to 1 mm squeezing. Thus a total increase by 3.3% with 2 mm squeezing compared to no squeezing. This confirms the hypothesis that wear is not negligible during the course of taking experiments with the different sets of tubes. Wear can only be approximately ignored when the runs are conducted directly after each other. Indeed, wear is clearly visible upon inspecting the sealing disc. In Figure 3.13 disc A is shown before using it in the dynamic experiments and after all experiments were conducted. It can be seen that the disc is fabricated with a certain chamfer on both sides. After

Table 3.4: Dry runs performed with the three sets of tubes: 0 mm (no squeezing), 1 mm and 2 mm. The mean values of the force data are tabulated, averaged over the five runs and as found when the disc is moving at a constant velocity of 200 mm/s. Every run is repeated five times, corresponding to 50 m of pigging distance. Figure 3.12b shows all force measurements.

L' [mm]	Friction force [N]
0	813
1	826
2	840

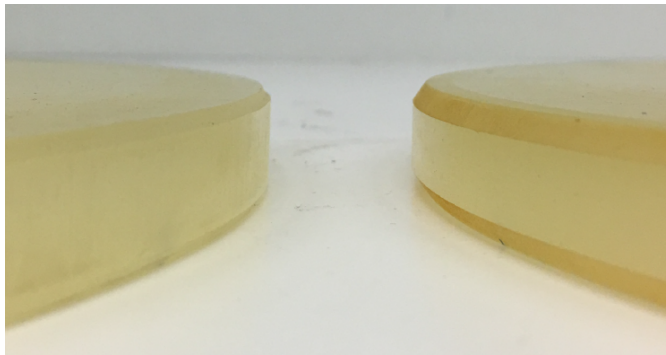


Figure 3.13: The chamfers of disc A are shown. Disc A on the left is not used in the dynamic experiments and reveals the chamfer of approximately 1.4 mm as built-in by the manufacturer. On the right disc A is shown which is used in the dynamic experiments. The wear is clearly visible and the chamfer is 4 mm.

completing all experiments, which means that the disc was used over a distance of approximately 1500 m, the chamfer has increased significantly to a length of 4 mm. In the next section the results of the dynamic experiments will be related to the static experiments as described in Section 3.3.2. The effect of the size chamfer in the translation from static experiments to the dynamic experiments will be discussed.

3.3.4 RELATION BETWEEN STATIC AND DYNAMIC RESULTS

In Section 3.3.2 we have seen that the FE model is able to capture the results obtained in the static setup, using the E-moduli obtained in stress and strain tests without the use of any fitting parameters. It is however not possible to investigate the effect of a possible liquid film between the disc and the pipe wall on the friction factor with this setup, since the experiment is static. In the dynamic experiment it is however possible to investigate the presence of a liquid, as was shown in section 3.3.3. The next step is to relate the static

results to the dynamic experiments. Both experiments measure the friction force, although the wall normal force cannot be measured in the dynamic experiments. We therefore need to deduce μ for the dynamic experiments, using the results from the static experiments.

Figure 3.14 shows the FE prediction of μ for the dynamic experiments, using three values of the chamfer length c . Here the results of the FE model are shown in a similar way as in Section 3.3.2, but now for an oversize of 4.04%. In the static experiments with disc A the tubes were not yet used, but the circumference of the disc after clamping was measured. This circumference corresponds exactly to the circumference of disc A when squeezed by 2 mm in the dynamic experiments. Therefore this oversize was chosen, see Table 3.2.

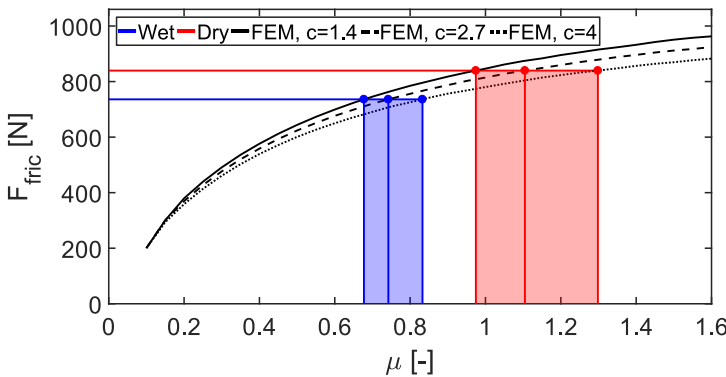


Figure 3.14: Prediction of the μ values in the dynamic experiment, using three values of the chamfer length c . Using the FE results, the force data from the dynamic experiments are translated into μ values. μ is predicted between 0.97 and 1.30 in the dry runs and between 0.68 and 0.83 in the wet runs.

When averaging the friction force for the different speeds for the dry experiments with $L' = 2$ mm (Table 3.3), a value of 839 N is found. Based on this value a corresponding μ value can be determined using the FE model. Wear was observed during the course of performing the dynamic experiments and it was found to increase the chamfer length c , see Figure 3.13. To investigate the sensitivity of the chamfer size on the frictional force the FE calculations were performed with three different chamfer lengths: the original chamfer length $c = 1.4$ mm, the final chamfer length $c = 4$ mm, and an intermediate chamfer length $c = 2.7$ mm. It can be observed that the friction force decreases when the chamfer length increases, as it is easier to subject the sealing disc to 4.04% oversize when the chamfer is larger. This is in line with other research and a consequence is that the required driving pressure needed to propel the pig decreases throughout the course of a pigging run [98]. When we focus on a fixed value of 839 N for the friction force in the dry experiments, we thus find different μ values, ranging between $\mu = 0.97$ and $\mu = 1.30$. The wet experiments correspond to lower friction values, see Section 3.3.3, and therefore lower corresponding

Table 3.5: Force ratio μ versus the chamfer length c .

c [mm]	μ [-], dry	μ [-], wet
1.4	0.97	0.68
2.7	1.11	0.75
4.0	1.30	0.83

μ values are found, see Figure 3.13. The results are summarized in Table 3.5. In the wet contact μ decreases by approximately 30%. An interesting follow-up experiment could be to use a biological or mineral oil as lubricant in the dynamic pig pull experiments.

3.4 CONCLUSIONS

A static and dynamic experimental setup have been designed to investigate the frictional behaviour of a sealing disc of a pipeline pig. The static setup has been used to systematically study the effect of various parameters including the oversize, force ratio, thickness and E-modulus. In this way the study contributes to the fundamental knowledge on parameters influencing the friction force in pigging applications. Being able to test sealing disc configurations for different values of the force ratio μ is important for the industry as μ is often unknown and may vary a quite substantially.

A finite element (FE) model was built which was able to accurately capture the behaviour of the experiments. The finite element model was able to accurately describe the static experiments, by using E-moduli obtained in stress and strain tests and without using any fitting parameters. When similar forces as measured in the experiment are acting on the chamfer in the finite element model, the maximum deformation varies by less than 2 mm for μ values larger than 0.25. Furthermore, the shapes obtained in the experiments agree very well with the shapes obtained with the finite element model. In the current experiment and FE model axisymmetry applies. For future research it could be interesting to investigate the effect of gravity which would break the axisymmetry. This effect is expected to become important when the gravitational forces become comparable with the forces which are purely caused by confining the sealing discs in the pipe.

When the disc is brought to a specific oversize between 1% and 4% in the finite element model, the required forces agree very well with the experimental force data. The maximum deviations for disc A and B occurred at 4% oversize. Here the finite element model underpredicts the friction force by a maximum of 5.2% and 11.6%, respectively. It is hypothesized that this underprediction is explained by undesired friction between the hull and the frame in the experimental setup, which is especially observed at high frictions forces. To test if this hypothesis is correct a setup could be designed which has more roller bearings between the hull and the frame which would result in even less friction.

The dynamic pig pull facility has been used to test the frictional behaviour during a dynamic pull test through a 1.7 meter pipe for both a dry and a wet contact. This dynamic setup is complementary to the static pig pull facility. The influence of the clamping force of the spacer discs on the sealing disc diameter and frictional force has been investigated. It was found that by increasing the clamping force the diameter, and therefore the oversize, of the sealing disc increases. As a result the frictional force was found to increase during the dynamic pull tests. The largest difference in friction force is observed when comparing the dry and the wet experiments. Lubrication was clearly visible in the force measurements. Using water as a lubricant resulted in a decrease in the friction force by between 12% and 16% for the experiments conducted. This decrease in friction force is attributed to a difference in friction coefficient, which has been quantified using FE calculations. The sensitivity of the size of the chamfer in this analysis has been taken into account. This has led to a prediction of the friction coefficient of between 0.97 and 1.30 for a dry contact and of values between 0.68 and 0.83 for a wet contact. Only water has been used as lubricant in the experiments. It is suggested for future research to study also other lubricants, such as for example mineral oil.

4

EXPERIMENTS AND MODELLING OF BY-PASS PIGGING UNDER LOW PRESSURE CONDITIONS

This chapter is adopted from M.H.W. Hendrix, H.P. IJsseldijk, W.-P. Breugem, and R.A.W.M. Henkes, "Experiments and modelling of by-pass pigging under low pressure conditions". In: *Journal of Process Control* 71 (2018), pp. 1-13.

4.1 INTRODUCTION

Pipelines are used in many industries as a means of transporting fluids. Such fluids can consist of gases, liquids, or combinations of gases, liquids and solids. An inevitable consequence is the internal maintenance of those pipelines. In the oil and gas industry this is done by using a pig (Pipeline Inspection Gauge). This is a cylindrical device which travels through the pipeline driven by the fluid flow, see for example figure 4.1. Pigs have a wide range of applicability, including cleaning the inside of a pipeline, removing excessive liquid from a liquid-gas pipeline, or distribution of corrosion inhibitor [15, 74, 94, 96]. Pigs can also be equipped with intelligent sensors which can inspect the inner pipe wall [75], for example. There is a wide variety of pigs to perform these tasks. An example of three common utility pigs are (1) the mandrel pig, (2) the solid cast pig and (3) the foam pig, which are shown in figure 4.1 [74]. A mandrel pig consists of a metal core with elements mounted on this core. It depends on the purpose of the pigging operation which elements are mounted. Typical elements are scrapers for cleaning, guiding discs to ensure a proper alignment with the pipe and sealing elements to seal the pipe. These elements are normally made from polyurethane. A solid cast pig differs from a mandrel pig in the sense that it is made out of one material, often also polyurethane. A foam pig is made of softer material and has a larger volume. The pigging purpose and the costs determine which of the types is most appropriate to perform a pigging operation.

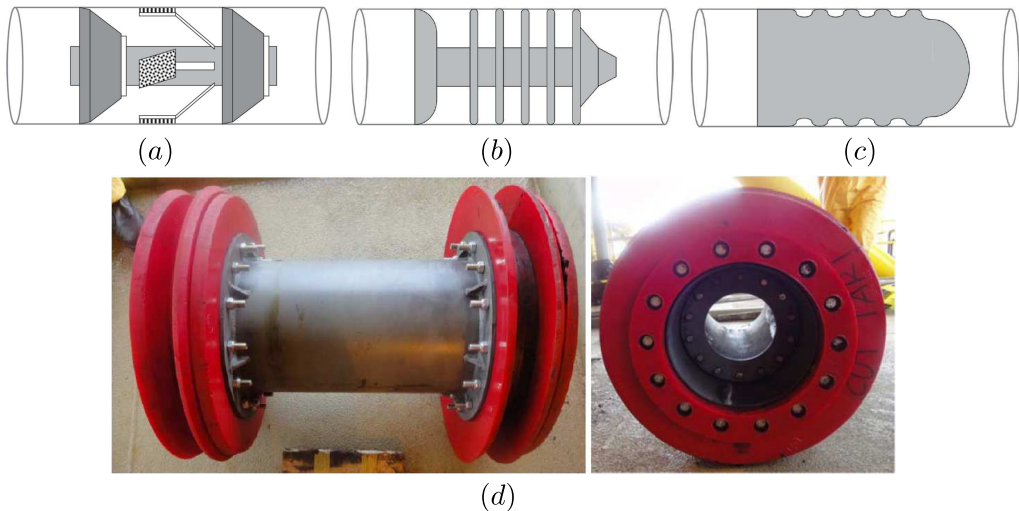


Figure 4.1: Several pig types: (a) Mandrel pig. (b) Solid cast pig. (c) Foam pig. (d) By-pass pig. Adapted from [74] and [53].

It is desirable that the product flow, which is driving the pigs through the pipeline, is interrupted as little as possible during the pigging operation. Conventional pigs, such as the

ones displayed in figure 4.1a-c, typically completely seal the pipeline. As a consequence the speed of the device will be equal to the velocity of the product flow. However, often a lower travel speed is desired, as a too high pig velocity may damage the pig or pipeline. In addition, it has been shown that a lower pig velocity is also beneficial for the cleaning and inspection performance of the pig [63, 96]. A solution to achieve a lower pig velocity while avoiding production deferment is the use of a by-pass pig, which does not seal the complete pipeline. Instead, a by-pass pig has a hole, or by-pass area, which allows fluid to by-pass the pig while it is moving inside the pipeline, see figure 4.1d. The presence of a by-pass will cause that the pig velocity is not dictated by the velocity of the product flow. Instead the pig velocity will be lower and it is now determined from a balance between the driving pressure force and the friction force between the pig and the pipe wall [82]. The risk, however, of using a by-pass pig is that the driving force on the pig becomes too low to overcome the wall friction force, which will result in a pig being stuck in the pipeline. To mitigate the risk of a stuck pig, so-called speed controlled pigs have been designed which have an adjustable by-pass area which provides the right amount of by-pass such that the velocity of the pig is lowered, while the pig does not get stuck [63]. Detailed mechanisms on how such a control system should be designed are only scarcely found in literature [62, 68].

In this study we consider the movement of a pig in a low pressure gas-filled pipeline. Piggings of such low pressure gas-filled pipelines in actual field operation can lead to large oscillations in the pig velocity due to the compressibility of the gas, see for example [67, 90]. This is because compressed gas pockets may build up at the upstream side of the pig when it is moving slower due to locally increased friction caused by for example irregularities in the inner pipe diameter. When the pressure in such a pocket has been sufficiently built-up, it is able to catapult the pig, resulting in large pig velocity excursions. This can lead to an unsafe and inefficient piggings operation. The effect described above gets more pronounced when the operating pressure or the flow velocity in the pipe is low. It can even result in a so-called ‘stick-slip motion’, where the pig slows down completely after a period of high velocity. This stick-slip motion of the pig is generally undesired in the industry. However, when a pig is equipped with appropriate speed control, the occurrence of high pig velocities in low pressure gas filled pipelines may be suppressed, which enables safe and effective piggings of these pipelines.

This chapter is built up as follows. In section 4.2 we first discuss the force balance on a (by-pass) pig. In addition we derive a simplified model which describes the motion of a pig in a low pressure system. The simplified model gives insights into the basic physical mechanisms which are key to unsteady pig motion due to low pressure conditions in gas filled pipelines. The simplified model relies on some assumptions, most notably the assumption that the pressure upstream of the pig is directly determined by the volume that the gas occupies upstream of the pig. In reality the pressure upstream of the pig will change as result of a transient pressure wave, rather than a instantaneous response to the change in volume. We therefore also include a more complete approach which models the motion

of the pig in a transient 1D pipe model. In section 4.3 we describe the experimental setup that has been used to perform pigging experiments. The experimental setup has been used in a previous work to test a prototype of a speed controlled pig [36, 44]. In this work we more systematically study the behaviour of by-pass pigs with constant by-pass area which, in combination with the developed models, is expected to improve the design of such a speed controlled pig. In section 4.4 a comparison will be made between the experimental results and the various models. The proposed models and experiments are subsequently used for the design of a PD controller in order to reduce pig velocity excursions through dynamically adjusting the size of the by-pass. Section 4.5 gives conclusions and discusses possibilities for future research.

4.2 MODELS

Whereas the pig velocity U_{pig} of a conventional pig in a pipeline is dictated by the bulk velocity U upstream of the pig, the pig velocity of a by-pass pig will be lower because part of the fluid is able to flow through the by-pass pig, see figure 4.2.

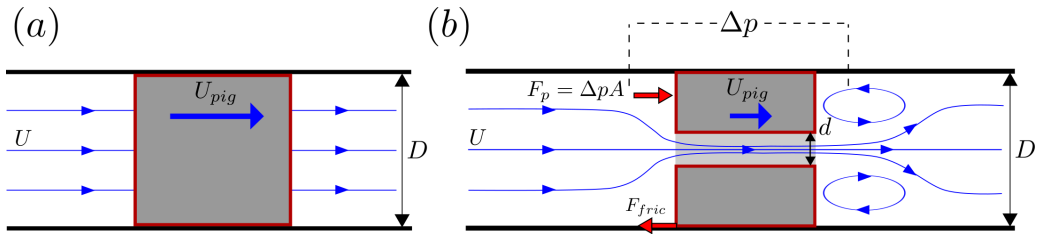


Figure 4.2: (a) Schematic motion of: (a) a conventional pig (b) a by-pass pig.

The motion of a by-pass pig in a horizontal pipeline is determined from a force balance between the driving pressure force F_p and frictional force F_{fric} . By applying a control volume analysis over the whole pig (including the by-pass area), F_p can be expressed as $F_p = \Delta p A$ where Δp is the pressure drop over the pig and A is the pipe cross-sectional area. The pressure drop is usually characterized by a pressure loss coefficient K defined as [45]:

$$K = \frac{\Delta p}{\frac{1}{2} \rho_{bp} U_{bp}^2}. \quad (4.1)$$

Here ρ_{bp} is the density of the fluid in the by-pass (which is taken as the density downstream of the pig) and U_{bp} is defined as the fluid velocity in the by-pass region taken relative to the pig velocity, see [35, 82]. A mass balance taking into account a higher den-

sity upstream of the pig ρ_{up} due to compressibility of the fluid thus yields the following expression for U_{bp} :

$$U_{bp} = \frac{D^2}{d^2} \frac{\rho_{up}}{\rho_{bp}} (U - U_{pig}). \quad (4.2)$$

Here D is the pipe diameter and d the diameter of the by-pass hole. Substituting this expression for U_{bp} into equation 4.1 and applying a steady state force balance on the pig ($\Delta pA = F_{fric}$) results in an equation for the velocity of the by-pass pig [30, 82]:

$$U_{pig} = U - \frac{d^2}{D^2} \frac{\rho_{bp}}{\rho_{up}} \sqrt{\frac{F_{fric}}{K \frac{1}{2} \rho_{bp} A}}. \quad (4.3)$$

When the by-pass area fraction d^2/D^2 goes to zero, equation 4.3 returns a pig velocity equal to the bulk velocity, as is the case for a conventional pig. When d^2/D^2 is not equal to zero, detailed knowledge of both K and F_{fric} are needed in order to accurately predict the pig velocity. The pig geometry in this research can be regarded as a thick orifice, for which the following correlation for the pressure loss coefficient has been proposed by Idelchik [45]:

$$K = 0.5 \left(1 - \frac{d^2}{D^2}\right)^{0.75} + \frac{4fL_{pig}}{d} + \left(1 - \frac{d^2}{D^2}\right)^2. \quad (4.4)$$

Here L_{pig} denotes the length of the pig, and f is the Fanning friction coefficient which has been calculated using the Churchill correlation [13]. Equation 4.4 can be recognized as a combination of the loss associated with a sudden compression (first term), frictional loss in the by-pass (second term), and a sudden expansion (third term). This correlation has been extensively verified with simulations using CFD (Computational Fluid Dynamics) [5, 82]. The loss coefficient for a by-pass pig that has a design different from a thick orifice geometry has been studied in [35]. Regarding the friction force F_{fric} , two main types of friction can be distinguished: (1) dry friction and (2) lubricated friction [72]. In case of lubricated friction (which obviously is only possible for twophase gas-liquid flow), a thin liquid layer is formed in between the two solids that is said to lubricate the relative motion. Such a lubrication layer normally reduces the friction coefficient considerably [84]. Our experiments are, however, carried out in a dry pipeline using air as working fluid. We model the dry sliding friction between the pig and the pipe wall with a constant coefficient. The proposed models of K and F_{fric} will be compared with experimental results which are described in section 4.3. With F_p and F_{fric} in place, the equation of motion of the pig follows as:

$$m \frac{d^2s}{dt^2} = F_p - F_{fric}. \quad (4.5)$$

Here m and s are the mass and the position of the pig, respectively.

We will now describe a simplified model and a more complete numerical model to describe the motion of a pig in a low pressure pipeline.

4.2.1 SIMPLIFIED MODEL

The simplified model considers the motion of the pig by modelling F_p as the force that results from the pressure in the gas pockets on both sides of the pig. It is assumed that the pressure in these pockets is uniform and adapts instantaneously to any changes in the volume that they occupy. The pressure upstream p_{up} of the pig thus reads

$$p_{up} = \frac{p^*}{\rho^*} \rho_{up} = \frac{p^*}{\rho^*} \frac{M_{tot}}{As} = \frac{p^*}{\rho^*} \frac{M_0 + \dot{M}t}{As}. \quad (4.6)$$

Here the ideal gas law is used to relate the pressure in the upstream pocket to the upstream density ρ_{up} , using $p^* = 101 \text{ kPa}$ and $\rho^* = 1.2 \text{ kg/m}^3$ as reference values for air. Furthermore, M_{tot} denotes the total mass in the upstream pocket, A is the pipe cross-sectional area, and s is the location of the pig as measured from the inlet. The total mass M_{tot} is a sum of the initial mass M_0 at $t = 0$ and the (constant) mass flux at the inlet \dot{M} multiplied by the time t .

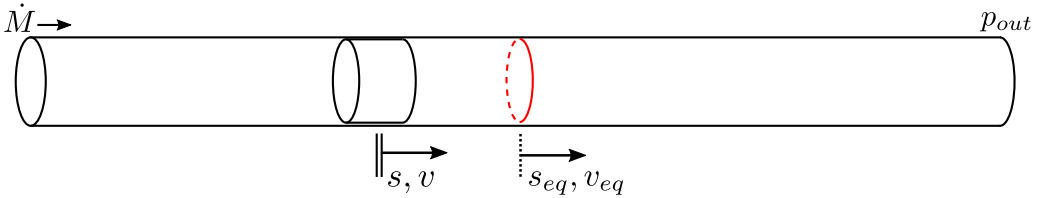


Figure 4.3: (a) Schematic motion of simplified pig model.

Applying the same approach to the downstream side of the pig leads to a constant pressure $p_{down} = p_{out}$ for the downstream gas pocket. This approach effectively neglects frictional pressure losses. Substituting $F_p = A(p_{up} - p_{down})$ into equation 4.5 yields:

$$m \frac{d^2s}{dt^2} = \frac{p^*}{\rho^*} \frac{M_0 + \dot{M}t}{s} - Ap_{out} - F_{fric}. \quad (4.7)$$

The equilibrium position $s(t) = s_{eq}(t)$ can be found by setting the left hand side of equation 4.7 equal to zero, which gives:

$$s_{eq}(t) = \frac{p^*}{\rho^*} \frac{M_0 + \dot{M}t}{Ap_{out} + F_{fric}}. \quad (4.8)$$

The equilibrium velocity v_{eq} can be found by differentiating equation 4.8, which yields:

$$v_{eq} = \frac{p^*}{\rho^*} \frac{\dot{M}}{Ap_{out} + F_{fric}}. \quad (4.9)$$

We now define $s(t) = s_{eq}(t) + \delta s(t)$. Dividing equation 4.7 by $Ap_{out} + F_{fric}$ and substituting the decomposition of s into equation 4.7 yields

$$\frac{m}{Ap_{out} + F_{fric}} \frac{d^2 \delta s}{dt^2} = \frac{s_{eq}(t)}{s_{eq}(t) + \delta s} - 1. \quad (4.10)$$

Assuming that the perturbations of δs are small ($\delta s \ll s_{eq}$) we can expand the first term on the right hand side of equation 4.10:

$$\frac{m}{Ap_{out} + F_{fric}} \frac{d^2 \delta s}{dt^2} = -\frac{\delta s}{s_{eq}(t)}. \quad (4.11)$$

Equation 4.11 can be solved analytically (see Appendix C), yielding an explicit expression for $\delta s(t)$:

$$\delta s(t) = C_1 k J_1(2k) - C_2 k Y_1(2k). \quad (4.12)$$

Here J_1 is the Bessel function of the first kind with order 1 and Y_1 is the Bessel function of the second kind with order 1. Furthermore $k(t)$ is given by:

$$k(t) = \omega(t) \left(\frac{M_0}{M} + t \right), \quad (4.13)$$

where $\omega(t)$ is given by:

$$\omega(t) = \sqrt{\frac{(Ap_{out} + F_{fric})}{s_{eq}(t) m}}. \quad (4.14)$$

Differentiating equation 4.12 yields an expression for the perturbed velocity δv (see Appendix C):

$$\delta v(t) = \omega^2(t) \left(\frac{M_0}{M} + t \right) (C_1 J_0(2k) - C_2 Y_0(2k)). \quad (4.15)$$

C_1 and C_2 are integration constants (with unit length) which can be found from the initial conditions for δs and δv . This approximate analytic expression will be compared with numerical integration of equation 4.7 in section 4.4.3.

4.2.1.1 Local analysis

When fixating the value for s_{eq} , Equation 4.11 can be recognized as the equation which describes a harmonic oscillator, for which the solution is given as:

$$\delta s(t) = C_3 \sin(\omega t + C_4). \quad (4.16)$$

Here ω is the local frequency of the solution for a given s_{eq} , as given by equation 4.14, and C_3 and C_4 are integration constants. The maximum value for δv_{max} can be found by differentiating Equation 4.16 and determining the maximum which gives:

$$\delta v_{max} = C_3 \omega. \quad (4.17)$$

The value of C_3 (and C_4) is determined by the initial conditions for $\delta s(t = 0)$ and $\delta v(t = 0)$, which we denote δs_0 and δv_0 respectively. C_3 can then be determined as:

$$C_3 = \frac{\sqrt{\omega^2 \delta s_0^2 + \delta v_0^2}}{\omega}. \quad (4.18)$$

Substituting this expression for C_3 into equation 4.17 gives:

$$\delta v_{max} = \sqrt{\omega^2 \delta s_0^2 + \delta v_0^2} = \sqrt{\frac{A p_{out} + F_{fric}}{s_{eq} m} \delta s_0^2 + \delta v_0^2}. \quad (4.19)$$

In order to determine δs_0 and δv_0 and s_{eq} we now consider a pig which moves in a stick-slip fashion and just enters the slip phase. In this analysis we introduce the static friction force $F_{fric,s}$, which is usually higher than the value of the sliding dynamic friction force F_{fric} . We now consider a pig that sticks at a location $L = s_{eq} + \delta s_0$. Just at the point before the pig starts slipping ($t = 0$) a force balance can be constructed which reads:

$$(p_{up} - p_{out})A = \left(\frac{p^* M_0}{\rho^* AL} - p_{out} \right) A = F_{fric,s} \quad (4.20)$$

This equation can be solved for M_0 and the result can be substituted into Equation 4.8 to yield an expression for the equilibrium position s_{eq} :

$$s_{eq} = \frac{L(F_{fric,s} + P_{out}A)}{F_{fric} + P_{out}A}. \quad (4.21)$$

Using $\delta s_0 = L - s_{eq}$ and $\delta v_0 = -v_{eq}$ and substituting these expressions into Equation 4.19 gives the following expression for the maximum velocity v_{max} which occurs during the stick-slip cycle:

$$v_{max} = v_{eq} + \delta v_{max} = v_{eq} + \sqrt{\frac{L(F_{fric,s} - F_{fric})^2}{m(F_{fric,s} + P_{out}A)}} + v_{eq}^2. \quad (4.22)$$

We note that if the static friction force $F_{fric,s}$ equals the dynamic friction force F_{fric} the maximum velocity is simply equal to twice the upstream equilibrium velocity v_{eq} .

4.2.2 FULL NUMERICAL MODEL

The full numerical model discretizes the fluid domain into multiple finite volumes, rather than describing the fluid upstream and downstream of the pig as one pocket as was done in the model described in section 4.2.1. The resulting model is a one-dimensional (1D) transient model, which solves for cross-sectionally averaged quantities such as pressure and velocity as function of the pipe coordinate s , which runs along the pipe, and time t . Examples of 1D transient tools which are used in the oil and gas industry to model pig motion in a pipeline include OLGa and LedaFlow [8, 28]. The current 1D model relies on the 1D extended Euler equations from which the cross-sectionally averaged mass and momentum equation read:

$$\frac{\partial}{\partial t} (\rho A) + \frac{\partial}{\partial s} (\rho u A) = 0, \quad (4.23)$$

$$\frac{\partial}{\partial t} (\rho u A) + \frac{\partial}{\partial s} (\rho u^2 A + p A) = -\tau (\pi D). \quad (4.24)$$

Here τ is the wall shear stress which is calculated as:

$$\tau = \frac{1}{2} \rho u^2 f, \quad (4.25)$$

where f is the Fanning friction coefficient calculated using the Churchill relation [13]. As in the simplified model, we calculate $\rho = \rho(p)$ through the ideal gas law, that is $\rho = (\rho^*/p^*)p$. Equations 4.23 and 4.24 form a closed system of equations which is discretized using the finite volume method on a staggered grid, see figure 4.4.

Conservation of mass (equation 4.23) is discretized on the p -volume Ω_p , in which p is defined at the center of the volume:

$$\frac{d}{dt} (\rho_i \Omega_i^p) + \rho_{i+1/2} u_{i+1/2} A - \rho_{i-1/2} u_{i-1/2} A = 0 \quad (4.26)$$

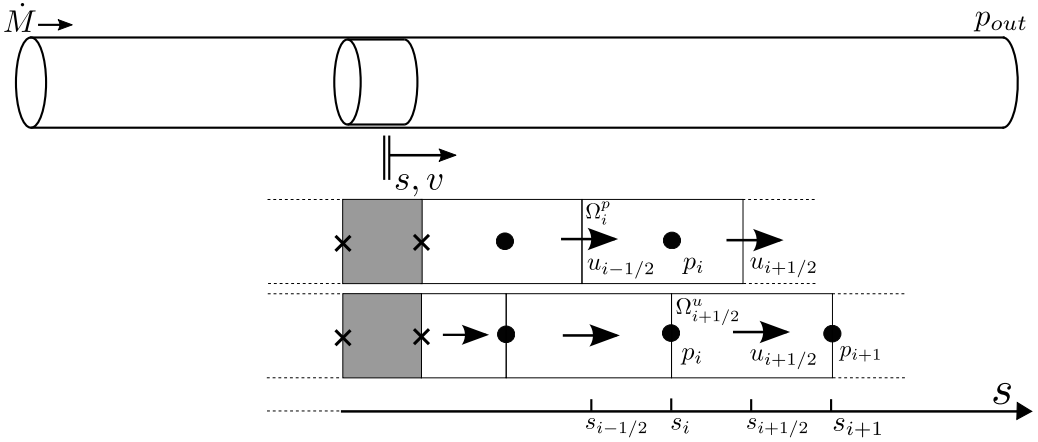


Figure 4.4: Staggered grid layout in the full numerical model.

Here $\Omega_i^p = A\Delta s_i = A(s_{i+1/2} - s_{i-1/2})$ is the size of the finite p-volume. Conservation of momentum (equation 4.24) is discretized in a similar way:

$$\frac{d}{dt} \left(\rho_{i+1/2} u_{i+1/2} \Omega_{i+1/2}^u \right) + \rho_{i+1} (u_{i+1})^2 A - \rho_i (u_i)^2 A = -\tau_{i+1/2} (\pi D) \Delta s_{i+1/2} \quad (4.27)$$

Here $\Omega_{i+1/2}^u = A\Delta s_{i+1/2} = A(s_{i+1} - s_i)$ is the size of the finite u-volume. Some terms in equation 4.26 and 4.27 require interpolation. If the term is part of a convective term a flux limiter is used, otherwise central interpolation is used. The system is integrated in time using the second order BDF2 scheme. For more details on the numerical implementation, the reader is referred to chapter 6.

4.3 EXPERIMENTAL SETUP

A schematic of the flow loop in which the laboratory experiments are conducted is depicted in figure 4.5a. The loop consists of a horizontal transparent perspex pipe with a length of 62 meter and an internal diameter of 52 millimeter. The experiment is operated in single phase using air as working fluid. The flow loop is equipped with a pig launcher located at the inlet of the loop that allows to insert a pig into the system, see figure 4.5b. By placing the pig in the launcher and subsequently redirecting the air through the launcher the pig will be inserted into the pipe. After traversing along the pipe the pig is trapped at the outlet and can be retrieved. Figure 4.5c shows a close-up of one of the pigs that is used in the experiments.

The air that is used as working fluid in the experiment is tapped from an air supply system which is kept at a pressure of 8 bar. A pressure reducing valve brings this down to

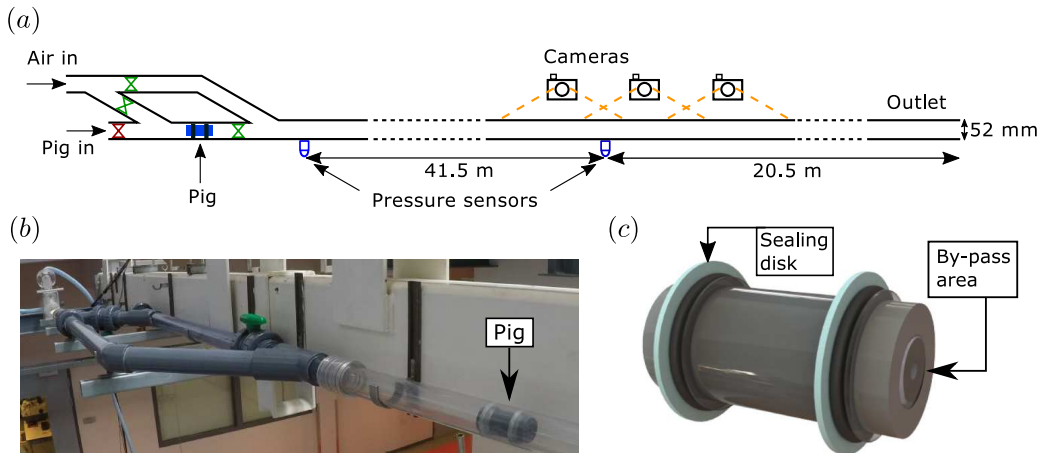


Figure 4.5: (a) Overview of the flow loop. (b) Close-up of the pig launcher. (c) Drawing of the pig.

2 bar. The air then passes through a gas flow meter (Bronkhorst - MASS-STREAM Series D-6300) where the air mass flux can be controlled. The flow loop is equipped with two pressure sensors (Validyne DP15), see figure 4.5a. The average pig velocity is computed as the total length divided by the residence time. For the length, the distance between the upstream pressure transducer and the pig receiver (i.e. the flow loop exit) is used, which amounts a distance of 62 m. The residence time is the time difference found by studying the pressure increase and decrease measured by the upstream pressure transducer. In addition, the pressure drop that is measured over the pig allows to determine the frictional force of the pig with the pipe wall, since in steady state the driving pressure force and the frictional force must balance, see equation 4.5. Three synchronized high speed cameras (GoPro HERO4) located at about 41.5 meter downstream of the first pressure sensor allow for the local dynamics of the pig to be analyzed, see figure 4.5a. The cameras are operated at a framerate of 120 frames per second at a resolution of 720p. The cameras are separated in such a way that their field of views partly overlap. The three images of each camera are stitched together during post-processing using a cross-correlation algorithm in order to construct one single image. The total field of view thus obtained is 7.5 meter. The cameras are synchronized in time by using a flash light as reference point which is visible on all three cameras at the beginning of a measurement.

The pigs are custom-made and have a flexible modular design which allows for the by-pass area and sealing disks to be easily interchanged. The sealing disk makes sure that no fluid leaks between the pig and the pipe wall, and that the only fluid that flows through the pig goes through the by-pass area, see figure 4.5c. The by-pass area is formed by a concentric hole in the centre of the pig body and ranges from 0% to 4% of the total cross-sectional area in the current experiment.

Two pig configurations have been tested: configuration 1 and configuration 2, see figure 4.6a and figure 4.6b respectively. Both configurations have a sealing disk with a slightly larger diameter than the inner pipe diameter. The difference in the diameters, or the oversize, ensures that the pig properly seals the pipeline and that no leakage occurs between the pig and the pipe wall [74].

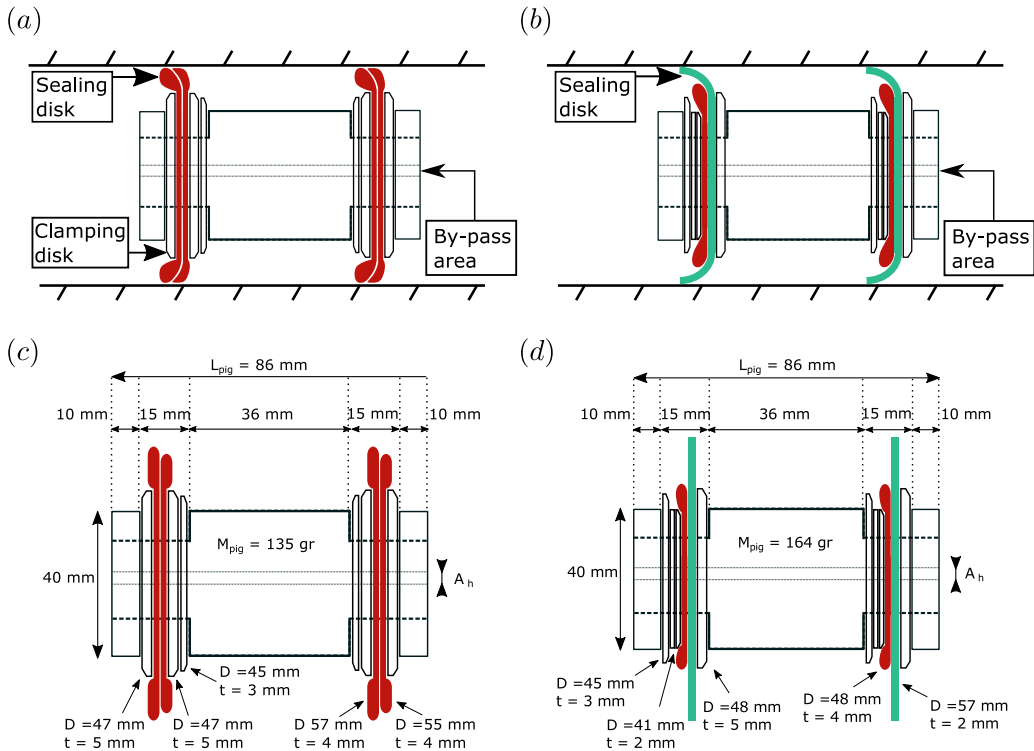


Figure 4.6: (a) Schematic of pig configuration 1. (b) Schematic of pig configuration 2. (c) Detailed geometry of pig configuration 1. (d) Detailed geometry of pig configuration 2.

The two pig configurations have a different sealing disk compression behaviour. The seals in configuration 1 are compressed in the radial direction. For industrial pigs, sealing disks deformed in a similar way are referred to as scraper disks [74]. Since the used material of our small-scale pigs is rather flexible, the variation in friction due to diameter variations is limited. Furthermore, the clamping disks can be relatively large which prevents tilting of the pig. A downside of the flexible seals is that severe wear of the sealing disks can occur. In the current experiment they were therefore replaced after roughly every 6 runs. The seals in configuration 2 have more space to bend compared to configuration 1. This is comparable with what in industry is referred to as cone disks [74]. The sealing disk material of configuration 2 is much harder and shows very good wear properties. A downside is that more space is required for the seals to bend, which increases the chance

that the pig is being tilted. The dimensions of pig configurations 1 and 2 are displayed in figure 4.6c and in figure 4.6d, respectively. More details on the material and sizes of the sealing disks are listed in table 4.1. To build up sufficient pressure, it is essential that the pig properly seals the pipe. Cell rubber (EPDM) with a closed cell structure is chosen for configuration 1 to guarantee that the sealing disk is impermeable. Para rubber is used for configuration 2, which has very good wear properties.

Table 4.1: Properties of pig configurations.

Property	Configuration 1	Configuration 2	Unit
Material sealing disk 1	EPDM	Para rubber	-
Hardness sealing disk 1	35 *	45	Shore A
Outer diameter sealing disk 1	57	57	mm
Thickness sealing disk 1	4	2	mm
Material sealing disk 2	EPDM	EPDM	-
Hardness sealing disk 2	35	35	Shore
Outer diameter sealing disk 2	55	48	mm
Thickness sealing disk 2	4	4	mm
Average friction	25.68	41.3	N

* The hardness is measured according Shore 00 standards. A comparable Shore A value is given here to compare with the other material

From the pressure measurements during the pigging runs an estimation of the friction was obtained for both configurations, see table 4.2. This table will be explained in more detail in the next section.

4.4 RESULTS

This section starts with some overall results from the various pigging runs that have been conducted in the lab facility. In total 72 runs were used in the analysis of configuration 1, and 60 runs were performed with configuration 2. The overall quantities include the average pig velocity and the required driving pressure for various by-pass pigs. These results are important for verifying steady state by-pass pigging models which can be used to predict the pig velocity. In addition, the results are relevant for 1D transient models in which the trajectory of the pig can be monitored [8, 28]. These 1D transient models rely on accurate correlations to model the pig dynamics. Subsequently, section 4.4.2 presents an analysis of the local pig dynamics which gives insight in the oscillatory behaviour of the pig motion due to the low pressure conditions. A comparison with the models developed

in section 4.2 will be made. The results for the local behaviour of the pig motion are used in section 4.4.3 to design a simple PD controller to reduce the velocity excursions of the pig by dynamically adjusting the by-pass area.

4.4.1 OVERALL BEHAVIOUR

For each pigging run the pressure from the upstream and downstream pressure sensors is recorded. Figure 4.7a shows a typical signal that is obtained. Here the mass inflow rate is $\dot{M} = 0.0089$ kg/s, and the pig has configuration 2 with 0% by-pass. When the pig traverses along the upstream pressure sensor the excess pressure increases to about 20 kPa. After traversing 41.5 meter the pig reaches the downstream pressure sensor, which is clearly visible by the uptake of the signal at around 16 seconds. When the pig reaches the outlet of the pipe both signals drop because the pressure that was built up behind the pig is now released.

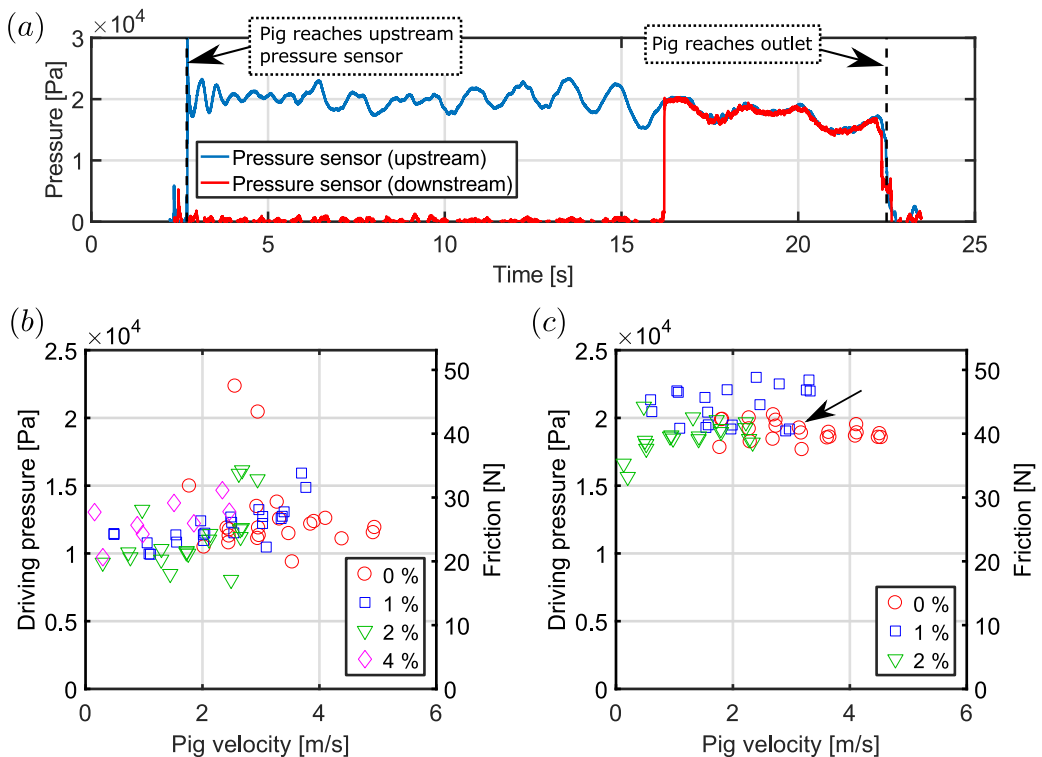


Figure 4.7: (a) Pressure signal for configuration 2 with 0% by-pass. (b) Average driving pressures for the configuration 1 pigging runs. (c) Average driving pressures for the configuration 2 pigging runs. The symbols in (b) and (c) denote various by-pass ratios.

From the time difference between the instant that the pig reaches the upstream pressure sensor and the outlet, the average pig velocity can be obtained. In addition, the average driving pressure force needed to propel the pig can be deduced from the measurements, which in steady state balances the friction force between the pig and the pipe wall. Figure 4.7b and 4.7c show the average driving pressures ($\bar{p}_{\text{up}} - \bar{p}_{\text{down}}$) as function of the pig velocity for configuration 1 and for configuration 2, respectively. The measurement corresponding to the pressure signal displayed in figure 4.7a is indicated by the black arrow in figure 4.7c. The different pig velocities have been obtained by varying both the upstream bulk velocity of the air as well as the by-pass area, as will be explained in more detail below. When inspecting figures 4.7b and 4.7c, we note that the driving pressure is not a function of the pig velocity. This substantiates our earlier modeling assumption that the friction of the pig can indeed be approximated by a constant (dry) friction force within the current parameter range. It is important to note that this can be different when the transported fluid is a liquid instead of a gas or when there is two-phase gas-liquid flow, due to the effect of possible lubrication. From the data presented in figure 4.7 the overall average friction force for each by-pass pig (0,1,2, and 4%) for the two configurations can be obtained. These average friction values, with the standard deviation, are summarized in table 4.2. As can be noted from both figure 4.7 and table 4.2 no runs for a by-pass of 4% were performed for configuration 2. The reason is that the friction of this pig with 4% by-pass is too high which results in a stalled pig.

Table 4.2: Properties of pig configurations.

	By-pass area ratio(%)			
	0	1	2	4
Configuration 1				
Average friction (N)	27.1 ± 6.5	25.5 ± 3.0	23.9 ± 5.0	26.5 ± 4.5
Configuration 2				
Average friction (N)	40.3 ± 1.5	44.4 ± 2.9	39.5 ± 2.5	NA

One of the main reasons for using by-pass pigs is the ability to reduce the pig velocity. The flow velocity can be kept at the nominal production rate whereas the pig travels through the pipeline at a lower velocity. The reduction in the pig velocity depends on the by-pass ratio, see equation 4.3. Figure 4.8 shows the pig velocity versus the flow velocity for both configurations 1 and 2. Different colours and symbols are used for different by-pass area ratios.

The red circles represent the pigging runs with zero by-pass. These pig velocities should be equal to the upstream bulk velocity, which is indicated by the 45 degree line in gray. The results for both configurations indeed follow this line. The other markers represent the pig velocity for a specific by-pass ratio. As can be noted an increase in by-pass area

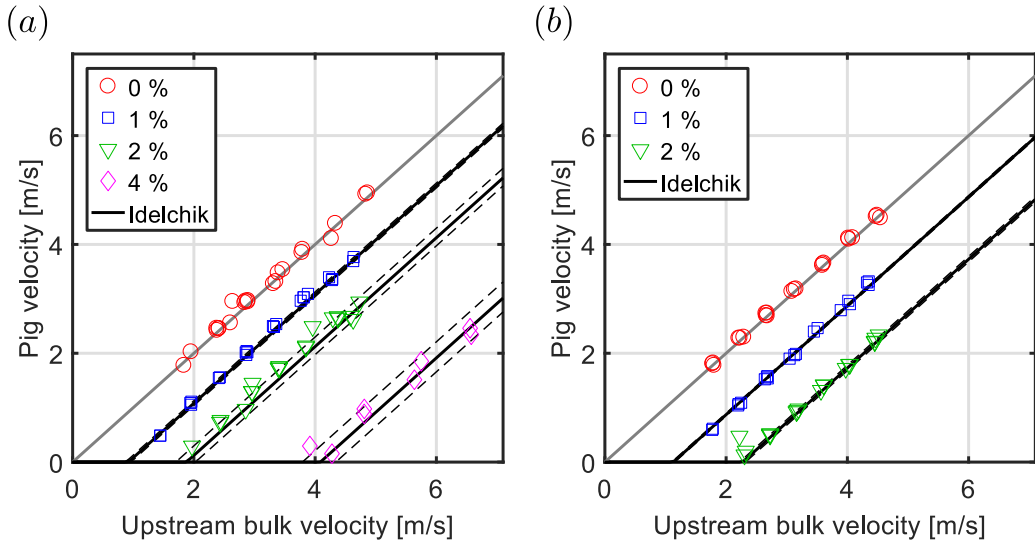


Figure 4.8: Pig velocity as function of upstream bulk velocity (a) Configuration 1, (b) Configuration 2. The dashed lines denote the standard deviation in the calculated pig velocity.

does indeed result in a reduction of the pig velocity. It can be deduced from figure 4.8 that the reduction in pig velocity is around 1 m/s for each percentage of by-pass area that is added relative to the zero by-pass case. For a more quantitative comparison with theory we compare the experimental results with the velocity predicted by equation 4.3, which is shown by the black line. In this equation the friction force F_{fric} is taken equal to the average measured value of the friction, see table 4.2. The value for K in equation 4.3 is modeled by the Idelchik relation (equation 4.4) to model the pressure drop. Therefore the solid line effectively plots the predicted travel velocity based on the Idelchik relation and a constant predetermined friction. In addition the velocity calculated based on plus and minus the standard deviation of the friction force are included as black dashed lines. As was already shown in table 4.2, the spread is higher for configuration 1. Figure 4.8 shows very good agreement between the measurements and the values based on the Idelchik relation. During the pigging runs oscillatory motion of the pig was observed, which will be discussed in the next section. These results show that even though equation 4.3 is based on a steady state balance it can be applied to unsteady pig motion from which an average pig velocity is extracted.

We further note that the point where the black line intersects the horizontal axis indicates a minimum average bulk velocity which is needed to propel the by-pass pig. Below this bulk velocity not enough driving pressure is generated to overcome the average friction force of the pig with the pipe wall. Note that in practice the minimum required bulk velocity may be higher as the black line is based on an average friction. A local increase in friction, for example due to irregularities in the pipe diameter, may cause a pig to stall

even above this velocity. In the next section we will discuss the local behaviour which is observed by analyzing detailed dynamics of the pig motion as well as time series of the upstream pressure.

4.4.2 LOCAL BEHAVIOUR

We now focus on the local behaviour of the pig motion. As was mentioned in the previous section stick-slip motion was observed in the experiment. The oscillatory signal of the pressure (figure 4.7a) indicates that the pressure upstream of the pig is indeed not constant as would be expected in case the pig would move at a constant steady state velocity. Figure 4.9 shows the upstream pressure signal which is displayed in figure 4.7a together with a prediction from the simplified model, as described in section 4.2.1. The model is initiated at two time instances: $t_1 = 3.04$ and $t_2 = 12.20$ seconds. These instances are selected as case examples in the time series of the upstream pressure, as a clear oscillatory signal is visible, see figure 4.9. In order to evaluate the simplified model to predict the upstream pressure, equation 4.6 is used. To evaluate equation 4.6 the initial position of the pig needs to be known. Clearly, the pig is located further downstream at $t = t_2$ than at $t = t_1$. To determine the initial pig positions for these two cases, the equilibrium velocity (Equation 4.9) is multiplied by the traveling time t_1 and t_2 . Furthermore, the dynamic friction force F_{fric} and the static friction force $F_{fric,s}$ are input parameters to the model. F_{fric} has been estimated by determining the mean driving pressure which is needed to propel the pig multiplied by the pipe area, as has been described in 4.4.1. $F_{fric,s}$ is estimated at 1.5 times the standard deviation of the pressure signal of the upstream pressure sensor multiplied by the pipe area. This leads to $F_{fric} = 40.80$ N and $F_{fric,s} = 43.87$ N. The pressure values which are needed to balance the friction forces F_{fric} and $F_{fric,s}$ are indicated with a dashed and a dotted line respectively, see figure 4.9.

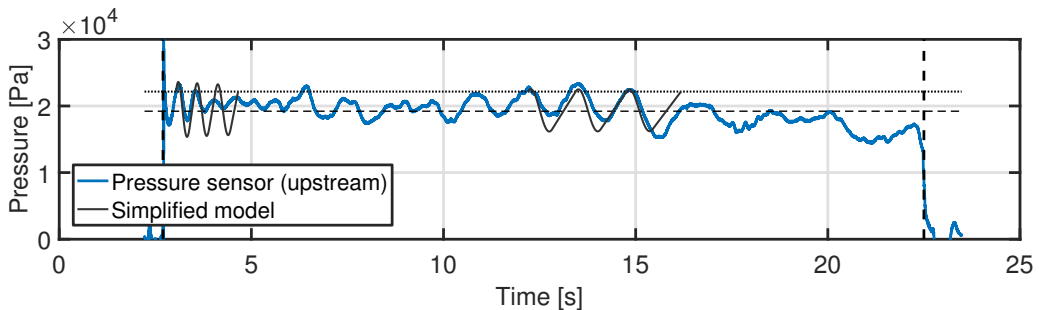


Figure 4.9: Pressure signal for configuration 2 with 0% by-pass compared with the simplified model. The horizontal dashed lines represent the average pressure plus and minus 1.5 times the standard deviation of the pressure multiplied by the pipe area.

Figure 4.9 shows qualitatively good agreement between the measured upstream pressure and the value obtained with the simplified model. Both the model and the measurements show that the frequency of the oscillation decreases when the pig moves further through the pipeline. This is in line with equation 4.14, which describes the local frequency of the oscillation. It must be noted that the simplified model idealizes the model of the friction in the sense that it assumes one value of the static friction $F_{fric,s}$ and one value of the dynamic friction F_{fric} . In reality the value of $F_{fric,s}$ may vary due to for example irregularities in the inner pipe diameter. Nonetheless it can be observed that the frequency of oscillations of the pig motion can be captured by the model by estimating constant values for F_{fric} and $F_{fric,s}$.

The oscillation in pressure which was discussed above is directly connected to oscillations in the pig velocity. We now use the images from the high speed cameras, which are located around 41.5 meter downstream of the upstream pressure sensor (see figure 4.5), to investigate the maximum pig velocity that occurs. The maximum velocity is found from the video recordings by tracking the location of the pig using image processing, as discussed in section 4.3. The experiments performed with configuration 2 are selected, because the spread in average friction is smaller compared to configuration 1, see section 4.4.1. The results are shown in figure 4.10a. The coloured symbols represent the different by-pass pigs that are used in the experiment. In addition the maximum velocity as predicted by the simplified model, equation 4.22, is shown. Here the dynamic friction F_{fric} is taken equal to the value of the 0% by-pass pig, which is 40.3 N, see table 4.2. The static friction $F_{fric,s}$ is taken equal to 40.3 N, 44 N, and 48 N, as shown by the solid, dashed, and dotted line, respectively. It is clear from figure 4.10a that a higher value of $F_{fric,s}$ promotes a higher maximum pig velocity. This is explained by the higher pressure in the gas pocket upstream of the pig corresponding to the higher value of the static friction force $F_{fric,s}$. The black solid line represents the maximum pig velocity in case $F_{fric,s}$ is equal to F_{fric} . According to equation 4.22 this corresponds to a maximum pig velocity which is twice the average pig velocity. From the measurements it is clear that the maximum pig velocity is indeed significantly higher than the average travel velocity of the pig as most of the measurements are located at the left of the solid line. In addition to the measurements and the simplified model, the results of the full numerical model as explained in section 4.2.2 are included for the three different values of $F_{fric,s}$ (lines with solid black circles). The by-pass in this simulation is set equal to 0%. The maximum pig velocity has been obtained from a simulation in which the pig is inserted 40 meter downstream. This location ensures that the maximum velocity occurs within the location corresponding to the field of view of the cameras in the experiment. Grid converged solutions were typically obtained when using a total of 200 finite volumes, which corresponds to a computational cell length of about 0.34 meter, and a timestep of 0.0025 seconds.

When comparing the results of the simplified model with the full numerical model and the experimental data we note that the simplified model overpredicts the maximum velocity. This is due to the assumption in the simplified model that the influence of pressure

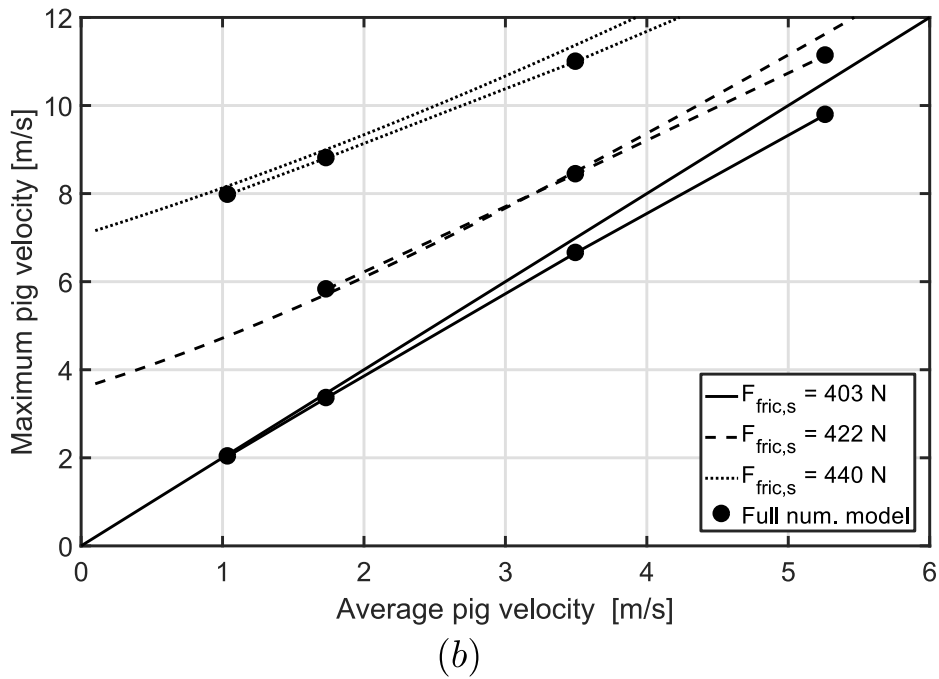
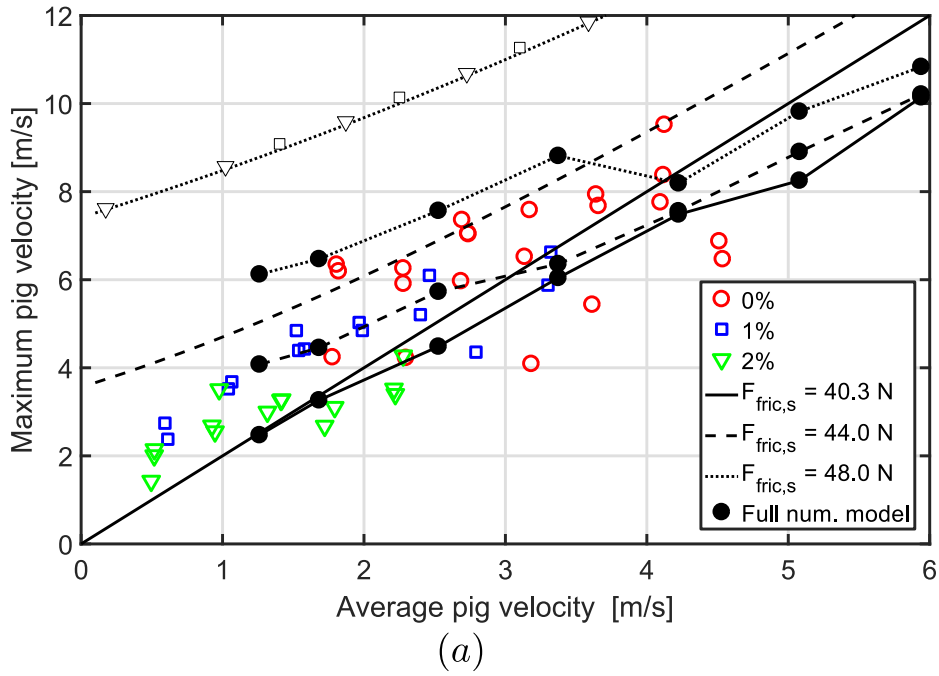


Figure 4.10: Maximum pig velocity versus average pig velocity: (a) Experimental conditions (b) Higher friction (10 times) compared to experimental conditions.

waves due to the acceleration of the fluid around the pig are negligible. The full numerical model does incorporate this, and therefore predicts a lower maximum velocity within this parameter range. The effect of these pressure waves compared to the overall pressure drop over the pig becomes less important if the friction force of the pig is larger. To test this hypothesis we run the same simulation, but now increase the value of F_{fric} by a factor 10 to $F_{\text{fric}} = 403$ N. Again three values of $F_{\text{fric},s}$ have been chosen as 403 N, 422 N, and 440 N. We also increased the pig mass by a factor 10. We now see that the agreement between the simplified model and the full numerical model is much closer. Therefore we conclude that the simplified model can be used to estimate the maximum velocity if the magnitude of the pressure waves that occur in the fluid due to the acceleration of the pig are negligible compared to the pressure drop over the pig.

Figure 4.10a shows the simplified model (lines) and the full numerical model (lines with solid black circles) evaluated for the 0% by-pass case. The experimental results performed with the 1% and 2% by-pass pigs are superimposed in the plot. Although the travel velocity of the by-pass pigs is lower, it can be noted that the results with 1% and 2% by-pass follow the trend of the results with 0% by-pass and thus have a significantly higher maximum velocity than the average travel velocity. We also have evaluated the simplified model by incorporating a by-pass. To make the simplified model suitable for by-pass pigs, equation 4.7 is modified to take into account the mass leakage that occurs through the by-pass:

$$m \frac{d^2s}{dt^2} = \frac{p^*}{\rho^*} \frac{M_0 + \dot{M}t - \int \dot{M}_\beta dt}{s} - Ap_{\text{out}} - F_{\text{fric}}, \quad (4.28)$$

where \dot{M}_β is the mass flux through the by-pass given by

$$\dot{M}_\beta = (U - U_{\text{pig}})A\rho_{\text{up}}. \quad (4.29)$$

Here U can be solved from equation 4.3 for a given mean pig velocity U_{pig} . Instead of constructing an analytical solution, which was possible for 0% by-pass case, equation 4.28 is solved numerically. As an example the results for $F_{\text{fric},s} = 48$ N are included in figure 4.10a with white squares and white triangles for 1% and 2% by-pass respectively. These symbols closely follow the line of the simplified model corresponding to 0% by-pass. It can thus be concluded that a fixed by-pass area does not reduce the velocity excursion of the pig. This is also confirmed by the experimental results as shown in figure 4.10: although the average speed of the by-pass pigs is lower, the maximum velocity is still significantly higher than the average pig velocity. However when the by-pass area is not fixed, but instead is adjusted dynamically, the maximum pig velocity can be reduced, which will be discussed in the next section.

4.4.3 CONTROL

In the previous sections the mechanism behind oscillatory motion of a pig in a low pressure pipeline has been explained and described. Due to stick-slip behaviour it was found that the maximum pig velocity is significantly higher than the average pig velocity for both conventional pigs (i.e. no by-pass) as well as pigs with by-pass. We now propose a control mechanism which relies on actively regulating the size of the by-pass, such that part of the pressure in the gas pocket upstream of the pig can be released. This would result in a lower maximum pig velocity, as the driving upstream pressure is reduced during the acceleration of the pig. It is important to note that if the by-pass stays open too short or too little, not enough pressure is released and the pig still accelerates to a high velocity. On the other hand, if the by-pass stays open too long, too much pressure is released and instead of mitigating the spike in pig velocity, a new stick-slip cycle is promoted. The ideal by-pass opening can be determined by an appropriate control algorithm. The time scale on which the controller should act is given by $2\pi/\omega$, where ω is the local angular frequency of the oscillation, given by equation 4.14. We will now demonstrate a simple controller based on the physical models that have been formulated, which set some minimum requirements for the design of a controller. Therefore we again consider a pig that sticks at location L at $t = 0$. When defining $\tilde{s} = s - L$ and $\tilde{v} = d\tilde{s}/dt$ we can write equation 4.28 as:

$$m \frac{d^2\tilde{s}}{dt^2} = \frac{p^*}{\rho^*} \frac{M_0 + M_u}{\tilde{s} + L} - Ap_{out} - F_{fric}. \quad (4.30)$$

Here $M_u = \int_0^t (\dot{M} - \dot{M}_\beta) dt$ is the upstream mass that has been added after the pig starts moving. We can put equation 4.30 in state space form by selecting M_u as control variable and linearizing around the point $\tilde{s} = 0, \tilde{v} = 0, M_u = 0$:

$$\begin{bmatrix} \dot{\tilde{s}} \\ \dot{\tilde{v}} \end{bmatrix} = \begin{bmatrix} 0 & 1 \\ -\frac{p^* M_0}{\rho^* L^2 m} & 0 \end{bmatrix} \begin{bmatrix} \tilde{s} \\ \tilde{v} \end{bmatrix} + \begin{bmatrix} 0 \\ \frac{p^*}{\rho^* L m} \end{bmatrix} M_u = \begin{bmatrix} 0 & 1 \\ -\omega^2 & 0 \end{bmatrix} \begin{bmatrix} \tilde{s} \\ \tilde{v} \end{bmatrix} + \begin{bmatrix} 0 \\ \frac{v_{eq} \omega^2}{M} \end{bmatrix} M_u \quad (4.31)$$

$$v = \begin{bmatrix} 0 & 1 \end{bmatrix} \begin{bmatrix} \tilde{s} \\ \tilde{v} \end{bmatrix}. \quad (4.32)$$

In the final step in obtaining equation 4.31 above we assumed for simplicity, without loss of generality, that $F_{fric,s} = F_{fric}$. The corresponding transfer function $P(\sigma)$ of the state space model reads:

$$P(\sigma) = \frac{\sigma \frac{v_{eq} \omega^2}{M}}{\sigma^2 + \omega^2}. \quad (4.33)$$

Here σ denotes the complex frequency variable. A feedback loop with a linear controller $C(\sigma)$ may be constructed as shown in figure 4.11a.

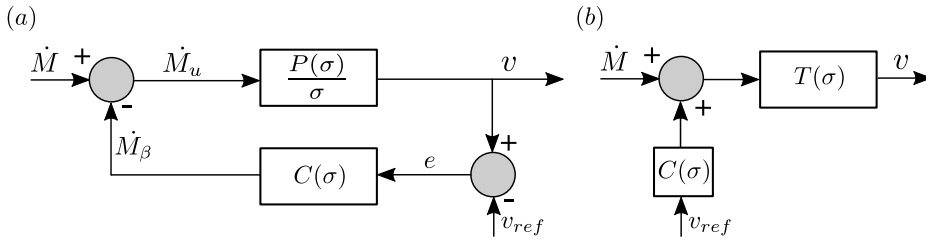


Figure 4.11: (a) Feedback loop (b) Equivalent feedback loop with closed loop transfer function $T(\sigma)$.

The goal is to have no excursion in the pig velocity, and preferably it is equal or close to a preset reference velocity v_{ref} . Perhaps the simplest controller which would meet these requirements is a PD-controller:

$$C(\sigma) = K_p + K_d \sigma \quad (4.34)$$

The closed loop transfer function T as displayed in the equivalent blockdiagram in figure 4.11b then follows as:

$$T(\sigma) = \frac{\frac{v_{eq} \omega^2}{\dot{M}}}{\sigma^2 + \omega^2 + \frac{v_{eq} \omega^2}{\dot{M}} (K_p + K_d \sigma)} \quad (4.35)$$

We now again consider the example case which has been discussed in section 4.4.2. For this case we have $\dot{M} = 0.0089$ kg/s and $F_{fric} = 40.80$ N. This yields a value of $v_{eq} = 2.94$ m/s and $\omega = 6.21$ rad/s, see equation 4.9 and equation 4.14 respectively. The open loop response of the linear system to a mass influx \dot{M} at $t = 0$ is marginally stable and is shown by the black line in figure 4.12a. Indeed when performing the numerical integration of equation 4.30 the pig velocity shows persisting oscillations, as shown by the red squares in figure 4.12a. We note that these numerical results for the 0% by-pass case are well captured by using the analytical approximation of equation 4.15, as shown by the red solid line. We now focus on damping the oscillation. The damping ratio of the second order system (equation 4.35) can be identified as:

$$\zeta = \frac{\frac{v_{eq} \omega^2}{\dot{M}} K_d}{2 \sqrt{\omega^2 + \frac{v_{eq} \omega^2}{\dot{M}} K_p}} \quad (4.36)$$

Furthermore, we note that a constraint on the controller is that \dot{M}_β has a maximum equal to \dot{M} . The typical error in the velocity \tilde{e} can be estimated as $-v_{eq}$, which is equal to the error in the beginning of a slip phase, as the actual pig velocity is still zero at that point. In a similar fashion, we estimate $d\tilde{e}/dt$ as $2v_{eq}\omega/\pi$, which is the average acceleration from 0 to $2v_{eq}$ in the time period π/ω . Using these estimations of \tilde{e} and $d\tilde{e}/dt$ the following requirement can then be formulated:

$$K_p \tilde{e} + K_d \frac{d\tilde{e}}{dt} = -K_p v_{eq} + K_d \frac{2v_{eq}}{\pi\omega} = \dot{M}. \quad (4.37)$$

K_p and K_d can now be solved from equation 4.36 and equation 4.37 and expressed as:

$$K_p = \frac{\dot{M}(16\zeta^2 - \pi^2)}{v_{eq}\pi^2} \text{ kg/m} \quad (4.38)$$

$$K_d = \frac{\dot{M}8\zeta^2}{v_{eq}\omega\pi} \text{ kg s/m}. \quad (4.39)$$

Oscillations will be damped when $\zeta > 1$. We choose a value of $\zeta = 1.2$, which yields $K_p = 0.0041 \text{ kg/m}$ and $K_d = 0.0018 \text{ kg s/m}$. The result of this closed loop system is shown in figure 4.12c/d. The linear response of the closed loop system (black solid line), as well as numerical integration (red squares) indeed show that the pig velocity does not overshoot but now approaches the reference velocity (dashed black line), which has been set just below v_{eq} at a value equal to 2.75 m/s. In order to obtain this pig velocity trajectory, M_β and the corresponding by-pass opening have been increased for a short time period to release the excess pressure of the upstream gas pocket. This is shown by the black triangles in figure 4.12d and the blue triangles in figure 4.12c respectively.

The simplified model relies on various assumptions, most notably the assumption that the pressure in the gas pocket upstream and downstream of the pig is instantaneously determined by the volume that the gas pocket occupies. The 1D full numerical model as described in section 4.2.2, however, contains more physics and does not rely on this assumption. We now apply the controller derived from the simplified model directly on the full numerical model. The result is shown by the black circles in figure 4.12c. Although some oscillations are still present, the maximum pig velocity also in this case is clearly diminished. In very long pipelines the assumption of an instantaneous pressure response in the simplified model will not hold. It is therefore recommended for future research to further investigate the applicability of the simplified model in long pipelines. Instead of selecting the upstream mass M_u as a control parameter, a local pressure analysis around the pig may be more appropriate in this case.

The above example illustrates some minimum requirements on a controller which can be used to reduce pig velocity excursions in low pressure pipelines. In order to realize this in practice, the pig needs to be able to track at least the following quantities: pig

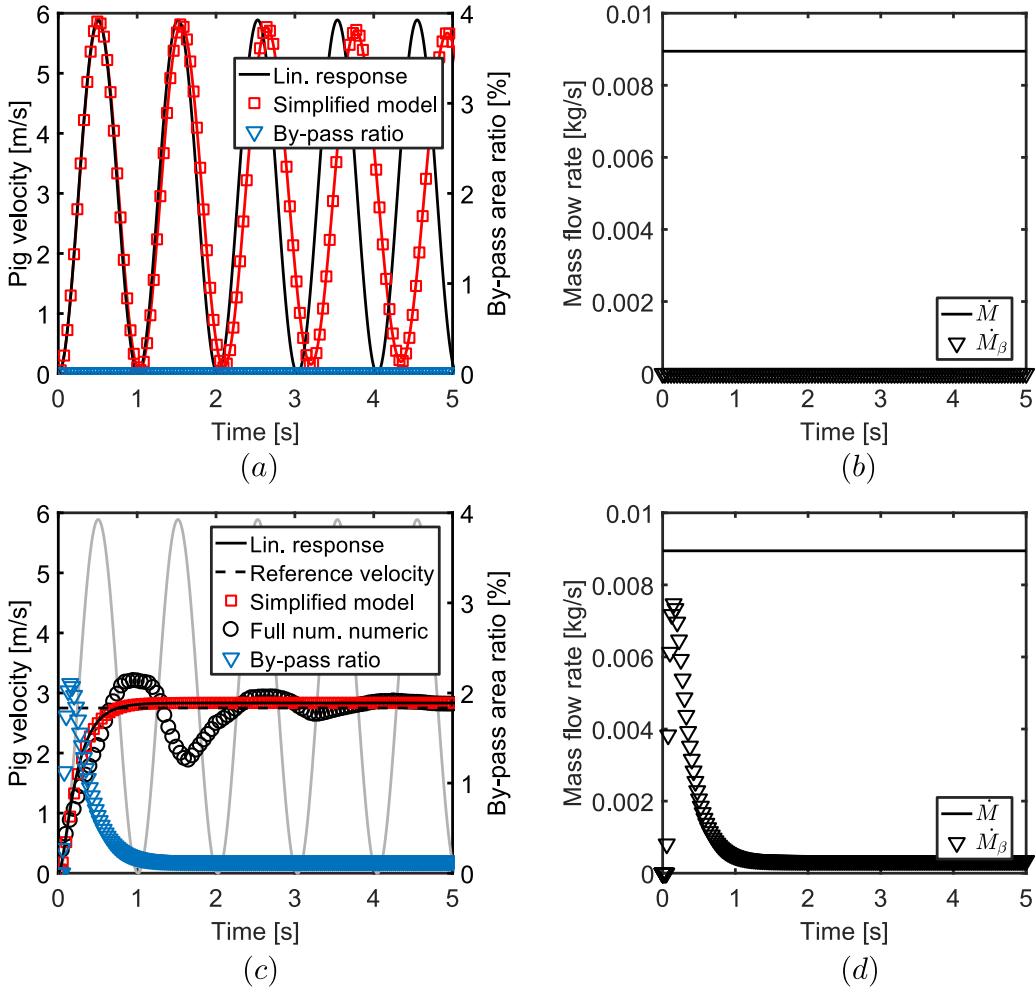


Figure 4.12: (a) Pig velocity and by-pass opening without control. (b) Mass flow rate without control. (c) Pig velocity and by-pass opening with control. (d) Pig velocity and by-pass opening with control.

velocity, pig acceleration, and the pressure upstream of the pig. Clearly the pig velocity needs to be measured in order to evaluate the error e compared to a preset desired reference velocity. The pig velocity is usually measured by odometer wheels attached to the pig which touch the inner pipe wall and thereby record the velocity, see for example [63]. The acceleration needs to be measured to evaluate de/dt to anticipate on a possible velocity excursion of the pig as soon as it starts moving. The acceleration can be measured with an accelerometer. Measurement of the upstream pressure will help to determine M_0 , which is especially relevant when the local static friction $F_{fric,s}$ is larger than the dynamic friction F_{fric} .

4.5 CONCLUSIONS

The motion of by-pass pigs in a horizontal low pressure gas pipeline has been studied on a laboratory scale. The effect of the by-pass area and of the upstream bulk velocity was analyzed by means of an extensive experimental parameter study.

It was found that the average pig velocity can be well predicted by modelling the pressure loss through the by-pass with the Idelchik correlation and the friction between the pig and the pipe wall with a constant value. The use of the Idelchik correlation has been verified through previous CFD calculations, and is now confirmed experimentally. It was shown that under low pressure conditions the pig motion shows oscillatory motion with high pig velocity excursions due to gas accumulation that may build up behind the pig.

The frequency and amplitude of this oscillatory motion have been described with a simplified model which has been verified against experimental data. Based on the simplified model a PD controller has been formulated in order to reduce the pig velocity excursions. The controller was tested both in the simplified model as well as in a full numerical 1D transient model. In both cases it was shown that the pig velocity excursions are successfully mitigated by the controller. The case example which was used to test the controller thereby demonstrates minimum requirements for the design of a speed controlled pig in a low pressure pipeline.

For further research it is suggested to test a controller based on the simplified model in a laboratory environment while comparing the results with a 1D transient tool, as often these tools are used to predict the motion of a pig in a pipeline upfront. It is thus important that these 1D transient tools are able to capture the essential dynamics of a speed controlled pig in a low pressure pipeline. Based on these findings the controller can be further developed to take into account more physics, such as possible changes in friction while the pig is accelerating. In addition, the measurement of the pig velocity will in reality always contain a certain amount of noise. It is therefore recommended to investigate the sensitivity of the controller to a certain level of noise in a model environment first, before carrying out the experiment.

5

ANALYSIS OF TIME INTEGRATION METHODS FOR THE COMPRESSIBLE TWO-FLUID MODEL

This chapter covers a part of the joined journal publication by B. Sanderse, I. E. Smith, and M. H. W. Hendrix. “Analysis of time integration methods for the compressible two-fluid model for pipe flow simulations.” In: *International Journal of Multiphase Flow* 95 (2017), pp. 155–174.

This chapter contains all the simulation data and figures that have been prepared by M.H.W. Hendrix.

5.1 INTRODUCTION

In the petroleum industry multiphase flow occurs when transporting oil and gas through long multiphase pipeline systems. The behaviour of the flow can take many forms, depending on parameters like fluid velocities, pipe properties and fluid properties. An important flow regime is (hydrodynamic) slug flow, in which liquid pockets, separated by gas bubbles, propagate in an alternating fashion with high speed along the pipeline. Such slugs have a large influence on the sizing of receiving and downstream facilities, such as the mechanical supports of the pipeline system, separators (or slug catchers), compressors, pumps, and heat exchangers. The industry uses various flow models for simulating slug flow, but there is a need for increased accuracy. A promising approach is using so-called slug capturing, through the accurate numerical solution of the one-dimensional two-fluid model. Although this two-fluid model can become ill-posed, this approach is believed to be capable of describing the transition from stratified flow to slug flow, see e.g. [46]. The use of the compressible two-fluid model is necessary to generate slugs at the right frequency [46].

For the time integration of the two-fluid model, the workhorse in both industrial and academic codes has been the first order Backward Euler method, due to its stability and damping properties [8, 16, 46, 64]. The large numerical diffusion, however, requires small time steps; the CFL number based on the liquid velocity is not on the order of 1 but has to be much smaller [46, 55]. Only a few studies mention higher order time integration methods for the two-fluid model [9, 49, 102].

The purpose of the present study is to analyse different time integration methods for the compressible two-fluid model in terms of accuracy, stability and damping properties, and to use them to construct so-called discrete flow pattern maps. In particular, we show that BDF2 is preferred over Backward Euler and Crank-Nicolson because it combines second-order accuracy with L-stability (filtering of acoustic waves at large time steps).

This chapter is organized as follows: first, in section 5.2 the two-fluid model is explained in terms of eigenvalues, stability and flow pattern maps. Section 5.3 describes the spatial (central, upwind) and temporal (Backward Euler, Crank-Nicolson, BDF2) discretizations used in this work. Section 5.4 presents a von Neumann analysis applied to the fully discrete problem and a novel method to assess the stability without requiring symbolic manipulations. Section 5.5 presents two test cases: linear and nonlinear wave growth based on Kelvin-Helmholtz instabilities. Section 5.6 provides concluding remarks.

5.2 GOVERNING EQUATIONS AND CHARACTERISTICS

5.2.1 COMPRESSIBLE TWO-FLUID MODEL

The two-fluid model can be derived by considering mass and momentum balances for the stratified flow of oil and gas in a pipeline. The major assumption in the derivation is that of one-dimensional, stratified flow, with the transverse hydrostatic pressure variation introduced via level gradient terms. Furthermore, we assume isothermal flow so that no energy equation is required, and we neglect surface tension. In contrast to the incompressible model, which is commonly discussed in the literature, we allow the gas phase to be compressible (the extension to compressible liquid is straightforward). This leads to the presence of acoustic waves in the solution, which in turn has an effect on the choice of the time integration method, as will become clear later. With these assumptions, the two fluid model consists of the conservation equations for mass and momentum for the gas and liquid phase, reading:

$$\frac{\partial}{\partial t} (\rho_g \mathcal{A}_g) + \frac{\partial}{\partial s} (\rho_g u_g \mathcal{A}_g) = 0, \quad (5.1)$$

$$\frac{\partial}{\partial t} (\rho_l \mathcal{A}_l) + \frac{\partial}{\partial s} (\rho_l u_l \mathcal{A}_l) = 0, \quad (5.2)$$

$$\begin{aligned} \frac{\partial}{\partial t} (\rho_g u_g \mathcal{A}_g) + \frac{\partial}{\partial s} (\rho_g u_g^2 \mathcal{A}_g) = & -\frac{\partial p}{\partial s} \mathcal{A}_g + \text{LG}_g - \tau_{gl} P_{gl} - \tau_g P_g \\ & - \rho_g \mathcal{A}_g g_s + F_{\text{body}} \mathcal{A}_g, \end{aligned} \quad (5.3)$$

$$\begin{aligned} \frac{\partial}{\partial t} (\rho_l u_l \mathcal{A}_l) + \frac{\partial}{\partial s} (\rho_l u_l^2 \mathcal{A}_l) = & -\frac{\partial p}{\partial s} \mathcal{A}_l + \text{LG}_l + \tau_{gl} P_{gl} - \tau_l P_l \\ & - \rho_l \mathcal{A}_l g_s + F_{\text{body}} \mathcal{A}_l, \end{aligned} \quad (5.4)$$

supplemented with the volume equation:

$$\mathcal{A}_g + \mathcal{A}_l = A. \quad (5.5)$$

s is the spatial coordinate along the centreline of the pipe. The driving pressure force $F_{\text{body}} = -\frac{dp_{\text{body}}}{ds}$ in the gas and liquid momentum equations is required for the simulations that involve periodic boundary conditions. The friction models are described in appendix D.2. The level gradient (LG) terms differ from the incompressible case and were derived and reported by us in [103]; a similar form was presented in [59]:

$$\text{LG}_g = \frac{\partial \text{HG}_g}{\partial s}, \quad \text{HG}_g = \rho_g g_n \left[(R - h) \mathcal{A}_g + \frac{1}{12} P_{gl}^3 \right], \quad (5.6)$$

$$\text{LG}_l = \frac{\partial \text{HG}_l}{\partial s}, \quad \text{HG}_l = \rho_l g_n \left[(R - h) \mathcal{A}_l - \frac{1}{12} P_{gl}^3 \right]. \quad (5.7)$$

In eq. (5.1) to eq. (5.7), the subscript β denotes the phase, either gas ($\beta = g$) or liquid ($\beta = l$), ρ_β denotes the density of phase β (either liquid or gas), \mathcal{A}_β the cross-sectional

area occupied by phase β (which will also be referred to as the liquid holdup or the gas holdup), R the pipe radius, h the height of the liquid layer measured from the bottom of the pipe, u_β the phase velocity, p the pressure at the interface, τ_β the shear stress (with the wall or at the interface), g the gravitational constant, φ the local inclination of the pipeline with respect to the horizontal, $g_n = g \cos \varphi$ and $g_s = g \sin \varphi$. A_l (or A_g) and h are related by a nonlinear algebraic expression since the pipeline has a circular cross-section (for channel flow one simply has $h = A_l/w$, where w is the width of the channel). Similarly, the wetted and interfacial perimeters P_g , P_l and P_{gl} can be expressed in terms of the hold-up or the interface height (see appendix D.1 for more details). As a result, the two-fluid model features five equations with five unknowns (A_g , A_l , u_g , u_l , p). Depending on the velocity difference between the phases, the two-fluid model is well-posed or ill-posed [7, 57, 83], as will be discussed in the next section.

5.2.2 CHARACTERISTICS

The governing equations of the two-fluid model can be written in quasi-linear form in terms of the primitive variables $\mathbf{W} \in \mathbb{R}^q$ ($q = 4$),

$$\mathbf{W} = \begin{pmatrix} A_l \\ u_l \\ u_g \\ p \end{pmatrix}, \quad (5.8)$$

reading

$$\mathbf{A}(\mathbf{W}) \frac{\partial \mathbf{W}}{\partial t} + \mathbf{B}(\mathbf{W}) \frac{\partial \mathbf{W}}{\partial s} + \mathbf{C}(\mathbf{W}) = \mathbf{0}. \quad (5.9)$$

The eigenvalues can be found by substituting wave-like solutions in the homogeneous part of the equations [19, 40] (so neglecting the third term of eq. (5.9)), i.e. $\mathbf{W} = \hat{\mathbf{W}} e^{I(n_s s + n_t t)}$, leading to

$$\det(n_t \mathbf{A} + n_s \mathbf{B}) = 0. \quad (5.10)$$

By letting $\lambda = -n_t/n_s$ ($= \frac{ds}{dt}$) this can be seen as the generalized eigenvalue problem

$$\det(\mathbf{B} - \lambda \mathbf{A}) = 0. \quad (5.11)$$

When considering an incompressible liquid and a compressible gas, while neglecting the hydraulic gradient term in the gas phase and using the ‘incompressible’ form of the hydraulic gradient of the liquid phase, a simple expression for the characteristic equation can be obtained (see also [23]):

$$A_g (c_g^2 - (\lambda - u_g)^2) \left(\frac{\partial H G_l}{\partial A_l} + \rho_l (\lambda - u_l)^2 \right) + A_l c_g^2 \rho_g (\lambda - u_g)^2 = 0. \quad (5.12)$$

Here c_g is the speed of sound of the gas phase ($\rho_g = p/c_g^2$). The characteristic equation can be converted to a limit for the velocity difference $\Delta u_{\text{IKH}} = u_g - u_l$ between the phases for which the eigenvalues are real. This is also referred to as the 'inviscid Kelvin-Helmholtz' limit (IKH), see [55]. In our simulations we continuously check the well-posedness of the model by computing the eigenvalues from a quartic that is similar to eq. (5.12), but which includes all compressibility and hydraulic gradient effects. This quartic is evaluated at all gridpoints of the computational domain. When complex eigenvalues are encountered at any location in the domain, the simulation is stopped, since we take the view of Drew and Passman [19] that the original initial boundary-value problem has become meaningless.

5.2.3 STABILITY

To investigate the stability of the equations of the two-fluid model we take the following approach [64, 76]: linearization of the governing equations around a reference state, assuming a travelling-wave solution for the perturbations, and determining the dispersion relation to identify the stability. A similar approach is taken in Liao et al. [55] and Fullmer et al. [25].

We linearize the governing equations by writing $\mathbf{W} = \mathbf{W}_0 + \tilde{\mathbf{W}}$ (where $\tilde{\mathbf{W}} \ll \mathbf{W}_0$), using the fact that the reference state (indicated by $(\cdot)_0$) satisfies the equations, and neglecting products of disturbances. The linearized equations then read:

$$\mathbf{A}_0 \frac{\partial \tilde{\mathbf{W}}}{\partial t} + \mathbf{B}_0 \frac{\partial \tilde{\mathbf{W}}}{\partial s} = \mathbf{C}_0 \tilde{\mathbf{W}}, \quad (5.13)$$

where $\mathbf{A}_0 = \mathbf{A}(\mathbf{W}_0)$, $\mathbf{B}_0 = \mathbf{B}(\mathbf{W}_0)$, and $\mathbf{C}_0 = \left(\frac{\partial \mathbf{C}}{\partial \mathbf{W}}\right)_0$. It is cumbersome to determine \mathbf{C}_0 analytically due to the presence of the friction factors, see equation eq. (D.7), and in general we determine it numerically.

The perturbation is assumed to be of a wave like form: $\tilde{\mathbf{W}} = \epsilon e^{I(\omega t - ks)}$, with ω being the angular frequency and k the wave number. This leads to

$$(\mathbf{A}_0 \cdot (I\omega) - \mathbf{B}_0 \cdot (Ik) - \mathbf{C}_0) \epsilon e^{I(\omega t - ks)} = 0. \quad (5.14)$$

For non-trivial solutions we need

$$\det(\mathbf{A}_0 \cdot (I\omega) - \mathbf{B}_0 \cdot (Ik) - \mathbf{C}_0) = 0. \quad (5.15)$$

This yields the dispersion relation $\omega(k)$. In the absence of source terms ($\mathbf{C}_0 = 0$), the condition for stability ($\text{Im}(\omega) = 0$) is equivalent to the IKH well-posedness limit obtained from the eigenvalue analysis in the preceding section. When source terms are included, the stability condition differs from the well-posedness criterion and the stability limit is commonly known as the viscous Kelvin-Helmholtz (VKH) stability limit.

5.2.4 FLOW PATTERN MAP

An example of the IKH and VKH stability boundaries will be given here for the compressible equations in terms of a flow pattern map. We consider the Kelvin-Helmholtz instability problem, at the same conditions as proposed and analyzed by Liao et al. [55]. A horizontal pipe with a length of one meter is taken ($\varphi = 0$) and its diameter is 78 mm. The density of the gas is given by a perfect gas relation,

$$\rho_g = \frac{p}{c_g^2}, \quad (5.16)$$

where c_g is taken such that for $p = p_0$ we have $\rho_g = 1.1614 \text{ kg/m}^3$. The density of the liquid is constant (incompressible). The superficial liquid velocity is set at 0.5 m/s, and the superficial gas velocity at $u_{s,g} = 6.908 \text{ m/s}$. The liquid hold-up, gas velocity, liquid velocity and pressure gradient follow from the steady state momentum balance and are given, together with other parameters, in table 5.1. Note that ϵ is the hydraulic wall roughness, and μ is the fluid viscosity.

Table 5.1: Parameter values used in the example of the Kelvin-Helmholtz problem.

parameter	value	unit
α_l	0.5	[-]
u_g	13.815	m/s
u_l	1	m/s
ρ_l	1000	kg/m ³
R	0.039	m
p_0	10^5	N/m ²
c_g	293.43	m/s
g	9.8	m/s ²
μ_g	$1.8 \cdot 10^{-5}$	Pa s
μ_l	$8.9 \cdot 10^{-4}$	Pa s
ϵ	10^{-8}	m
F_{body}	74.225	Pa/m

Liao et al. [55] report that the stability limit for the incompressible model is $\Delta U_{\text{IKH}} = 16.0768 \text{ m/s}$. In the compressible model the stability limit slightly changes to $\Delta U_{\text{IKH}} = 16.0355 \text{ m/s}$. Since at the current conditions $\Delta U = 12.815 \text{ m/s}$, the model is well-posed and stable. Note that we have employed Biberg's approximate relation for $\alpha_l(h)$, see equation eq. (D.5), which leads to a small difference in the stability limit compared to the nonlinear relation.

We consider a single wave with $k = 2\pi$ on a domain $s \in [0, 1]$ m. The dispersion analysis, equation eq. (5.14), then leads to 4 waves with the following eigenvalues and angular frequencies:

$$\lambda = \begin{pmatrix} -279.80 \\ 0.69 \\ 1.34 \\ 307.40 \end{pmatrix} \text{ m/s}, \quad \omega = \begin{pmatrix} -1758.05 \\ 4.27 \\ 8.48 \\ 1931.47 \end{pmatrix} + \begin{pmatrix} 4.51\text{I} \\ 0.59\text{I} \\ -0.35\text{I} \\ 4.71\text{I} \end{pmatrix} 1/\text{s}. \quad (5.17)$$

The fact that all eigenvalues are real indicates that the initial condition is indeed well-posed, with $\lambda_{1,4}$ close to the speed of sound of the gas and $\lambda_{2,3}$ close to the liquid velocity. The angular frequencies indicate that out of the four waves there is one unstable mode, ω_3 , which will grow in time.

When repeating this analysis for different superficial liquid and gas velocities the neutral IKH and VKH stability boundaries can be constructed according to $\text{Im}(\omega) = 0$ - see figure 5.1. These neutral stability boundaries are independent of the wave number k [7, 73]. This is in contrast with an analysis which does include the effect of surface tension [18], which has been neglected in the current study. In between the inviscid and viscous stability curves we have a well-posed, unstable solution of the two-fluid model, in which transition from stratified flow to slug flow can possibly occur. The conditions given in table 5.1 are indicated by ‘current conditions’ and they are in this well-posed, unstable regime. Lines of constant hold-up are indicated by dashes in figure 5.1. The resulting flow pattern map and lines are similar to those of [6].

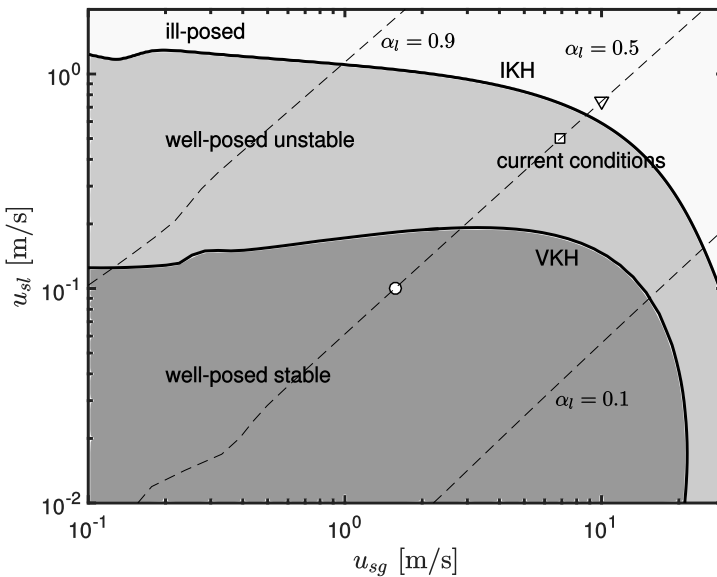


Figure 5.1: Flow pattern map based on Kelvin-Helmholtz instabilities.

5.3 SPATIAL AND TEMPORAL DISCRETIZATION

5.3.1 FINITE VOLUME METHOD ON A STAGGERED GRID

As mentioned in the introduction of this chapter, many options are available for the spatial discretization of the two-fluid model, such as finite difference methods [25, 55], pseudo-spectral methods [41], and characteristics methods [3]. We discretize the two-fluid model, eq. (5.1) to eq. (5.4), by using a finite volume method on a staggered grid. As indicated in figure 5.2, the staggered grid consists of both p-volumes, Ω^p , and u-volumes, Ω^u . Each volume consists of a liquid and a gas phase: $\Omega = \Omega_l \cup \Omega_g$, for both u- and p-volumes.

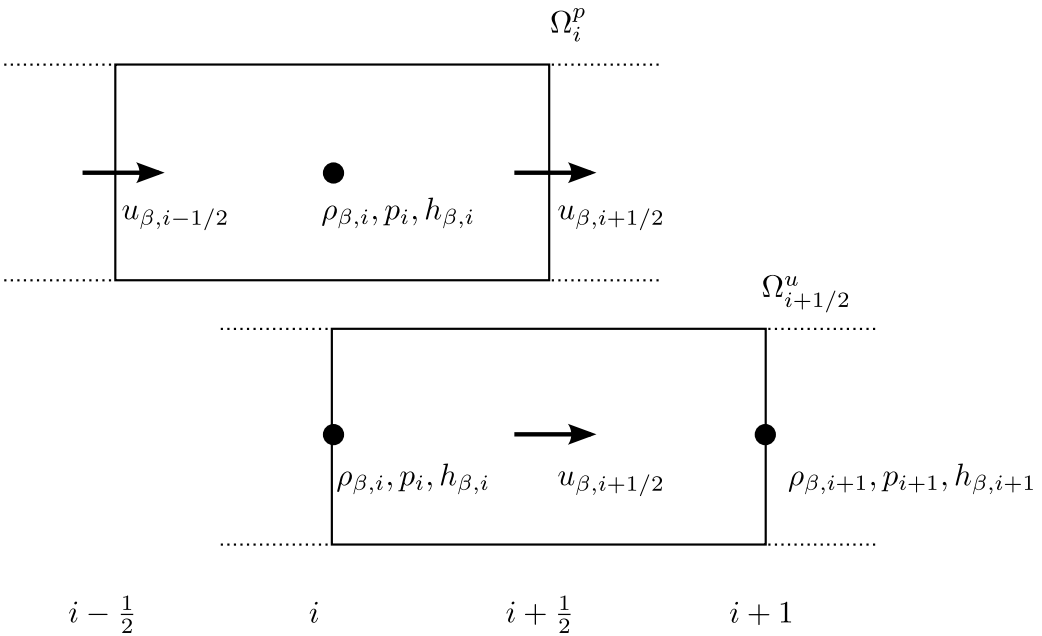


Figure 5.2: Staggered grid layout

We start with conservation of mass for a phase β (β is liquid or gas). Integration of equation eq. (5.1) in s -direction over a p-volume gives:

$$\frac{d}{dt} (\rho_{\beta,i} \Omega_{\beta,i}) + (\rho_{\beta} A_{\beta})_{i+1/2} u_{\beta,i+1/2} - (\rho_{\beta} A_{\beta})_{\beta,i-1/2} u_{\beta,i-1/2} = 0, \quad (5.18)$$

with the finite volume size given by

$$\Omega_{\beta,i} = A_{\beta,i} \Delta s_i. \quad (5.19)$$

The term $(\rho_\beta A_\beta)_{i+1/2}$ requires interpolation from neighbouring values, which is described below. For conservation of momentum we proceed in a similar way. Integration of eq. (5.3) in s -direction over a u -volume gives:

$$\begin{aligned} \frac{d}{dt} (\rho_{\beta,i+1/2} u_{\beta,i+1/2} \Omega_{\beta,i+1/2}) + (\rho_\beta A_\beta)_{i+1} (u_{\beta,i+1})^2 - (\rho_\beta A_\beta)_i (u_{\beta,i})^2 = \\ - A_{\beta,i+1/2} (p_{i+1} - p_i) + LG_{\beta,i+1/2} - \rho_{\beta,i+1/2} \Omega_{\beta,i+1/2} g_s - \\ \sum_{\substack{\gamma \in \{L,G,W\} \\ \gamma \neq \beta}} \tau_{\beta\gamma,i+1/2} P_{\beta\gamma,i+1/2} \Delta s_{i+1/2} + A_{\beta,i+1/2} F_{\text{body}} \Delta s_{i+1/2}, \end{aligned} \quad (5.20)$$

where

$$\Omega_{\beta,i+1/2} = A_{\beta,i+1/2} \Delta s_{i+1/2}, \quad (5.21)$$

and the level gradient terms for the gas and liquid are given by (+ for gas, - for liquid)

$$LG_{\beta,i+1/2} = g \cos(\varphi) \left(\left(h A_\beta \pm \frac{1}{12} P_{gl}^3 \right)_i - \left(h A_\beta \pm \frac{1}{12} P_{gl}^3 \right)_{i-1} \right), \quad (5.22)$$

Several terms in eq. (5.18) and eq. (5.20) require approximation. All terms that are not part of the convective terms are interpolated using a central scheme, e.g. $A_{\beta,i+1/2} = \frac{1}{2}(A_{\beta,i} + A_{\beta,i+1})$. The convective terms, on the other hand, require more care in order to prevent numerical oscillations. Since the system under consideration is (conditionally) hyperbolic, the wave directions have to be taken into account in the differencing scheme, e.g. by using a Roe method [3, 65]. In this work the focus is on the time integration method and we employ standard spatial discretization methods for the convective quantities: first order upwind or second-order central. The central scheme is accurate and stable in our computations since the solutions to the test cases are sufficiently smooth, i.e. we are not simulating discontinuities or flow transitions.

The spatial discretization presented in this section leads to a semi-discrete system, only depending on time, which can be written as

$$\frac{d\mathbf{U}}{dt} = \mathbf{F}(\mathbf{U}), \quad (5.23)$$

where $\mathbf{U} = \mathbf{U}(t) \in \mathbb{R}^{qN}$ is the vector of conserved variables. For periodic boundary conditions, which we will consider, it reads

$$\mathbf{U} = \left[(\rho_g A_g \Delta s)_{1\dots N}, (\rho_l A_l \Delta s)_{1\dots N}, \right. \\ \left. (\rho_g A_g u_g \Delta s)_{1/2\dots N-1/2}, (\rho_l A_l u_l \Delta s)_{1/2\dots N-1/2} \right]^T. \quad (5.24)$$

We use \mathbf{U} instead of \mathbf{W} in a discrete setting to ensure discrete conservation properties.

5.3.2 TEMPORAL DISCRETIZATION

Equation eq. (5.23) forms a system of ordinary differential equations which can be integrated in time with many different time integration methods [11, 31]. A common distinction is between multi-stage methods (Runge-Kutta) and multi-step methods (Adams, Backward Differentiation Formula (BDF)). Within both classes there is a distinction between explicit and implicit methods. Due to the strong time step restriction for explicit methods (caused by the acoustic speeds λ_1 and λ_4), we consider implicit methods. For the two-fluid model, the Backward Euler method is widely applied because of its unconditional numerical stability characteristics, although it has the disadvantage of being only first-order accurate, which introduces a significant amount of numerical diffusion. To construct a second-order method that keeps good stability properties, we consider the Crank-Nicolson and BDF2 methods, which are both second-order accurate and unconditionally stable. Backward Euler, Crank-Nicolson and BDF2 can all be gathered under the following expression:

$$\frac{\alpha_0 \mathbf{U}^{n+1} + \alpha_1 \mathbf{U}^n + \alpha_2 \mathbf{U}^{n-1}}{\Delta t} = \theta \mathbf{F}(\mathbf{U}^{n+1}, t^{n+1}) + (1 - \theta) \mathbf{F}(\mathbf{U}^n, t^n). \quad (5.25)$$

with the parameter values given in table 5.2.

Table 5.2: Parameter values for time integration methods.

scheme	α_0	α_1	α_2	θ
Backward Euler	1	-1	0	1
BDF2	$\frac{3}{2}$	-2	$\frac{1}{2}$	1
Crank-Nicolson	1	-1	0	$\frac{1}{2}$

Equation eq. (5.25) is a system of nonlinear equations and application of Newton's method leads to the following linear system that is solved at each time step:

$$\left[\frac{\alpha_0}{\Delta t} \mathbf{I} - \theta \left(\frac{\partial \mathbf{F}}{\partial \mathbf{U}} \right)^m \right] \Delta \mathbf{U} = - \left[\frac{\alpha_0 \mathbf{U}^m + \alpha_1 \mathbf{U}^n + \alpha_2 \mathbf{U}^{n-1}}{\Delta t} - \theta \mathbf{F}(\mathbf{U}^m, t^{n+1}) - (1 - \theta) \mathbf{F}(\mathbf{U}^n, t^n) \right], \quad (5.26)$$

where m is the iteration counter. If the direct evaluation of \mathbf{F} in terms of \mathbf{U} is not possible - for example in the case of a nonlinear equation of state, when the pressure cannot easily be obtained from the density - we solve equation eq. (5.26) in terms of \mathbf{W} , which requires the evaluation of an additional Jacobian. Solving system eq. (5.26) has roughly the same computational cost for Backward Euler, Crank-Nicolson and BDF2. This is because the

evaluation of the Jacobian is the most expensive part, which is the same for all methods since they are all implicit in time. From an implementation point of view, BDF2 can be implemented relatively easily in an existing code that uses Backward Euler, because the only extra required variable is \mathbf{U}^{n-1} .

The BDF2 method suffers from a start-up problem: \mathbf{U}^{n-1} is not available at the first time step, which is therefore computed with Backward Euler. Note that for variable time steps the coefficients of the BDF2 method become dependent on the time step ratio. Another issue of BDF2 is the fact that it is not unconditionally monotone (neither is Crank-Nicolson), and therefore under- or overshoots can appear near discontinuities [43, 102]. Adaptive time stepping or locally using Backward Euler are possible solutions to this issue. In the test cases reported here this was not required.

5.4 VON NEUMANN ANALYSIS ON THE FULLY DISCRETE EQUATIONS

5.4.1 INTRODUCTION

In the previous sections the eigenvalues of the continuous and semi-discrete equations were discussed. In the fully discrete case a stability analysis can be performed that is very similar to the one applied to the continuous case (section 5.2.3). This is known as von Neumann stability analysis [66], which can be seen as the discrete counterpart of the Kelvin-Helmholtz stability analysis [2]. It is applicable in case of linear, constant coefficient partial differential equations with periodic boundary conditions. We employ therefore the linearized equations in order to be able to apply the von Neumann analysis. As an example, we first consider the equations that result from applying the Backward Euler method:

$$\frac{\tilde{\mathbf{U}}^{n+1} - \tilde{\mathbf{U}}^n}{\Delta t} = \mathbf{J}\tilde{\mathbf{U}}^{n+1}, \quad (5.27)$$

where $\tilde{\mathbf{U}}$ contains the conservative variables defined on the staggered grid as shown in figure 5.2.

In the von Neumann analysis, which is essentially a discrete Fourier analysis [66], the solution is assumed to consist of a finite sum of discrete waves, each with a different wave number:

$$\tilde{\mathbf{U}}_i^n = \sum_m (\mathbf{V}_i^n)_m, \quad (5.28)$$

$$(\mathbf{V}_i^n)_m = e^{ik_m s_i} \mathbf{v}_m^n = e^{ik_m s_i} \mathbf{G}_m^n \hat{\mathbf{v}}_m, \quad (5.29)$$

where m indicates the mode number, k_m the wave number of mode m , $\mathbf{G} \in \mathbb{C}^{q \times q}$ the amplification matrix of mode m , and $\hat{\mathbf{v}}_m \in \mathbb{C}^q$ the Fourier coefficients of mode m of the initial condition. $q = 4$ is the dimension of the problem. The fact that we employ

an amplification matrix is similar to the approach followed by Fullmer et al. [25], but slightly different from the scalar amplification factor considered by Liao et al. [55]. We will comment later on the relation between the two.

Since equation eq. (5.27) is linear it suffices to consider a single mode $(\mathbf{V}_i^n)_m$ (consisting of solution components at grid points i and $i + 1/2$ due to the staggering) to analyse the stability properties of the discretization method:

$$\begin{pmatrix} V_{1,i} \\ V_{2,i} \\ V_{3,i+1/2} \\ V_{4,i+1/2} \end{pmatrix}^{n+1} - \begin{pmatrix} V_{1,i} \\ V_{2,i} \\ V_{3,i+1/2} \\ V_{4,i+1/2} \end{pmatrix}^n = \Delta t \sum_{j=1}^N \mathbf{J}_{ij} \begin{pmatrix} V_{1,j} \\ V_{2,j} \\ V_{3,j+1/2} \\ V_{4,j+1/2} \end{pmatrix}^{n+1}. \quad (5.30)$$

Since \mathbf{J} contains the spatial discretization it is very sparse. Substituting the Fourier expansion eq. (5.29) into equation eq. (5.30), omitting the subscript m , and dividing each equation by the complex exponential in space, yields the compact expression

$$\begin{pmatrix} v_{1,i} \\ v_{2,i} \\ v_{3,i+1/2} \\ v_{4,i+1/2} \end{pmatrix}^{n+1} - \begin{pmatrix} v_{1,i} \\ v_{2,i} \\ v_{3,i+1/2} \\ v_{4,i+1/2} \end{pmatrix}^n = \Delta t \mathbf{M}(e^{ik_m s_i}) \begin{pmatrix} v_{1,i} \\ v_{2,i} \\ v_{3,i+1/2} \\ v_{4,i+1/2} \end{pmatrix}^{n+1}. \quad (5.31)$$

The full matrix is similar to the one presented by Liao et al. [55], but much more elaborate due to the fact that we employ a 4×4 system including compressibility effects. In section 5.4.3 a method will be proposed which circumvents the explicit formulation of this matrix. We write equation eq. (5.31) in the following generic form, using a notation similar to Fullmer et al. [25]:

$$\mathbf{N}\mathbf{v}^{n+1} = \mathbf{O}\mathbf{v}^n, \quad \text{or} \quad \mathbf{v}^{n+1} = \mathbf{N}^{-1}\mathbf{O}\mathbf{v}^n, \quad (5.32)$$

where for Backward Euler: $\mathbf{N} = \mathbf{I} - \Delta t \mathbf{M}$, and $\mathbf{O} = \mathbf{I}$. The amplification matrix is given by

$$\mathbf{G} = \mathbf{N}^{-1}\mathbf{O}. \quad (5.33)$$

Stability depends on the spectral radius of \mathbf{G} , i.e. the maximum absolute value of the (complex) eigenvalues λ_G of \mathbf{G} . These eigenvalues λ_G follow from the eigenvalue problem

$$\det(\mathbf{N}\lambda_G - \mathbf{O}) = 0, \quad (5.34)$$

and a scalar amplification factor can be defined as $G = \max_i |\lambda_{G,i}|$. The amplification matrix \mathbf{G} is the one used by Fullmer et al. [25], whereas the amplification factor λ_G is used by Liao et al. [55]. \mathbf{G} contains the growth and frequency components of all waves,

which allows the reconstruction of the full solution, which is not possible with λ_G . In section 5.4.3 we will obtain the amplification factors from simulation data only, and this requires the use of the full \mathbf{G} .

Once the amplification matrix \mathbf{G} and the Fourier coefficients \mathbf{v} of the initial condition are known, the solution at a time instance t^n in terms of Fourier coefficients is obtained from

$$\mathbf{v}_m^n = \mathbf{G}_m^n \hat{\mathbf{v}}_m, \quad \text{or} \quad \mathbf{v}_m^{n+1} = \mathbf{G}_m \mathbf{v}_m^n. \quad (5.35)$$

\mathbf{G} contains information about the *growth* of the solution (diffusive errors), and about the *shift* (dispersive errors) of the solution in time.

5.4.2 EXTENSION TO BDF2 AND CRANK-NICOLSON

For the BDF2 scheme, equation eq. (5.31) becomes

$$\mathbf{N}\mathbf{v}^{n+1} + \mathbf{O}\mathbf{v}^n + \mathbf{P}\mathbf{v}^{n-1} = 0, \quad (5.36)$$

where $\mathbf{N} = \alpha_0\mathbf{I} - \Delta t\mathbf{M}$, $\mathbf{O} = \alpha_1\mathbf{I}$, $\mathbf{P} = \alpha_2\mathbf{I}$. This equation can be written as

$$\begin{pmatrix} \alpha_0\mathbf{I} - \Delta t\mathbf{M} & 0 \\ 0 & \mathbf{I} \end{pmatrix} \begin{pmatrix} \mathbf{v}^{n+1} \\ \mathbf{v}^n \end{pmatrix} = \begin{pmatrix} -\alpha_1\mathbf{I} & -\alpha_2\mathbf{I} \\ \mathbf{I} & 0 \end{pmatrix} \begin{pmatrix} \mathbf{v}^n \\ \mathbf{v}^{n-1} \end{pmatrix}, \quad \text{or:} \quad \hat{\mathbf{N}}\mathbf{w}^{n+1} = \hat{\mathbf{O}}\mathbf{w}^n, \quad (5.37)$$

from which the definition of \mathbf{G} follows:

$$\mathbf{G} = \hat{\mathbf{N}}^{-1}\hat{\mathbf{O}} = \begin{pmatrix} -\alpha_1(\alpha_0\mathbf{I} + \mathbf{M})^{-1} & -\alpha_2(\alpha_0\mathbf{I} + \mathbf{M})^{-1} \\ \mathbf{I} & 0 \end{pmatrix}. \quad (5.38)$$

This is a particular case of the more generic linear multistep methods analysed in [43]. The eigenvalues of \mathbf{G} follow from the determinant equation

$$\det(\hat{\mathbf{N}}\lambda_G - \hat{\mathbf{O}}) = \det((\alpha_0\mathbf{I} - \Delta t\mathbf{M})\lambda_G^2 + \alpha_1\lambda_G\mathbf{I} + \alpha_2\mathbf{I}) = 0. \quad (5.39)$$

When including the Crank-Nicolson method this can be generalized to

$$\det\left(\frac{\alpha_0 + \alpha_1\mathbf{G}^{-1} + \alpha_2\mathbf{G}^{-2}}{\Delta t}\mathbf{I} - (\theta\mathbf{M} + (1-\theta)\mathbf{M}\mathbf{G}^{-1})\right) = 0, \quad (5.40)$$

where we write \mathbf{G} instead of λ_G .

5.4.3 AMPLIFICATION FACTOR FROM SIMULATION DATA

In this section we propose an alternative, novel method to obtain the von Neumann amplification factors without the need of doing symbolic manipulations, as this can be cumbersome for nonlinear models with elaborate closure relations, such as in the case of the two-fluid model. The idea is to perform a simulation with a small-amplitude harmonic as initial condition and to derive the amplification matrix by comparing the Fourier transform of the solution at a certain time level to the Fourier transform of solutions at previous time levels. We call this the *automatic* von Neumann analysis, in contrast to the classical *symbolic* von Neumann analysis that uses symbolic manipulations. First, the Fourier coefficients \mathbf{v}_m of mode m are determined from the numerical solution \mathbf{V} by a discrete Fourier transform, similar to equation eq. (5.29):

$$\mathbf{v}_m^n = \sum_i \mathbf{V}_i^n e^{Ik_m s_i} \Delta s_i. \quad (5.41)$$

Given the solutions \mathbf{v}^{n+1} and \mathbf{v}^n , the coefficients of the matrix cannot be determined from eq. (5.35), since we have q equations for q^2 unknowns. We therefore perform q time steps and write

$$\begin{pmatrix} \left| \mathbf{v}_m^{n+1} \right. & \left| \mathbf{v}_m^n \right. & \dots & \left. \mathbf{v}_m^{n+2-q} \right| \\ \left| \right. & \left| \right. & & \left. \right| \end{pmatrix} = \tilde{\mathbf{G}}_m \begin{pmatrix} \left| \mathbf{v}_m^n \right. & \left| \mathbf{v}_m^{n-1} \right. & \dots & \left. \mathbf{v}_m^{n+1-q} \right| \\ \left| \right. & \left| \right. & & \left. \right| \end{pmatrix}, \quad (5.42)$$

or

$$\mathbf{Q}_m^{n+1} = \tilde{\mathbf{G}}_m \mathbf{Q}_m^n, \quad (5.43)$$

from which the matrix $\tilde{\mathbf{G}}_m$ can be readily determined:

$$\tilde{\mathbf{G}}_m = \mathbf{Q}_m^{n+1} (\mathbf{Q}_m^n)^{-1}. \quad (5.44)$$

We write $\tilde{\mathbf{G}}$ instead of \mathbf{G} to distinguish between the symbolic and the automatic von Neumann analysis. For the BDF2 scheme, $\tilde{\mathbf{G}} \in \mathbb{C}^{2q \times 2q}$, and the system of equations is extended to

$$\begin{pmatrix} \left| \mathbf{v}_m^{n+1} \right. & \left| \mathbf{v}_m^n \right. & \dots & \left. \mathbf{v}_m^{n+2-2q} \right| \\ \left| \right. & \left| \right. & & \left. \right| \\ \hline \left| \mathbf{v}_m^n \right. & \left| \mathbf{v}_m^{n-1} \right. & \dots & \left. \mathbf{v}_m^{n+1-2q} \right| \\ \left| \right. & \left| \right. & & \left. \right| \end{pmatrix} = \tilde{\mathbf{G}}_m \begin{pmatrix} \left| \mathbf{v}_m^n \right. & \left| \mathbf{v}_m^{n-1} \right. & \dots & \left. \mathbf{v}_m^{n+1-2q} \right| \\ \left| \right. & \left| \right. & & \left. \right| \\ \hline \left| \mathbf{v}_m^{n-1} \right. & \left| \mathbf{v}_m^{n-2} \right. & \dots & \left. \mathbf{v}_m^{n-2q} \right| \\ \left| \right. & \left| \right. & & \left. \right| \end{pmatrix}. \quad (5.45)$$

In order to construct \mathbf{Q}_m^{n+1} and \mathbf{Q}_m^n , it suffices to take $2q$ time steps and to store the Fourier coefficients at each time step (of course, one can also store the entire solution and calculate the Fourier coefficients afterwards). Once $\tilde{\mathbf{G}}$ is determined, the absolute value of its eigenvalues can be investigated. This has to be done for all wavenumbers, either by rerunning the simulation with an initial condition for each different wave, or performing one simulation with a single initial condition composed of all wavenumbers. This is a simple and fast procedure given that only $2q = 8$ time steps are necessary to reconstruct $\tilde{\mathbf{G}}$. In practice, we have noted that due to the high condition number of \mathbf{Q}^n inaccurate results are sometimes obtained. This can be resolved by increasing the number of time instances in the analysis to for example $4q$, which works well in our simulations. The matrices \mathbf{Q}^n and \mathbf{Q}^{n+1} then become non-square and the solution of eq. (5.45) should be interpreted in a least-squares sense.

To summarize, in this section we have explained two techniques, symbolic and automatic von Neumann analysis. This will be demonstrated for the Kelvin-Helmholtz instability case in section 5.5.1. The first is the classic analysis: substitution of a Fourier series in the discretization matrix and investigating the resulting amplification matrix and its eigenvalues. We have done this by using the symbolic toolbox of Matlab and by direct substitution of the complex exponentials into our code to arrive at symbolic expressions for the amplification matrix. The second technique is based on substituting sinusoidal wave perturbations in the initial conditions, and running the code for several time steps. This can be used to check the outcome of the first technique, but also to obtain amplification matrices for black-box solvers (for instance commercial codes).

5.5 RESULTS FOR VARIOUS TEST CASES

In this section we report the results of three test cases. The first two are related to the Kelvin-Helmholtz instability: the first one considers steady state flow with a small but unstable perturbation in a single wave to validate the linear stability (von Neumann) and accuracy of the time integration methods. The second case considers the same instability but with a much larger perturbation to study the nonlinear wave growth and the identification of ill-posedness. Lastly, in the third test case the propagation of a hold-up wave is investigated, and all the previously investigated concepts of stability, accuracy, ill-posedness are considered. The four cases will be referred to as A, B, C, and D, respectively.

5.5.1 KELVIN-HELMHOLTZ: LINEAR WAVE GROWTH

5.5.1.1 Modified wave number analysis

We consider the Kelvin-Helmholtz instability for the test problem described in section 5.2.4 and with the conditions given in table 5.1. The exact solution to the linearized system of equations eq. (5.13) is given by

$$\mathbf{W}(s, t) = \mathbf{W}_0 + \sum_j \operatorname{Re} \left[\boldsymbol{\varepsilon}_j e^{I(\omega_j t - ks)} \right]. \quad (5.46)$$

The initial condition is obtained by a small perturbation in the liquid hold-up: $\tilde{\alpha}_l = 10^{-6}$. The perturbation vector $\boldsymbol{\varepsilon}_3$ is taken to be the eigenvector associated to the angular frequency ω_3 [55]:

$$\boldsymbol{\varepsilon}_3 = 10^{-4} \begin{pmatrix} 1 \cdot 10^{-2} \\ 7.005 \cdot 10^{-3} - 1.1025 \cdot 10^{-3} I \\ 2.497 \cdot 10^{-1} + 1.186 \cdot 10^{-3} I \\ -3.619 - 6.550 \cdot 10^{-1} I \end{pmatrix}. \quad (5.47)$$

Firstly, we perform a consistency check: simultaneous grid and time step refinement for a fixed wave number $k = 2\pi$ with

$$\mathcal{C}_l \approx 1 \rightarrow \Delta t \approx \Delta s = \frac{1}{N}, \quad (5.48)$$

where \mathcal{C} is the dimensionless time step, similar to the CFL number (which strictly is a stability condition). $k = 2\pi$ is the smallest wave number that can be presented on our periodic simulation domain. The exact growth rate, $\operatorname{Im}(\omega_3) = -0.35$, is compared to the numerically computed growth rates as obtained from the symbolic and the automatic von Neumann analysis:

$$\omega_{vN} = \frac{\ln(\min(\operatorname{Im}(\lambda(\mathbf{G}_m))))}{\Delta t}, \quad \tilde{\omega}_{vN} = \frac{\ln(\min(\operatorname{Im}(\lambda(\tilde{\mathbf{G}}_m))))}{\Delta t}. \quad (5.49)$$

Even though only a single wave is triggered due to the initial perturbation in $\boldsymbol{\varepsilon}_3$, the discrete amplification matrix \mathbf{G} still has four eigenvalues. This is because the Fourier transform of the initial condition does not consist of a single wave, but of four waves. We are interested in the one that is largest in magnitude, since it indicates whether the numerical solution is stable or not. However, in contrast to the classical von Neumann analysis, in this study unstable solutions are not necessarily unwanted, since the differential equation itself has an unstable behaviour [25], which might be associated to slug flow.

Figure 5.3 shows the comparison of ω_3 to ω_{vN} and $\tilde{\omega}_{vN}$, for different grids and discretization schemes. Figure 5.3a shows that all time discretization methods converge to

the exact growth rate upon grid refinement. However, for coarse grids, the Backward Euler method predicts a positive ω (damped solutions), whereas BDF2 and Crank-Nicolson correctly predict growing solutions (albeit with a reduced growth rate). In figure 5.3b this is made more quantitative by computing the error of the discrete models compared to the exact value:

$$\eta = |\omega_3 - \omega_{vN}|. \quad (5.50)$$

It is clear that the use of Backward Euler or the use of the first order upwind scheme limits the accuracy to first order. Figure 5.3b also indicates that for very fine meshes there is a slight discrepancy between the symbolic and automatic von Neumann analysis. This is related to the matrix inversion required for the reconstruction eq. (5.44) in the automatic von Neumann analysis, which can suffer from numerical inaccuracies. For the main purpose of the von Neumann analysis, namely investigating the behaviour of the numerical growth rate or dispersion error as function of phase angle ($\phi = k\Delta s$), this is not an issue.

Secondly, we investigate how waves grow in time, depending on the wave number k and the spatial and temporal discretization. The number of grid points is fixed ($\Delta s = 1/160$ m). The shortest wavelength that can be represented on the grid is $2\Delta s$ (Nyquist limit), corresponding to the wavenumber $k = \pi/\Delta s$, and phase angle $\phi = \pi$. The wave number analysis provides insight into how well waves of different frequency are resolved by the time integration method. It is similar to the analysis for spatial discretization methods done by Liao et al. [55]. Figure 5.4a shows the growth rate $G = \max|\lambda(\mathbf{G})|$ which compares well with the results of [55]. In addition, figure 5.4b shows the growth rate ω_{vN} instead of the amplification factor, which includes the exact solution (denoted by the black dashed line). It is perhaps not surprising to see that Crank-Nicolson ('central in time') with a central scheme in space leads to an accurate prediction of G . In fact, when performing the analysis without friction terms (in the well-posed stable regime), the Crank-Nicolson / central combination leads to $G = 1$ independent of the wavenumber. This is a well-known result for advection equations and also holds for the two-fluid model without source terms. However, the presence of source terms leads to unstable solutions; their growth rate can be captured by the numerical scheme though, with the accuracy of the time integration method. Furthermore, $G = 1$ does not mean that the numerical is exact, but that there are only dispersive errors and no diffusive errors.

For each wavenumber k the corresponding growth rate ω_3 is negative. This agrees with the stability-hyperbolicity theorem [73] which says that the neutral stability limit is independent of the wavenumber. The case of $k = 2\pi$ from figure 5.3 is highlighted as the black vertical line in figure 5.4. For $\phi < 10^{-2}$ all numerical methods perform well - this corresponds to long, low frequency waves which are well resolved. For larger ϕ the numerical damping of all methods becomes apparent. The kinks in the amplification factor and the growth rate are due to the fact that a different eigenvalue (see equation eq. (5.49)) becomes dominant.

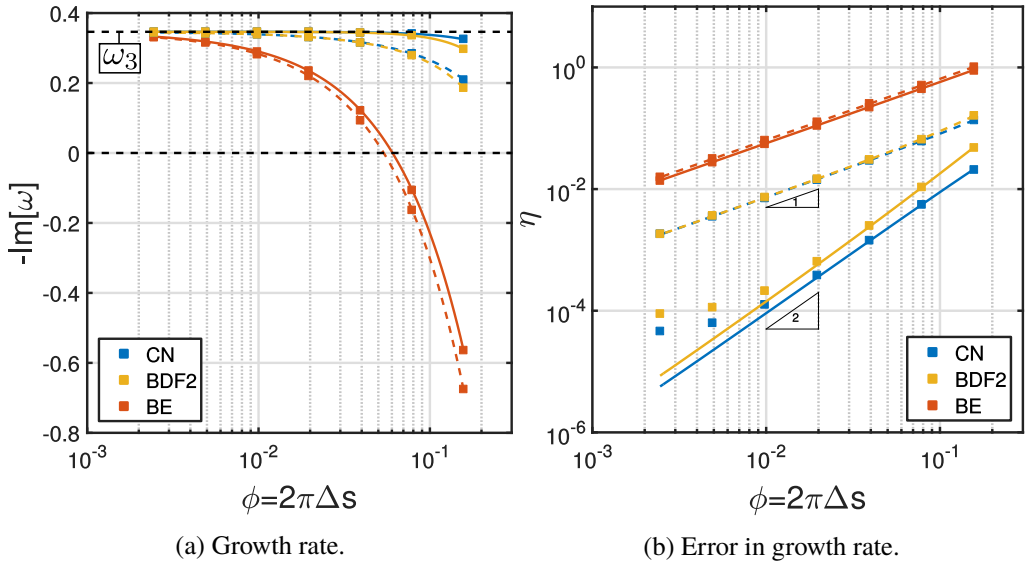


Figure 5.3: Comparison of the growth rate and the error in the growth rate for different discretization methods as a function of the grid size. Squares: automatic von Neumann analysis, lines: symbolic von Neumann analysis. Dashed lines: first order upwind, solid lines: second-order central.

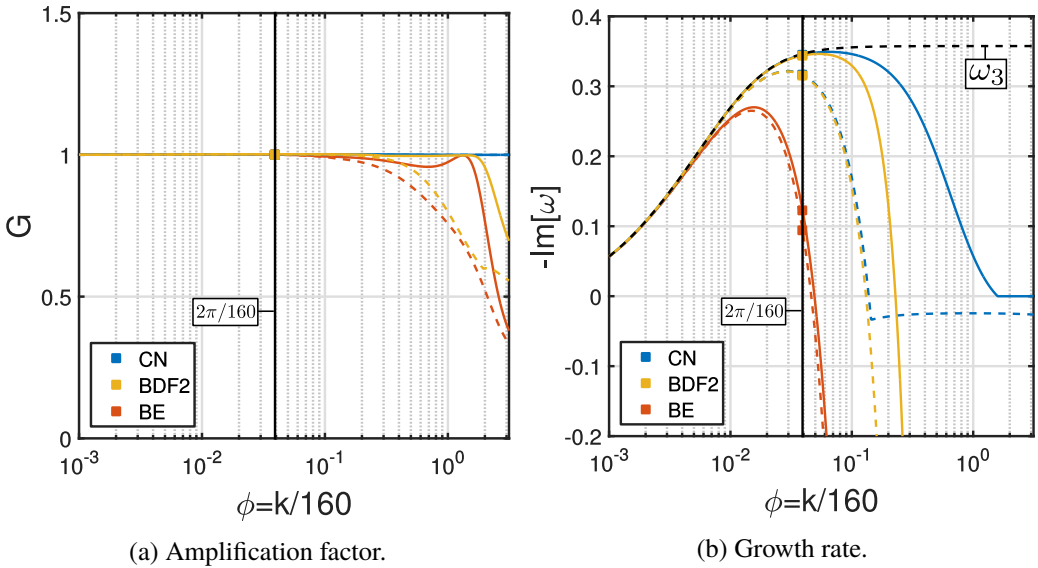


Figure 5.4: Comparison of the growth rate and the error in the growth rate for different discretization methods as as a function of the wave number. Dashed lines: first order upwind, solid lines: second-order central.

5.5.1.2 Linearized discrete flow pattern map prediction

In this section we propose a novel way for displaying the performance of numerical methods, which we call ‘Discrete Flow Pattern Maps’ (DFPM), that uses the growth rate determination method developed for the automatic von Neumann analysis (equation eq. (5.44)). Whereas traditional flow pattern maps, such as the one in figure 5.1, display stable and unstable regimes based on the properties of the differential equations, the DFPM displays the *effective* stability regions that result when the discrete equations are solved, with a certain numerical method and a certain grid and time resolution. Such a map is of crucial importance as an indication whether a discretization method is able to correctly capture the well-posed unstable regime (and the potential transition to slug flow) or whether numerical diffusion overwhelms the physical growth of instabilities.

The DFPM can be constructed in the same way in which we constructed the flow pattern map in figure 5.1. We employ a sequence of superficial liquid and gas velocities, solve the discrete equations with a small perturbation as initial condition and determine the growth rate $\tilde{\omega}_{vN}$ from eq. (5.44) and eq. (5.49). The stability boundary is given by $\text{Im}(\tilde{\omega}_{vN}) = 0$. Figure 5.5a shows the VKH stability boundary for Backward Euler and BDF2 for two different grids (and associated time steps). It can be seen that BDF2 captures the exact stability boundary very accurately on all grids. On the other hand, the effective stability region given by Backward Euler is much larger (note the log scale) than the actual stability region of the differential equations, due to the large amount of artificial diffusion added by Backward Euler. For example, for $N = 40$, and at a superficial gas velocity of $u_{sg} = 10$ m/s, the two-fluid model predicts growing waves at a superficial liquid velocity of $u_{sl} = 0.15$ m/s, but with Backward Euler the wave growth is only apparent when the superficial liquid is increased to $u_{sl} = 0.6$ m/s (already at the ill-posed boundary).

Any simulation starting above the ill-posedness boundary will directly be marked as ill-posed, because our ill-posedness indicator is based on the evaluation of the eigenvalues of the differential equations, see equation eq. (5.12). However, it is possible that, due to nonlinear effects, simulations that start in the well-posed unstable regime grow into the ill-posed regime. This is investigated in the next section.

5.5.2 KELVIN-HELMHOLTZ: NONLINEAR WAVE GROWTH

In this section the simulation from section 5.5.1 is repeated, but with a larger perturbation: $\tilde{\alpha}_1 = 10^{-2}$, and $\tilde{\epsilon}_3 = 10^4 \epsilon_3$. This causes the simulation to quickly enter the nonlinear regime, where waves steepen, possibly leading to slug formation but potentially also to ill-posedness. Based on the results of the previous section, we select BDF2 with $N = 80$ to assess the growth of initial perturbations into the nonlinear regime and whether this leads to ill-posed results. Note that this is different from a previous study [33], in which we have assessed the ‘time to ill-posedness’ as a metric to compare different time integration

methods. In the present study the focus is on whether well-posed unstable solutions can be obtained for long time integration periods.

Similar to the linear case, we perform simulations with the two-fluid model with a central discretization for a range of superficial gas and liquid velocities but now until $t = 100$ s and only with a central discretization of the convective terms. Ill-posedness is investigated by checking if the eigenvalues of the differential equation are real or complex at the conditions predicted by the numerical simulation. If a complex eigenvalue occurs at any point in space or time the corresponding point in the flow pattern map is marked ill-posed. Figure 5.5b shows that the resulting numerical ill-posedness boundary has shifted significantly into the well-posed unstable regime as compared to the ill-posedness boundary of the differential equations (indicated by IKH in figure 5.5b). It appears that *a large part of the well-posed unstable regime of the flow pattern map gives ill-posed solutions when actual numerical simulations are performed*. An example of a simulation which turns ill-posed is case A in figure 5.5b, which corresponds to the conditions studied in section 5.5.1 for linear perturbations. The nonlinear behaviour of the hold-up fraction α_1 in space and time is shown in figure 5.6 for this case. The solution becomes ill-posed already after approximately 5 seconds. The liquid hold-up fraction as a function of time at $s = 1$ m is shown in figure 5.7a.

In addition to case A, three other cases (B, C, and D) are indicated in figure 5.5b which exhibit qualitatively different solution behaviour. Case B in figure 5.7b starts in the well-posed unstable regime, like case A, but after initial growth (as predicted by linear theory) stabilizes and forms a wave with a constant amplitude and frequency. Its shape and position in the flow pattern map indicate that this could be a so-called continuous ‘roll wave’: a particular solution to the two-fluid model which is constant in a reference frame moving with the flow [6, 41, 48]. To check that this is not a numerical artefact, we have confirmed the roll wave presence with a simulation on a much finer grid ($N = 640$). Case C and D are both in the well-posed stable regime, where initial perturbations are damped according to the linear theory. This happens indeed for case D. However, for case C, the damping is very small ($\text{Im}(\omega_3) = 0.01$) and nonlinear effects lead to wave growth and the appearance of new harmonics. The oscillation frequency is now lower because the real part of ω_3 has decreased. Within the time period of 100 seconds displayed in the plot it is unclear if the wave damps out. Continued simulation until 1000 seconds reveals that the wave eventually damps out, like in case D.

We note that the current simulation results are obtained based on a number of simplifications compared to pipeline simulations on actual geometries. First, we employed initial perturbations according to the eigenvector ϵ_3 . This means that the perturbations immediately grow according to linear theory until nonlinear effects take over. Second, we used a single wave with wavenumber $k = 2\pi$. Other wavenumbers will have different frequencies and growth rates and can lead to qualitatively different behaviour (although the VKH and IKH boundaries are independent of wavenumber). Furthermore, the periodic boundary conditions and size of the domain limit the frequencies that can be represented on the

domain. Lastly, we note the black region in figure 5.5b, which indicates the region where the liquid reaches the top of the pipeline. This is not necessarily ill-posed, but outside the scope of our investigation.

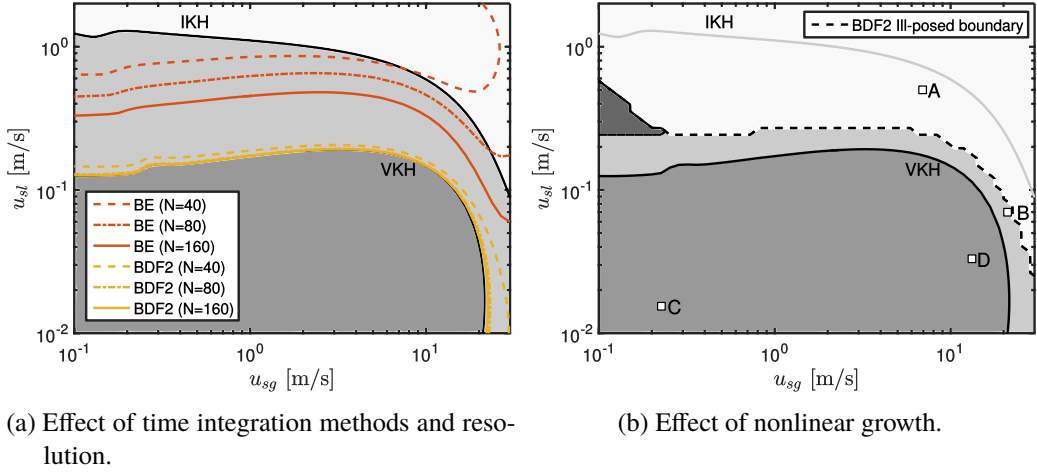


Figure 5.5: Discrete flow pattern maps (DFPM).

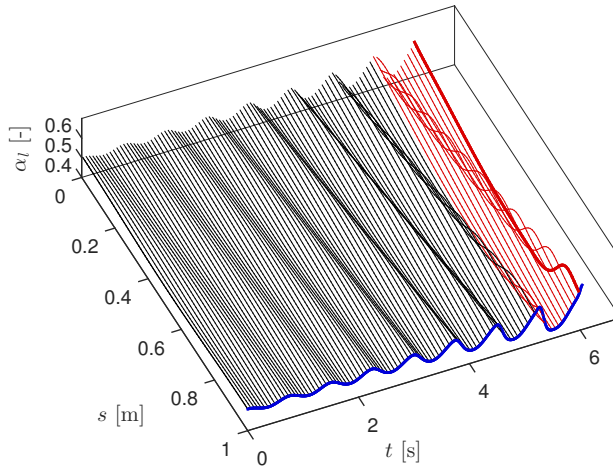
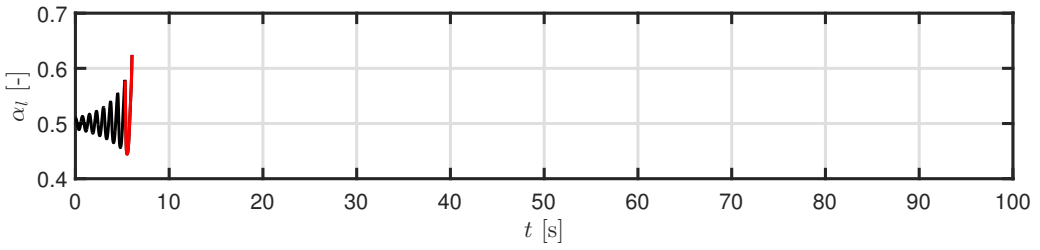
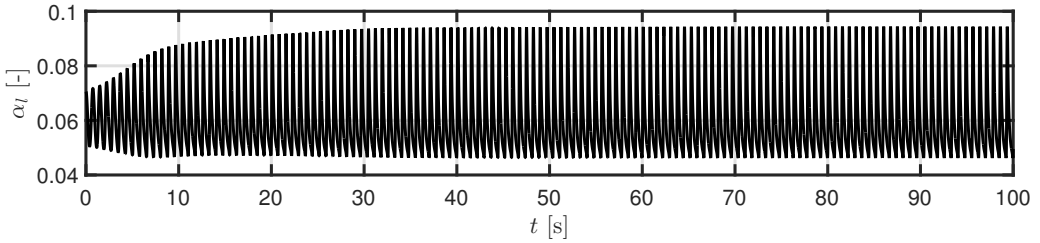


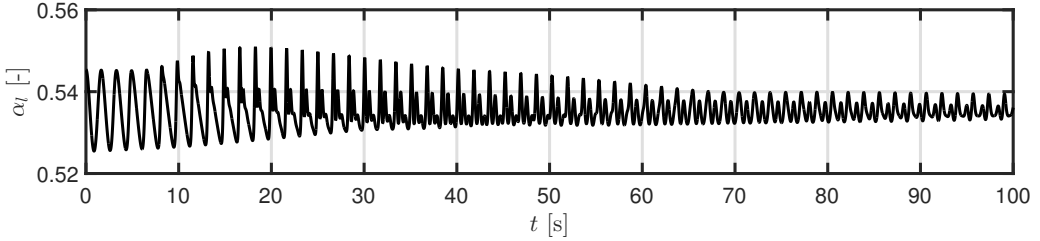
Figure 5.6: Solution in space and time for case A, simulated with BDF2: well-posed unstable solution becoming ill-posed (indicated in red). The blue curve is shown in figure 5.7a.



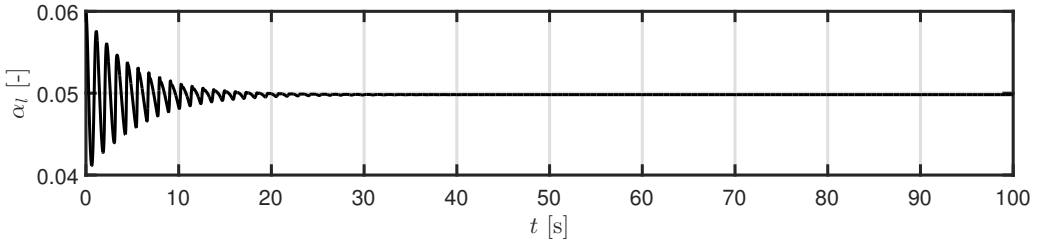
(a) Case A: Well-posed unstable solution turns ill-posed. $u_{sg} = 6.91$ m/s, $u_{sl} = 0.5$ m/s, $\omega_3 = 8.48 - 0.35I$.



(b) Case B: Well-posed unstable solution becomes stationary (roll waves). $u_{sg} = 21.16$ m/s, $u_{sl} = 0.07$ m/s, $\omega_3 = 8.32 - 0.14I$.



(c) Case C: Well-posed stable solution grows, encounters nonlinear effects and then damps. $u_{sg} = 0.23$ m/s, $u_{sl} = 0.015$ m/s, $\omega_3 = 3.73 + 0.01I$.



(d) Case D: Well-posed stable solution damps in time. $u_{sg} = 13.28$ m/s, $u_{sl} = 0.033$ m/s, $\omega_3 = 5.35 + 0.18I$.

Figure 5.7: Numerical solutions for cases A-D as indicated in figure 5.5b, simulated using BDF2.

5.6 CONCLUSIONS

In this chapter we have analysed several time integration methods for the compressible two-fluid model with the goal to simulate stratified wavy flow and slug flow in pipelines in a so-called ‘slug capturing’ approach. The study was focussed on obtaining insight into the numerical pitfalls and requirements. Thereto a theoretical analysis on the differential equations and the discretized equations was given, in particular with respect to their stability properties. The analysis has been demonstrated for a number of test cases.

We conclude that the BDF2 method is a robust time integrator for the two-fluid model and it outperforms the commonly used Backward Euler method and the second-order Crank-Nicolson method. This is due to a combination of its second-order accuracy, A -stability and L -stability. These properties make that BDF2 can be used for the time integration of unsteady problems with a CFL number of 1 based on the liquid velocity, while not suffering from numerical oscillations that arise from acoustic wave propagation.

To facilitate the comparison and understanding of the time integration methods, several techniques have been proposed which have not been applied to the two-fluid model before. First, a new automatic von Neumann analysis technique has been developed as tool for direct evaluation of the stability of the discrete models by running a computer code without requiring symbolic manipulations. This makes it very flexible since it can be directly applied when more physics (e.g. surface tension or axial diffusion) or other spatial discretization methods are included. Second, we have proposed the use of Discrete Flow Pattern Maps (DFPM) to indicate to what extent discretization methods (for a certain choice of the number of grid points and the size of the time step) are able to reproduce the flow pattern maps that are based on the stability of the differential equations. The Discrete Flow Pattern Map reveals that the *effective* well-posed unstable region is well captured by BDF2 but completely missed by Backward Euler, at least for the considered grid and time step resolutions. Simulations in the nonlinear regime furthermore have indicated that ill-posedness can occur when starting from the unstable regime. The implication is that the actual well-posed unstable regime for nonlinear simulations can be much smaller than the theoretical one, which can limit the application of the two-fluid model for simulating the stratified-slug flow transition.

We note that the DFPM as presented here is based on simulations in an idealized setting, with a simple geometry, initial conditions, and boundary conditions. In future work we plan to employ the BDF2 method to further study the formation of slug flow and ill-posedness issues under actual pipeline conditions.

6

MODELLING OF BY-PASS PIGGING IN TWO-PHASE STRATIFIED PIPE FLOW

This chapter is adopted from M.H.W. Hendrix, H.P. IJsseldijk, W.-P. Breugem, and R.A.W.M. Henkes, "Simulation of slug propagation for by-pass pigging in two-phase stratified pipe flow". In: *19th International Conference on Multiphase Technology* (2019), pp. 317-330.

6.1 INTRODUCTION

Several efforts have been made in the past to model the trajectory of a pig, which is propelled by the fluids in a pipeline. These efforts often rely on a 1D cross-sectional description of the fluid, while the pig is modelled as a point mass. The reason for this simplified approach is the high aspect ratio of the problem, which leads to an approach which only considers variations in the direction of the curvilinear coordinate s that runs along the pipeline. Such a 1D approach for the motion of two fluids in a pipeline has been described in chapter 5. The incorporation of a pig in a 1D approach for single phase flow has been briefly discussed in chapter 4. In this chapter we provide more details of the numerical implementation, and focus on the development of a 1D numerical model for pig motion in two-phase flow.

Kohda et al. [50] were among the first to present a numerical method for the motion of a pig in two-phase pipe flow. A separate coordinate system is used for the pig and the fluid. Their simulation results appeared to be in good agreement with experimental data. However, no details were provided on how the two used coordinate systems are coupled. The incorporation of a by-pass in the pig body using a 1D transient single-phase pigging model has been proposed by Nguyen et al. [67], who employed a method of characteristics (MOC) to solve the hyperbolic partial differential equations. Esmaeilzadeh et al. [22] used a MOC approach to model pig motion in a single phase pipeline, while comparing the modeling results to field data. Nieckele et al. [69] and Hosseinalipour et al. [42] used a finite difference technique to model the motion of a by-pass pig in a single-phase pipeline. Both studies address the necessity of regridding the numerical grid by using an adaptive mesh as the pig moves through the pipe, but it is not clear whether the approaches are mass conservative. Most of the studies for 1D pig modelling in a pipeline focus on single-phase flow, only a few consider the presence of a second phase [47, 50, 61, 97]. Among these studies that considered two-phase flow, only pigs without by-pass are considered.

This chapter describes the development of an accurate 1D numerical method to solve the motion of a pig with and without by-pass in a two-phase pipeline. The pig is implemented as a moving border of the numerical grid on which the two-fluid model is solved using a finite-volume method. The two-fluid model has been described in chapter 5 for use cases with periodic boundary conditions. This is clearly not applicable for monitoring the trajectory of a pig through a pipeline: we will need appropriate boundary conditions at the inlet and outlet of the pipe. We propose the use of characteristic boundary conditions [71, 88]. A similar approach is used to handle the boundary conditions on both sides of the pig. As the pig traverses through the pipe, it is necessary to regrid the finite volumes around the pig, to ensure that the finite-volume sizes do neither get too large nor too small.

The structure of this chapter is as follows. The numerical method covering the discretization and boundary treatment is discussed in section 6.2. The pig motion is described by Newton's second law. To account for different types of friction (static vs. dynamic), a smooth function is designed which addresses the different types of friction. Some mod-

elling results have already been shown in chapter 4, but more details on the numerical implementation are given in 6.3. Test cases considering two-phase flow will be given in section 6.4. Section 6.5 gives conclusions and discusses possibilities for further research.

6.2 NUMERICAL METHOD

The two-fluid model which is used to model the simultaneous transport of a liquid and a gas through a pipeline has been discussed in chapter 5. In that chapter only periodic boundary conditions have been considered, and a body force F_{body} was needed in the momentum equations to keep the flow going (see eq. 5.1 - 5.4). In this chapter we consider the presence of a pig which moves through a (horizontal) pipeline, so instead of periodic boundary conditions, appropriate inlet and outlet conditions are needed. We therefore drop the body forces, and the two-fluid equations read:

$$\frac{\partial}{\partial t} (\rho_g A_g) + \frac{\partial}{\partial s} (\rho_g u_g A_g) = 0, \quad (6.1)$$

$$\frac{\partial}{\partial t} (\rho_l A_l) + \frac{\partial}{\partial s} (\rho_l u_l A_l) = 0, \quad (6.2)$$

$$\frac{\partial}{\partial t} (\rho_g u_g A_g) + \frac{\partial}{\partial s} (\rho_g u_g^2 A_g) = -\frac{\partial p}{\partial s} A_g + \frac{\partial HG_g}{\partial s} + \underbrace{(-\tau_{gl} P_{gl} - \tau_g P_g)}_{S_g}, \quad (6.3)$$

$$\frac{\partial}{\partial t} (\rho_l u_l A_l) + \frac{\partial}{\partial s} (\rho_l u_l^2 A_l) = -\frac{\partial p}{\partial s} A_l + \frac{\partial HG_l}{\partial s} + \underbrace{(\tau_{gl} P_{gl} - \tau_l P_l)}_{S_l}. \quad (6.4)$$

Here A_g and A_l represent the hold-up of the gas and the liquid phase, respectively. The gas and liquid hold-up makeup the total pipe area, $A = A_g + A_l$. The phase velocities for the gas and the liquid are respectively denoted u_g and u_l . The density of the liquid, ρ_l , is taken constant, whereas the density of the gas, $\rho_g = \rho_g(p)$, is given by the ideal gas law (eq. 5.16). Here p is the pressure. HG_g and HG_l denote the hydraulic gradient terms, which are given by eq. 5.6 and eq. 5.7 respectively. The last two terms of Eq. 6.3 and Eq. 6.4 represent an expression for the interfacial friction and wall friction. The shear stress of the gas with the pipe wall is denoted as τ_g and the shear stress of the liquid with the pipe wall is denoted as τ_l . They are expressed by the Fanning friction factor, which is calculated using the Churchill relation, see appendix D.2. The interfacial shear stress τ_{gl} is calculated according to [55]. P_g and P_l denote the wetted perimeters, whereas P_{gl} represents the length of the gas/liquid interface within the pipe cross-sectional area, see

appendix D.1. The friction terms do not include derivatives of unknown quantities and are identified as source terms S_g and S_l :

$$S_g = -\tau_{gl}P_{gl} - \tau_g P_g, \tag{6.5}$$

$$S_l = \tau_{gl}P_{gl} - \tau_l P_l. \tag{6.6}$$

6.2.1 SPATIAL DISCRETIZATION

The two-fluid model (Eq. 6.1 - 6.4) is discretized using the finite volume method on a staggered grid, see figure 6.1. The pig is incorporated as a moving border of a finite volume. As a consequence, the discretization of the equations on the finite volumes adjacent to the pig needs to be adjusted. The pig here moves from left to right as a result of a gas and liquid mass influx at the left boundary which are equal to $\rho_g u_g A_g$ and $\rho_l u_l A_l$ evaluated on the left boundary, and are denoted \dot{M}_g and \dot{M}_l respectively. The right boundary consists of a pressure outlet condition p_{out} .

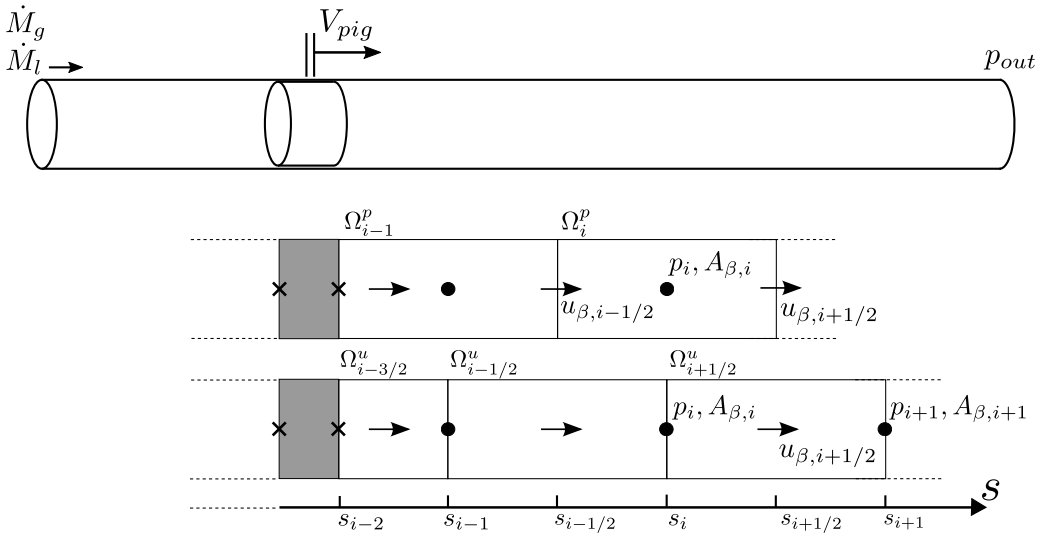


Figure 6.1: Staggered grid layout incorporating the presence of a pig.

The discretization of the mass and momentum equations on finite volumes which lay in the interior of the domain (and thus have no moving boundaries), such as Ω_i^p and $\Omega_{i+1/2}^u$ as shown in figure 6.1, has been discussed in section 5.3 and is given by:

$$\frac{d}{dt} (\rho_\beta \Omega_\beta)_i + (\rho_\beta A_\beta)_{i+1/2} u_{\beta,i+1/2} - (\rho_\beta A_\beta)_{\beta,i-1/2} u_{\beta,i-1/2} = 0, \tag{6.7}$$

$$\begin{aligned} \frac{d}{dt} (\rho_\beta u_\beta \Omega_\beta)_{i+1/2} + (\rho_\beta A_\beta u_\beta^2)_{i+1} - (\rho_\beta A_\beta u_\beta^2)_i = \\ - A_{\beta,i+1/2} (p_{i+1} - p_i) + (HG_{\beta,i+1} - HG_{\beta,i}) + S_{\beta,i+1/2}, \end{aligned} \quad (6.8)$$

where

$$\Omega_{\beta,i} = A_{\beta,i} \Delta s_i. \quad (6.9)$$

Here $\Delta s_i = (s_{i+1/2} - s_{i-1/2})$ is the length of the finite volume. We now focus on the discretization of finite volumes adjacent to the pig, such as Ω_{i-1}^p and $\Omega_{i-3/2}^u$. For the moment we assume that no by-pass is present in the pig body. As a result, the discretization of the convective term results in a zero contribution from the left cell face of the finite volume. The spatial discretization of the mass equation for phase β (where $\beta = g$ represent gas, and $\beta = l$ represents liquid) on Ω_{i-1}^p then reads:

$$\frac{d}{dt} (\rho_\beta \Omega_\beta)_{i-1} + (\rho_\beta A_\beta)_{i-1/2} u_{\beta,i-1/2} = 0, \quad (6.10)$$

Here $\Omega_{\beta,i-1}$ is a function of time. Similarly, the discretization of the momentum equation on the finite volume $\Omega_{i-3/2}^u$ reads:

$$\begin{aligned} \frac{d}{dt} (\rho_\beta u_\beta \Omega_\beta)_{i-3/2} + (\rho_\beta A_\beta)_{i-1} u_{\beta,i-1}^2 = \\ - A_{\beta,i-3/2} (p_{i-1} - p_{i-2}) + (HG_{\beta,i-1} - HG_{\beta,i-2}) + S_{\beta,i-3/2}. \end{aligned} \quad (6.11)$$

Note that p_{i-2} is the pressure at the downstream side of the pig. This pressure follows from appropriate boundary conditions, which are explained in section 6.2.3. The discretization of the finite volumes which are located on the left side of the pig are adjusted in a similar way.

6.2.2 REGRIDDING

As the pig traverses through the pipe, the finite volume in front of the pig will reduce in size and the finite volume at the back of the pig will increase in size. We solve our system of equations in conservative form (see also section 5.3), which means that we solve for the total mass $U_{mass,i} = \rho_{\beta,i} \Omega_i^p$ and total momentum $U_{mom,i+1/2} = (\rho_\beta u_\beta \Omega^u)_{i+1/2}$. Since the size of the finite volume is part of the conservative variable $U_{mass,i}$ and $U_{mom,i+1/2}$, the change of the size of the finite volume due to the motion of the pig is naturally captured. The pig motion is solved by applying Newton's second law, which we will discuss in more detail in section 6.3. The pig position and pig velocity are appended

to the vector of unknowns which contains $U_{mass,i}$ and $U_{mom,i+1/2}$ for each finite volume. The resulting system of equations is solved in a monolithic fashion. Since the pig position and pig velocity are part of the solution, there always exists a mapping of U_i to the primitive variables $u_{\beta,i}$, $\rho_{\beta,i}$ and $A_{\beta,i}$.

As a result of the current approach, the finite volume in front of the pig will at some point become too small, whereas the finite volume at the back of the pig will become too large. Therefore, the grid has to be regularly regenerated as the pig traverses through the pipe. We perform the grid regeneration as follows. When the finite-volume cell in front of the pig gets smaller than half the size of a cell as found in the interior, it will be merged with its neighbouring cell. Similarly, if the cell at the back of the pig gets larger than 1.5 the size of a cell as found in the interior, it will be split up in two cells, see figure 6.2. The conservative variable U_i will be reconstructed accordingly. The mass $U_{mass,i}^*$ of the volume in front of the pig after regeneration is determined by the sum of the masses of the cells before merging:

$$U_{mass,i+1}^* = U_{mass,i} + U_{mass,i+1} \quad (6.12)$$

The mass of the cells at the back of the pig is distributed proportionally to the length of the newly created cells (which are denoted Δs_{i-1}^* and Δs_i^*):

$$U_{mass,i-1}^* = \frac{\Delta s_{i-1}^* U_{mass,i-1}}{\Delta s_{i-1}} \quad (6.13)$$

$$U_{mass,i}^* = \frac{\Delta s_i^* U_{mass,i-1}}{\Delta s_{i-1}} \quad (6.14)$$

The approach is mass conservative, as $\Delta s_{i-1}^* + \Delta s_i^* = \Delta s_i$, which will be demonstrated in section 6.4.1. The merging and splitting of momentum cells $U_{mom,i+1/2}$ is performed in the same way.

We integrate the system of equations in time using the BDF2 scheme, see section 5.3.2. Before performing a new time step, the grid is regenerated if necessary. As a result of the regridding procedure as described above, we do not have the solution at the previous time step which exists on the new grid. We therefore change the time integration scheme to Backward Euler for the first time step after regridding for all unknowns, as BDF2 cannot be used since it needs the solution at the previous time step. After having performed the first time step following a regridding procedure, we switch back to the higher order BDF2 scheme.

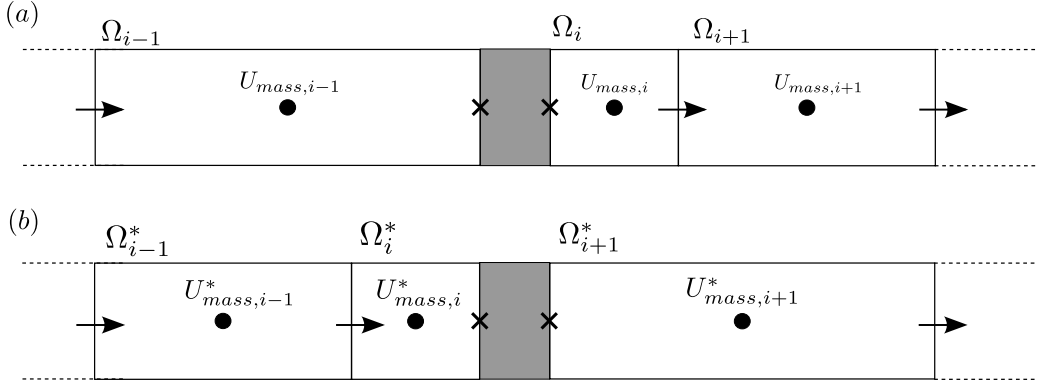


Figure 6.2: Grid regeneration. (a) Grid before regeneration. (b) Grid after regeneration.

6.2.3 BOUNDARY CONDITIONS

Boundary conditions are implemented using a characteristic boundary treatment [71, 88]. We first write eq. 6.1- 6.4 at a boundary point in vector form:

$$\frac{\partial \mathbf{U}}{\partial t} + \frac{\partial \mathbf{F}_0}{\partial s} + \mathbf{D}_0 \frac{\partial \mathbf{W}}{\partial s} = \mathbf{S}. \quad (6.15)$$

Here $\mathbf{U} = [\rho_g A_g, \rho_l A_l, \rho_g u_g A_g, \rho_l u_l A_l]^T$ is the vector containing the conserved variables and $\mathbf{W} = [A_l, p, u_g, u_l]^T$ contains the primitive variables. The source terms S_g and S_l are collected in the vector $\mathbf{S} = [0, 0, S_g, S_l]^T$. We have collected the conservative flux contributions into the second term of eq. 6.15. Here \mathbf{F}_0 is given by:

$$\mathbf{F}_0 = \begin{bmatrix} \rho_g u_g A_g \\ \rho_l u_l A_l \\ \rho_g u_g^2 A_g - H G_g \\ \rho_l u_l^2 A_l - H G_l \end{bmatrix}. \quad (6.16)$$

The non-conservative flux contributions are collected into the third term of eq. 6.15. Here \mathbf{D}_0 is given by:

$$\mathbf{D}_0 = \begin{bmatrix} 0 & 0 & 0 & 0 \\ 0 & 0 & 0 & 0 \\ 0 & A_g & 0 & 0 \\ 0 & A_l & 0 & 0 \end{bmatrix}. \quad (6.17)$$

We now put eq. 6.15 in quasi-linear form by defining Jacobian matrix $\mathbf{A}_0 = \frac{\partial \mathbf{U}}{\partial \mathbf{W}}$ and $\mathbf{J}_0 = \frac{\partial \mathbf{F}_0}{\partial \mathbf{W}}$:

$$\mathbf{A}_0 \frac{\partial \mathbf{W}}{\partial t} + \mathbf{J}_0 \frac{\partial \mathbf{W}}{\partial s} + \mathbf{D}_0 \frac{\partial \mathbf{W}}{\partial s} = \mathbf{A}_0 \frac{\partial \mathbf{W}}{\partial t} + \mathbf{B}_0 \frac{\partial \mathbf{W}}{\partial s} = \mathbf{S}. \quad (6.18)$$

Here $\mathbf{B}_0 = \mathbf{J}_0 + \mathbf{D}_0$, and is given as follows:

$$\mathbf{B}_0 = \begin{bmatrix} -u_g \rho_g & A_g u_g \frac{\partial \rho_g}{\partial p} & A_g \rho_g & 0 \\ u_l \rho_l & 0 & 0 & A_l \rho_l \\ -u_g^2 \rho_g - \frac{\partial H G_g}{\partial A_l} & A_g (u_g^2 \frac{\partial \rho_g}{\partial p} + 1) - \frac{\partial H G_g}{\partial p} & 2A_g u_g \rho_g & 0 \\ u_l^2 \rho_l - \frac{\partial H G_l}{\partial A_l} & A_l & 0 & 2A_l u_l \rho_l \end{bmatrix}. \quad (6.19)$$

We now multiply eq. 6.18 with \mathbf{A}_0^{-1} to obtain:

$$\frac{\partial \mathbf{W}}{\partial t} + \mathbf{Q} \frac{\partial \mathbf{W}}{\partial s} = \mathbf{A}_0^{-1} \mathbf{S}. \quad (6.20)$$

Here $\mathbf{Q} = \mathbf{A}_0^{-1} \mathbf{B}_0$ is given by:

$$\mathbf{Q} = \begin{bmatrix} u_l & 0 & 0 & A_l \\ -\frac{\rho_g (u_g - u_l)}{A_g \frac{\partial \rho_g}{\partial p}} & u_g & \frac{\rho_g}{\frac{\partial \rho_g}{\partial p}} & \frac{A_l \rho_g}{A_g \frac{\partial \rho_g}{\partial p}} \\ -\frac{\frac{\partial H G_g}{\partial A_l}}{A_g \rho_g} & A_g - \frac{\frac{\partial H G_g}{\partial p}}{A_g \rho_g} & u_g & 0 \\ -\frac{\frac{\partial H G_l}{\partial A_l}}{A_l \rho_l} & \frac{1}{\rho_l} & 0 & u_l \end{bmatrix}. \quad (6.21)$$

To derive characteristic equations, from which time dependent equations for the boundary points can be obtained, we determine the eigendecomposition of \mathbf{Q} , that is $\mathbf{Q} = \mathbf{R} \mathbf{\Lambda} \mathbf{R}^{-1}$. Here $\mathbf{\Lambda}$ contains the eigenvalues $[\lambda_1, \lambda_2, \lambda_3, \lambda_4]^T$ on the diagonal and \mathbf{R} contains the right eigenvectors of \mathbf{Q} :

$$\frac{\partial \mathbf{W}}{\partial t} + \mathbf{R} \mathbf{\Lambda} \mathbf{R}^{-1} \frac{\partial \mathbf{W}}{\partial s} = \mathbf{A}_0^{-1} \mathbf{S}. \quad (6.22)$$

The eigenvalues and eigenvectors can be computed analytically with the help of a computer algebra system (in this case Matlab version 2016b has been used). However, the expressions which are obtained are long, so we will not reproduce them here. Now we define the vector $\mathbf{L} = \mathbf{R} \mathbf{\Lambda} \mathbf{R}^{-1} \frac{\partial \mathbf{W}}{\partial s}$ and rewrite eq. 6.22 as follows:

$$\frac{\partial \mathbf{W}}{\partial t} + \mathbf{R} \mathbf{L} = \mathbf{A}_0^{-1} \mathbf{S}. \quad (6.23)$$

Here the components of $\mathbf{L} = [L_1, L_2, L_3, L_4]^T$ are associated to the eigenvalues $[\lambda_1, \lambda_2, \lambda_3, \lambda_4]^T$. The four eigenvalues of the compressible two-fluid model, assuming subsonic flow, contain one negative and one positive eigenvalue close to the speed of sound, say λ_1 and λ_4 respectively. The magnitude of the other two eigenvalues, λ_2 and λ_3 are in the order of the phase velocities and their sign depends on the local flow conditions [23, 80]. We thus consider the following three possibilities: λ_2 and λ_3 are both positive, λ_2 and λ_3 are both negative, and λ_2 is negative while λ_3 is positive. We use the sign of the eigenvalues to determine the number of incoming and outgoing waves at the boundary. By solving eq. 6.23 we can then formulate time dependent equations for the solution at the boundary points. For example, we consider the right boundary point, which corresponds to the outlet of the domain for the cases considered in this work. Figure 6.3 shows the grid layout near the right boundary point.

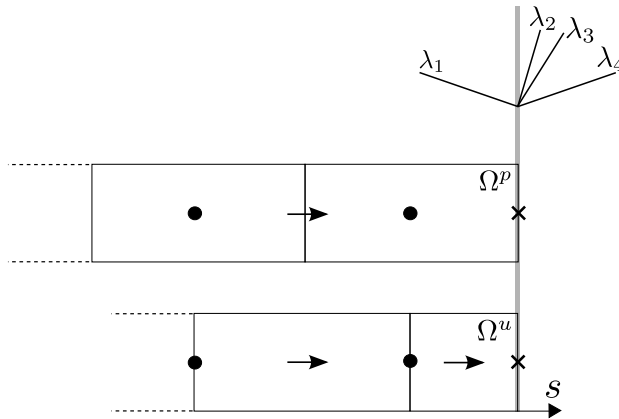


Figure 6.3: Schematic of the grid layout near the right boundary point.

The eigenvalues can be calculated at the boundary point as function of the current solution at the boundary point. A possible outcome could be that λ_2 and λ_3 are both positive, which would imply we have three positive eigenvalues and one negative eigenvalue (since λ_1 and λ_4 are negative and positive respectively). Since we consider the right boundary, three positive eigenvalues correspond to three outgoing waves. This means that the components L_2, L_3 and L_4 of vector \mathbf{L} which feature $\frac{\partial \mathbf{W}}{\partial s}$ can be calculated by using finite differences which are evaluated using the interior of the domain. L_1 should not be calculated in this case, since it corresponds to an ingoing wave, and no information is available in the interior of the domain. Instead information should be given by supplying an appropriate boundary condition by providing an expression for one of the entries vector $\frac{\partial \mathbf{W}}{\partial t}$. A typical boundary condition for an outlet used in this work is an outlet condition for the pressure. A constant outlet pressure corresponds to $\frac{\partial p}{\partial t} = 0$. Eq. 6.23 can now be completely solved since we have 4 unknowns (L_1 and the remaining three unknown entries of vector $\frac{\partial \mathbf{W}}{\partial t}$) and 4 equations. The result is an expression for the full vector $\frac{\partial \mathbf{W}}{\partial t}$ at the boundary point,

which can be integrated together with the interior using the BDF2 scheme. For the left boundary of the domain and the pig boundaries we employ the same technique. For the pig boundaries this results in a boundary condition for the fluid velocity from which the liquid hold-up and pressure can be calculated. For some boundary conditions it may be more convenient to express the boundary equations in terms of conserved variables \mathbf{U} instead of primitive variables \mathbf{W} . For example, at the inlet of the domain one would rather supply boundary conditions in terms of the gas and liquid mass inflow than in terms of gas and liquid velocity. To derive boundary equations in terms of \mathbf{U} , eq. 6.23 is multiplied by Jacobian \mathbf{A}_0 .

6.3 PIG MOTION

The pig motion follows from Newton's second law:

$$\frac{ds}{dt} = v, \quad (6.24)$$

$$m \frac{dv}{dt} = F_p - F_{\text{fric}}. \quad (6.25)$$

Here s and v are the pig position velocity respectively. $F_p = \Delta p A$ is the driving force generated by the pressure drop Δp over the pig and F_{fric} is the friction force which the pig experiences with the inner pipe wall. Whereas F_p can be evaluated by using the pressure upstream and downstream of the pig, F_{fric} needs to be modelled. We make a distinction between the static friction $F_{\text{fric},s}$ which is valid when the pig is not moving, and a dynamic friction $F_{\text{fric},d}$ when the pig is moving. F_{fric} can thus be described by the following equation:

$$F_{\text{fric}} = \begin{cases} \min\{F_p, F_{\text{fric},s}\} & \text{if } v = 0 \\ \text{sgn}(v)F_{\text{fric},d} & \text{if } v \neq 0. \end{cases} \quad (6.26)$$

Usually, $F_{\text{fric},s} > F_{\text{fric},d}$, see chapter 4, where the effect of $F_{\text{fric},s}$ on the maximum pig velocity of a pig undergoing stick-slip motion was discussed. Eq. 6.26 is discontinuous around $v = 0$, which poses a challenge when solving the pig motion numerically. Since we solve the two-fluid equations and the pig motion in a monolithic fashion using Newton's method (see Eq. 5.26), we approximate eq. 6.26 with a smooth function which will aid convergence of the solver. We will explain the construction of this smooth function in more detail in the next section.

6.3.1 A SMOOTH FUNCTION FOR THE PIG FRICTION WITH THE PIPE WALL

In order to design a smooth function which approximates eq. 6.26 we introduce the following functions:

$$H1(c_1, c_2, w_1, s_1, x) = c_1 + \frac{c_2 - c_1}{2} \left(\tanh \left(4 \frac{x - s_1}{w_1} \right) + 1 \right), \quad (6.27)$$

$$H2(c_1, c_2, w_1, s_1, y) = s_1 + \frac{w_1}{\pi} \left(\arcsin \left(2 \frac{y - c_1}{c_2 - c_1} - 1 \right) \right), \quad (6.28)$$

$$H3(c_1, c_2, w_1, s_1, x) = \begin{cases} c_1 & \text{if } x - s_1 < \frac{-w_1}{2} \\ c_1 + \frac{c_2 - c_1}{2} \left(\sin \left(\pi \frac{x - s_1}{w_1} \right) + 1 \right) & \text{if } |x - s_1| \leq \frac{w_1}{2} \\ c_2 & \text{if } x - s_1 > \frac{w_1}{2}. \end{cases} \quad (6.29)$$

We now define an expression for the friction in three zones: a zone in which the pig velocity is negative, a zone in which the the pig velocity is positive, and a zone in which the pig velocity is near zero. The friction in these three zones is defined respectively:

$$F_{\text{fric},1} = H1(-F_{\text{fric},d}, -F_{\text{fric},s}, \frac{v_{\text{trans}}}{2}, -v_{\text{trans}}, v), \quad (6.30)$$

$$F_{\text{fric},2} = H1(F_{\text{fric},s}, F_{\text{fric},d}, \frac{v_{\text{trans}}}{2}, v_{\text{trans}}, v), \quad (6.31)$$

$$F_{\text{fric},3} = H3(-F_{\text{fric},s}, F_{\text{fric},s}, \frac{v_{\text{trans}}}{2}, s_2, v). \quad (6.32)$$

Here s_2 is defined as:

$$s_2 = H2(F_{\text{fric},s}, -F_{\text{fric},s}, \frac{v_{\text{trans}}}{2}, 0, F_p). \quad (6.33)$$

Furthermore, v_{trans} is a constant and is used to determine the pig velocity range over which the friction changes from zone to zone. In order to arrive at an expression for F_{fric} which connects the friction as defined in each of the zones, we now define two switching functions:

$$S_1 = H1(1, 0, \frac{v_{\text{trans}}}{2}, -\frac{v_{\text{trans}}}{2}, v), \quad (6.34)$$

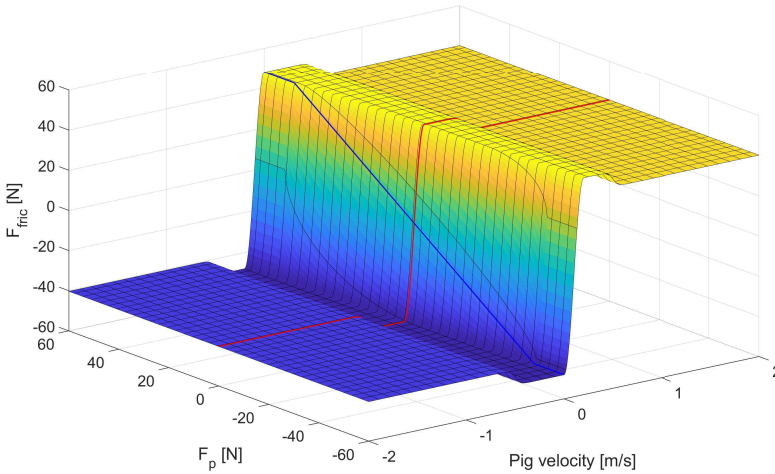
$$S_2 = H1(0, 1, \frac{v_{\text{trans}}}{2}, \frac{v_{\text{trans}}}{2}, v). \quad (6.35)$$

We can then construct a smooth approximation of eq. 6.26, $F_{fric,sm}$, as follows:

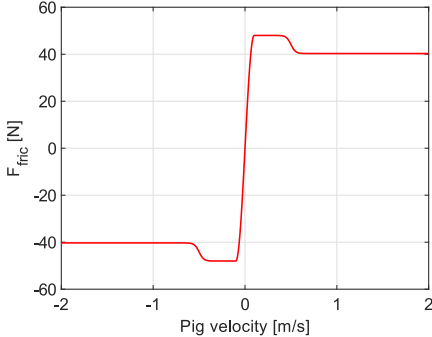
$$F_{fric,sm} = S_1 F_{fric,1} + S_2 F_{fric,2} + (1 - S_1)(1 - S_2) F_{fric,3}. \tag{6.36}$$

Figure 6.4 shows eq. 6.36 evaluated as function of the pig velocity v and the driving force F_p . Here we took $F_{fric,s} = 40.3$ N, and $F_{fric,d} = 48$ N, which represent values as used in section 4.4.2. Furthermore, we took $v_{trans} = 0.5$. This means that transition from $F_{fric,s}$ to $F_{fric,d}$ occurs around $v = 0.5$ m/s, see Figure 6.4b. For visualization purposes we here chose the value of v_{trans} rather big. In practice it is desired that v_{trans} is small, such that the discontinuity in eq. 6.36 is more accurately approximated. In simulations we typically use a value of $v_{trans} = 0.01$.

(a)



(b)



(c)

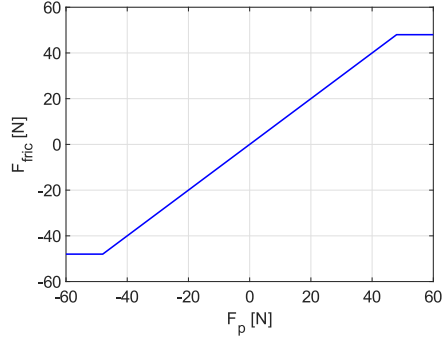


Figure 6.4: (a) A smooth function for the friction force of the pig with the pipe wall. (b) Friction force as function of pig velocity for $F_p = 0$. (c) Friction force as function of F_p for $v = 0$.

6.4 TEST CASES

In this section we discuss two test cases that were performed using the method described in the previous sections. In these test cases we focus on the liquid slug that is accumulated in front of the pig, see figure 6.5. In describing the liquid slug we make use of the definition of the liquid hold-up fraction:

$$\alpha = \frac{A_l}{A}. \quad (6.37)$$

Due to the movement of the pig an increased liquid hold-up fraction α_s exists in this pig-generated slug when compared to the hold-up fraction further downstream, which we denote α_0 . We also define the velocity of the transient that travels ahead of the pig, V_{front} . This front separates two regions: the region downstream of the front, where the flow is still unaffected by the pig motion, and the region upstream of the front where the flow is affected as a result of the pig motion. We first discuss a test case which considers a pig without by-pass. We then move to a test case for pigs with by-pass.

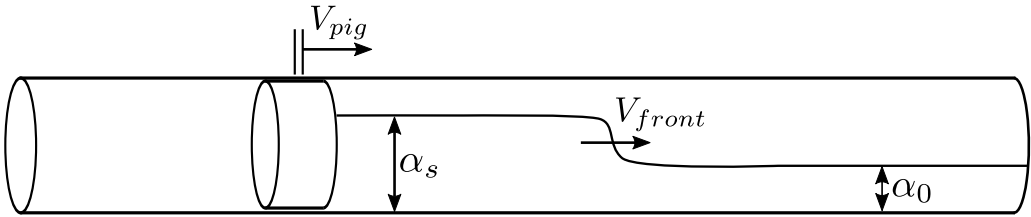


Figure 6.5: Schematic of liquid slug accumulation in front of a moving pig.

6.4.1 PIG-GENERATED SLUG FOR PIGS WITHOUT BY-PASS

As a first step in understanding the liquid slug, which is propelled by a pig in two-phase stratified pipe flow, we assume inviscid flow and a preset pig velocity. In addition, we neglect the pressure gradient $\frac{\partial p}{\partial s}$, which means that we only consider pressure variations due to the hydraulic gradient term. We can then simplify the liquid mass equation 6.2 and the liquid momentum equation 6.4. When applying a mass and momentum balance over the liquid front in a reference frame that moves with the liquid front we can then write the following steady state balance:

$$(V_{\text{pig}} - V_{\text{front}})\alpha_s A = (-V_{\text{front}})\alpha_0 A \quad (6.38)$$

$$(V_{\text{pig}} - V_{\text{front}})^2 \alpha_s A - HG_{l,\alpha=\alpha_s} = (-V_{\text{front}})^2 \alpha_0 A - HG_{l,\alpha=\alpha_0} \quad (6.39)$$

Here $HG_{l,\alpha=\alpha_s}$ is the hydraulic gradient term (see eq. 5.7) evaluated in the slug region in front of the pig, whereas $HG_{l,\alpha=\alpha_0}$ is the hydraulic gradient term evaluated downstream of the liquid front. Inspecting eq. 6.38 and 6.39 we identify two unknowns that characterize the pig-generated slug: α_s and V_{front} . We solve for α_s and V_{front} and compare the result with numerical simulations of the full two-fluid model (eq. 6.1- 6.4), see figure 6.6.

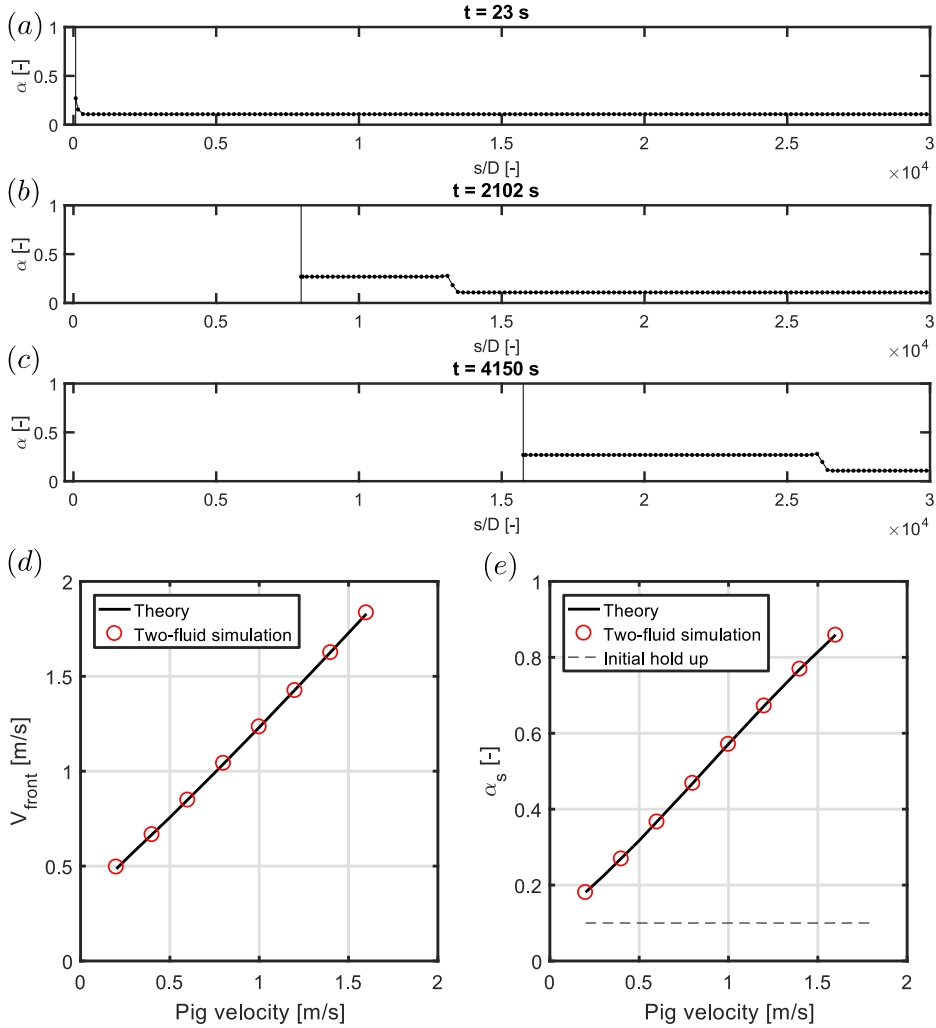


Figure 6.6: Pig generated slug for inviscid flow. (a) Solution at $t = 23$ s. The spatial coordinate s is normalized by pipe diameter D . (b) Solution at $t = 2102$ s. (c) Solution at $t = 4150$ s. (d) V_{front} as function of pig velocity. (e) α_s as function of pig velocity.

The simulations were carried out by considering a pipeline with initial hold-up of $\alpha_0 = 0.1$, with the fluid being at rest. At time $t = 0$ s, a pig is inserted at $s = 0$ m, which is visible in figure 6.6a as a vertical black line. The pig is given a constant preset velocity

$V_{pig} = 0.4$ m/s, and as a result liquid is accumulated in front of the pig, see figure 6.6b/c. We use the properties of water for the liquid phase, whereas we use the properties of air for the gas phase. We further adopt the same pipe diameter D as in [50]. The length of the pipe L is chosen equal to 3840 m. This length is found to be sufficiently long for the holdup waves that are generated to be fully developed. The simulation parameters are summarized in table 6.1.

Table 6.1: Simulation parameters.

Parameter	Value	Unit
Liquid density ρ_l	998	kg/m ³
Gas speed of sound c_g	289	m/s
Liquid viscosity μ_l	$1.0 \cdot 10^{-3}$	Pa s
Gas viscosity μ_g	$1.8 \cdot 10^{-5}$	Pa s
Pipe diameter D	0.105	m
Pipe length L	3840	m
Pipe wall roughness ϵ	$5 \cdot 10^{-6}$	m
Acceleration of gravity g	9.8	m/s ²
Outlet pressure p_{out}	10^5	N/m ²
Number of finite volumes N	200	
Mesh size Δs	19.2	m
Time step Δt	2.56	s

From the simulation results α_s and V_{front} can be extracted, see figure 6.6d/e in which the results for various pig velocities are summarized. A good agreement is found when comparing the simulation result to the theoretical solution for α_s and V_{front} , which is obtained from solving eqs. 6.38 and 6.39.

In order to verify mass conservation of the method, we evaluate the mass error ϵ_β according to the BDF2 scheme:

$$\epsilon_\beta = \left(\frac{3}{2}M_\beta^{n+1} - 2M_\beta^n + \frac{1}{2}M_\beta^{n-1} \right) + \Delta t (F_{\beta,out} - F_{\beta,in}). \quad (6.40)$$

Here M_β is the total mass of phase β which resides in the domain. M_β is simply obtained by summing the mass of the individual finite volumes. $F_{\beta,out}$ and $F_{\beta,in}$ are the outward and inward mass fluxes at the border of the domain respectively. Figure 6.7 shows the evolution of ϵ_β in time, which indeed confirms that the method is mass conserving.

As a next step we consider the same test case, but we include the viscosity of the fluid. The viscosity of the liquid phase will generate an increasing amount of friction with the pipe

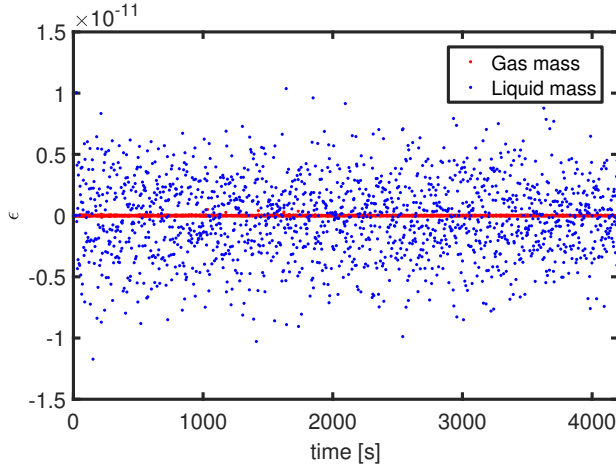


Figure 6.7: Error in liquid and gas mass.

wall. As a result, the liquid hold-up α_s in the pig-generated slug keeps increasing until it hits the top of the pipe, see figure 6.8. For this simulation $V_{pig} = 1.0$ m/s. The time step is taken as $\Delta t = 0.02$ s, whereas the number of volumes is 200. The domain length is 120 m, which results in a mesh size of $\Delta s = 0.6$ m. As a consequence of the liquid that hits the top of the pipe for pigs without by-pass, an initial full-bore liquid slug is formed, which finally can result in a large liquid surge that must be managed by the receiving facilities [21]. The use of a by-pass pig can help to smooth out the liquid surge [21]. This will be the topic of the next section.

6.4.2 PIG-GENERATED SLUG FOR PIGS WITH BY-PASS

The presence of a by-pass in the pig body has two effects on the pig-generated slug. First of all, a by-pass pig will have a lower travel velocity compared to a conventional pig. The steady-state velocity of a by-pass pig in a horizontal pipe can be expressed as follows [37, 82]:

$$V_{pig} = V_{mix} - \frac{d^2}{D^2} \frac{\rho_{bp}}{\rho_{up}} \sqrt{\frac{F_{fric}}{K \frac{1}{2} \rho_{bp} A}}. \quad (6.41)$$

Here $V_{mix} = (u_g A_g + u_l A_l)/A$ is the upstream mixture velocity, d is the diameter of the by-pass hole, ρ_{bp} is the density of the fluid in the by-pass (which is taken as the downstream gas density), ρ_{up} is the upstream density of the gas, F_{fric} is the friction of the pig with the inner pipe wall, and K is the pressure loss coefficient of the by-pass pig. We use the Idelchik relation to calculate K , in which we assume single-phase gas flow

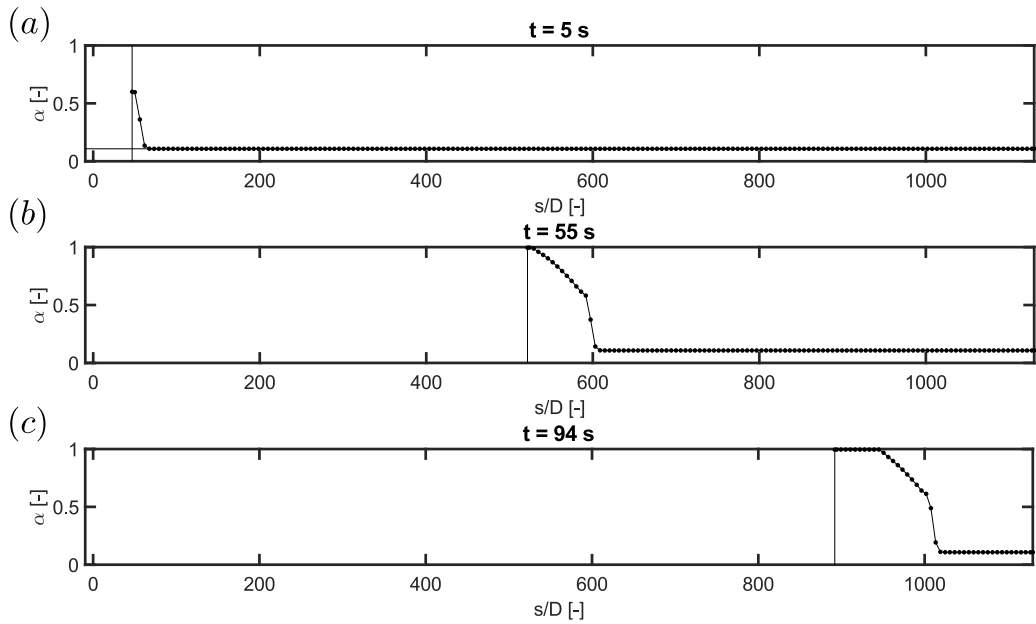


Figure 6.8: Pig-generated slug for viscous flow. (a) Solution at $t = 5$ s. (b) Solution at $t = 55$ s. (c) Solution at $t = 94$ s.

around the by-pass pig [37, 45, 82]. The pig length for calculating K is taken equal to two times the pipe diameter D . Furthermore, we take a value of $F_{\text{fric}} = 10$ N. When the by-pass area fraction $\frac{d^2}{D^2}$ goes to zero, one retrieves a pig velocity equal to the upstream mixture velocity. As a result of the lower pig velocity due to the by-pass, the liquid in front of the pig will also adopt a lower velocity.

A second effect of the presence of a by-pass is that the gas that by-passes will result in a liquid hold-up α_s in front of the pig, which is not equal to one, i.e. the liquid will not reach the top of the pipe. Instead, α_s will reach an equilibrium hold-up; see the results in figure 6.9 for different by-pass ratios. As an initial condition the hold-up fraction has again been settled at 0.1, which was achieved by setting $\dot{M}_l = 0.051$ kg/s and $\dot{M}_g = 0.010$ kg/s at the inlet and solving the steady-state limit of equations 6.3 and 6.4 whereby spatial derivatives (except for the pressure gradient) have been neglected, see also equation 6.44. We carried out a simulation for a pig with a by-pass area fraction of 0.02, which results in $V_{\text{pig}} = 0.3427$ m/s (eq. 6.41). The other simulation parameters are as summarized in table 6.1. To avoid additional transients due to initial acceleration of the pig, we directly set the pig velocity equal to the steady-state pig velocity, as given by eq. 6.41. The equilibrium hold-up α_s is extracted when the hold-up in front of the pig has settled to a steady-state value, see figure 6.9c.

We now proceed to estimate α_s by a simplified model. We therefore again consider the region just downstream of the pig, where $\alpha = \alpha_s$. As a first step we aim to have an

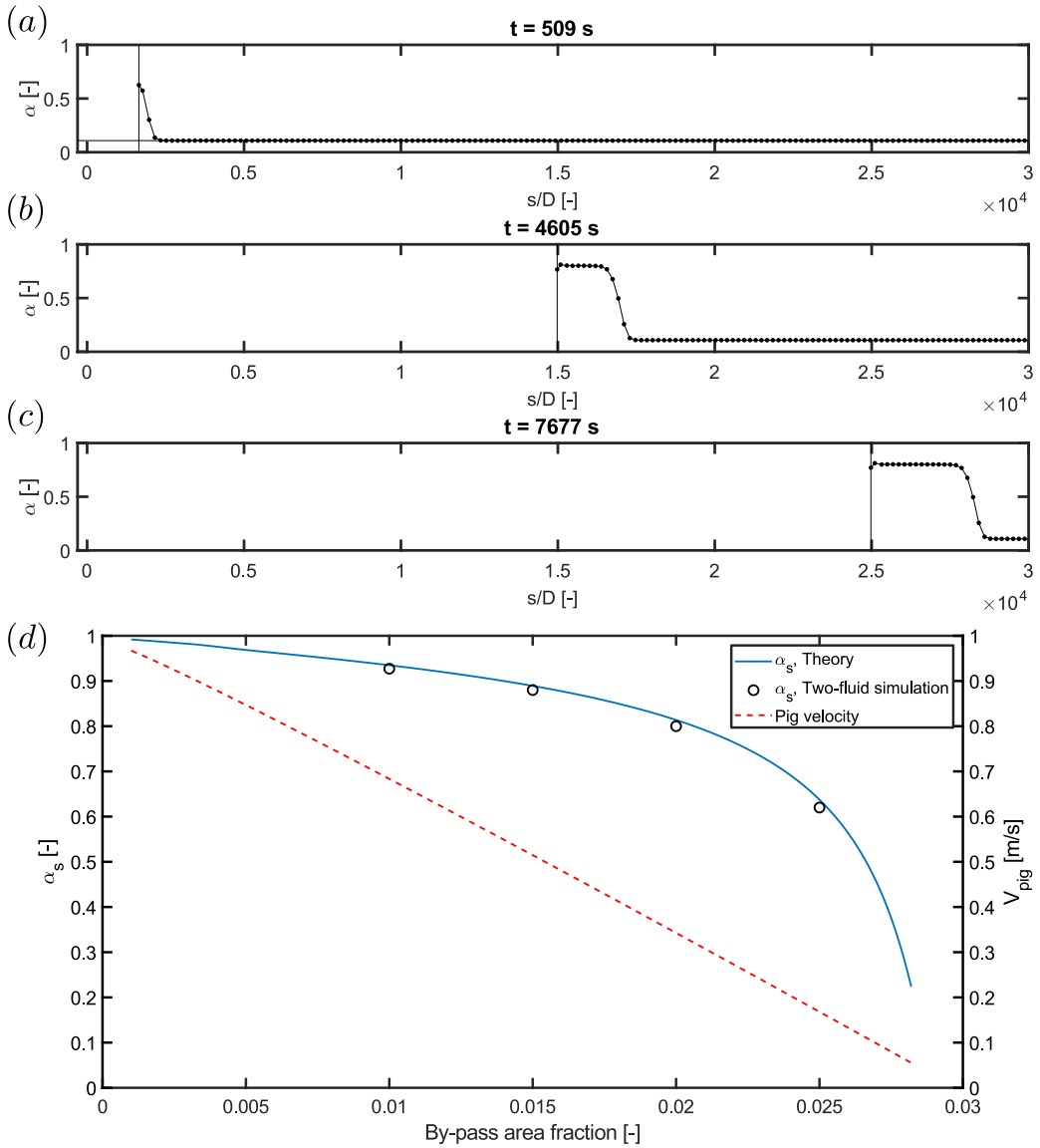


Figure 6.9: Pig-generated slug for a by-pass pig. (a) Solution condition at $t = 509$ s. The by-pass area fraction is equal to 0.02. (b) Solution at $t = 4605$ s. (c) Solution at $t = 7677$ s. (d) α_s and pig velocity (eq. 6.41) as a function of the by-pass area fraction.

expression for the liquid and gas mass flow in this region, denoted $\dot{M}_{l,\alpha=\alpha_s}$ and $\dot{M}_{g,\alpha=\alpha_s}$. As the liquid velocity has adopted the pig velocity, $\dot{M}_{l,\alpha=\alpha_s}$ can be calculated as follows:

$$\dot{M}_{l,\alpha=\alpha_s} = \rho_l V_{pig} \alpha_s A. \quad (6.42)$$

The gas mass flow at this location is determined by the amount of gas that goes through the by-pass pig. It can be calculated by applying a mass balance:

$$\dot{M}_{g,\alpha=\alpha_s} = \rho_{up} (V_{mix} - V_{pig}) A. \quad (6.43)$$

We next use the steady-state limit of the momentum equations 6.3 and 6.4 where we neglect spatial derivatives (except for the pressure gradient), to derive the following point model:

$$\tau_{gl} P_{gl} \left(\frac{1}{1-\alpha_s} + \frac{1}{\alpha_s} \right) + \frac{\tau_g P_g}{1-\alpha_s} - \frac{\tau_l P_l}{\alpha_s} = 0. \quad (6.44)$$

Here the shear stresses are a function of α_s as well as the gas and liquid mass flow, which are given by eq. 6.42 and 6.43. As α_s is the only unknown in equation 6.44, it can be solved, see figure 6.9d. This simplified approach shows good agreement with the numerical simulations, which thus gives insight in characterizing the liquid slug which is propelled by a by-pass pig under the assumption of stratified flow conditions.

6.5 CONCLUSIONS

In this chapter we have discussed the numerical implementation of the pig motion in stratified two-phase pipe flow using a mass conserving two-fluid model. The pig has been implemented as a moving border of a finite volume. A new mass- and momentum-conserving regridding strategy has been proposed and a new implementation of the boundary condition treatment has been realized. Test cases were used to characterize the liquid slug accumulation in front of the pig for both frictionless and frictional flow. The effect of a by-pass in the pig body on the liquid slug has been quantified. Good agreement between the simplified approach and the 1D transient simulations was found.

The current study has been carried out assuming stratified flow. This assumption may not always hold, especially not for the flow just in front of the pig, which may depend on the details of the shape of the pig and of the by-pass holes. A 1D pipe flow model will in general not be able to predict the complex 3D flow close to the by-pass pig. Therefore, it is recommended to carry out two-phase CFD simulations to help developing reliable two-phase correlations which characterize the flow just in front of the by-pass pig. The correlations will serve as input to the 1D model, such as the model presented in this study.

The pig velocity in this study was given the preset steady-state velocity from the start of the simulation. A next step is to test if the assumptions of the simplified model will still hold when startup transients of the pig and the surrounding fluid are included in the full 1D simulation.

7

CLOSURE

The research purpose of the present study was to get a better fundamental understanding of the physics of the pigging of a pipeline with multiphase flow transport in order to improve engineering models used in the industry for pigging operations. The results presented in this thesis show that significant progress has been made.

In particular knowledge was lacking on the two user parameters required for running engineering pipeline models with pigs in the industry, which are the pressure loss coefficient due to the by-passing fluid and the friction between the pig and the pipe wall. By using dedicated lab experiments and different simulation approaches (both 1D, 2D, and 3D) we were able to provide clarity on the fluid flow physics of pigging (particularly by-pass pigging, either without or with speed control) as well as on the frictional force of the pig with the inner pipe wall. The implementation of by-pass pigging in a 1D two-fluid model has been detailed out. After implementation of these new insights in the engineering simulations tools, the industry will obtain more reliable simulation results, which will reduce the risk of operational problems during pigging in the field. This will lead to safer operation, and also to lower operational costs (as there will be less or no production during the pigging event) and lower capital costs (as the size of the slug catcher can be significantly reduced).

The conclusions of the present study and recommendations for future research are given in the two sections below.

7.1 CONCLUSIONS

7.1.1 PRESSURE LOSS DUE TO BY-PASSING FLUID

In chapter 2 a building block approach was applied to describe the pressure loss coefficient K due to the by-passing single-phase fluid in various by-pass pigging geometries. First of all K of the conventional bi-directional by-pass pig has been revisited. Subsequently, new correlations for more complex geometries had been proposed and compared with CFD simulations using the building block approach. This building block approach allowed to construct correlations both for the disk pig geometry and for the speed-controlled pig geometry. A two-solution region was found for the disk pig geometry, which means that there are two stable flow behaviours (type A and type B) within the RANS framework of the current study. Good agreement was found between the proposed correlation for the disk pig and the CFD results, provided that the flow exhibits flow behaviour B. In addition, the pressure loss coefficient of the speed-controlled pig was characterized. It was found that a correlation based on an equivalent disk pig gives qualitatively the right trend, but deviates quantitatively for small opening angles of the holes of the speed-controlled pig. Further research is needed to predict K also for small opening angles of the holes. The obtained correlation for K can be applied in the 1D engineering computer codes that are used in the industry for pigging simulations in multiphase pipelines.

7.1.2 FRICTION BETWEEN THE PIG AND THE PIPE WALL

Static and dynamic experimental setups have been designed to investigate the frictional behaviour of a sealing disc of a pipeline pig. The results were described in chapter 3. The static setup has been used to systematically study the effect of various parameters including the oversize, force ratio, thickness and E-modulus. In this way the study contributes to the fundamental knowledge on parameters influencing the friction force in pigging applications. Being able to test sealing disc configurations for different values of the force ratio μ is important for the industry as this ratio is often unknown and may vary quite substantially. A finite element (FE) model was built that was able to accurately capture the behaviour of the experiments. The finite element model accurately describes the static experiments, by using E-moduli obtained in stress and strain tests and without using any fitting parameters. When similar forces as measured in the experiment are acting on the chamfer in the finite element model, the maximum deformation varies by less than 2 mm for μ values larger than 0.25. Furthermore, the shapes obtained in the experiments agree very well with the shapes obtained with the finite element model. In the current experiment and FE model axisymmetry applies. For future research it could be interesting to investigate the effect of gravity which would break the axisymmetry. This effect is expected to become important when the gravitational forces become comparable with the forces which are purely caused by confining the sealing discs in the pipe.

When the disc is brought to a specific oversize between 1% and 4% in the finite element model, the required forces agree very well with the experimental force data. The maximum deviations for disc A and B occurred at 4% oversize. Here the finite element model underpredicts the friction force by a maximum of 5% and 12%, respectively. It is hypothesized that this underprediction is explained by undesired friction between the hull and the frame in the experimental setup, which is especially observed at high friction forces. To test if this hypothesis is correct a setup could be designed that has more roller bearings between the hull and the frame which would result in even less friction.

The dynamic pig pull facility has been used to test the frictional behaviour during a dynamic pull test through a 1.7-meter pipe for both a dry and a wet contact. This dynamic setup is complementary to the static pig pull facility. The influence of the clamping force of the spacer discs on the sealing disc diameter and frictional force has been investigated. It was found that by increasing the clamping force, the diameter, and therefore the oversize, of the sealing disc increases. As a result, the frictional force was found to increase during the dynamic pull tests. The largest difference in friction force is observed when comparing the dry and the wet experiments. Lubrication was clearly visible in the force measurements. Using water as a lubricant resulted in a decrease in the friction force by between 12% and 16% for the experiments conducted. This decrease in friction force is attributed to a difference in friction coefficient, which has been quantified using FE calculations. The sensitivity of the size of the chamfer in this analysis has been taken into account. This has led to a prediction of the friction coefficient of between 0.97 and 1.30 for a dry contact and

of values between 0.68 and 0.83 for a wet contact. Only water has been used as lubricant in the experiments.

7.1.3 LAB-SCALE PIGGING EXPERIMENTS

The motion of by-pass pigs in a horizontal low-pressure gas pipeline has been studied on a laboratory scale, as described in chapter 4. The effect of the by-pass area and of the upstream bulk velocity was analyzed by means of an extensive experimental parameter study. It was found that the average pig velocity can be well predicted by modelling the pressure loss through the by-pass with the Idelchik correlation and the friction between the pig and the pipe wall with a constant value. The use of the Idelchik correlation has been verified through CFD calculations and is also confirmed experimentally. It was shown that under low-pressure conditions the pig motion shows oscillatory motion with high pig velocity excursions due to gas accumulation that may build up behind the pig.

The frequency and amplitude of this oscillatory motion have been described with a simplified model which has been verified against experimental data. Based on the simplified model a PD controller has been formulated in order to reduce the pig velocity excursions. The controller was tested both in the simplified model as well as in a full numerical 1D transient model. In both cases it was shown that the pig velocity excursions are successfully mitigated by the controller. The case example which was used to test the controller thereby demonstrates minimum requirements for the design of a speed-controlled pig in a low-pressure pipeline.

7.1.4 NUMERICAL METHOD FOR THE 1D TWO-FLUID MODEL

In chapter 5 we have analysed several time integration methods for the compressible two-fluid model with the goal to simulate stratified wavy flow and slug flow in pipelines in a so-called ‘slug capturing’ approach. The study was focussed on obtaining insight into the numerical pitfalls and requirements. Thereto a theoretical analysis on the differential equations and the discretized equations was given, in particular with respect to their stability properties. The analysis has been demonstrated for a number of test cases.

We conclude that the BDF2 method is a robust time integrator for the two-fluid model and it outperforms the commonly used Backward Euler method and the second order Crank-Nicolson method. This is due to a combination of its second order accuracy, A-stability and L-stability. These properties make that the second order BDF2 scheme is suitable for the time integration of unsteady problems, while not suffering from numerical oscillations that arise from acoustic wave propagation.

To facilitate the comparison and understanding of the time integration methods, several techniques have been proposed. First, a new automatic von Neumann analysis technique has been developed as tool for direct evaluation of the stability of the discrete models by

running a computer code without requiring symbolic manipulations. This makes it very flexible since it can be directly applied when more physics (e.g. surface tension or axial diffusion) or other spatial discretization methods are included. Second, we have proposed the use of Discrete Flow Pattern Maps (DFPM) to indicate to what extent discretization methods (for a certain choice of the number of grid points and the size of the time step) are able to reproduce the flow pattern maps that are based on the stability of the differential equations. The Discrete Flow Pattern Map reveals that the effective well-posed unstable region is well captured by BDF2 but completely missed by Backward Euler, at least for the considered grid and time step resolutions. Simulations in the nonlinear regime furthermore have indicated that ill-posedness can occur when starting from the unstable regime. The implication is that the actual well-posed unstable regime for nonlinear simulations can be much smaller than the theoretical one, which can limit the application of the two-fluid model for simulating the stratified-slug flow transition.

7.1.5 PIG SIMULATION WITH THE 1D TWO-FLUID MODEL

In chapter 6 we have discussed the numerical implementation of the pig motion in stratified two-phase pipe flow using a mass conserving two-fluid model. The pig has been implemented as a moving border of a finite volume. A new mass- and momentum-conserving regridding strategy has been proposed and the implementation of the boundary condition treatment has been detailed out. Test cases were used to characterize the liquid slug accumulation in front of the pig for both inviscid and viscous flow. The effect of a by-pass in the pig body on the liquid slug has been quantified. Good agreement between the simplified approach and the 1D transient simulations was found.

7.2 RECOMMENDATIONS FOR FURTHER RESEARCH

7.2.1 NUMERICAL SIMULATIONS

CFD simulations were carried out for single-phase fluid that is flowing through the by-pass area of different pigging configurations. For some conditions two different solutions were found, with hysteresis to move from one branch of solutions to the other branch. It is of interest to further investigate the two-solution region that was found for the disk pig. The boundary of the two-solution region may be sensitive to the parameters of the RANS model, most notably the turbulence model. It would also be interesting to investigate the existence and stability of the two-solution region experimentally in order to further verify the CFD modelling.

It is also recommended to carry out CFD simulations for by-passing with two-phase flow. This will show how the liquid ahead of the pig is being accumulated as a result of the pig propagation. These results can be used for further validation of the 1D pipeline model.

Two-phase simulations, however, are much more complex than single-phase simulations. This is because with two-phase flow a significant pipe length needs to be included in the CFD geometry, whereas for single-phase flow only a small section (with an observer sitting on the pig) is sufficient. In addition, there will be no axi-symmetry, and it may require significant simulation time to reach steady state two-phase flow.

In the 1D by-pass pigging simulations as carried out with the new numerical model, we have assumed stratified flow. This assumption may not always hold, especially not for the flow just in front of the pig, which may depend on the details of the shape of the pig and of the by-pass holes. A 1D pipe flow model will in general not be able to predict the complex 3D flow close to the by-pass pig. Here two-phase CFD simulations can help to develop reliable two-phase correlations which characterize the flow just in front of the by-pass pig. The correlations will serve as input to the 1D model, to improve e.g. the relation for the pressure loss coefficient. The pig velocity in this study was given the preset steady-state velocity from the start of the simulation. A next step is to test if the assumptions of the simplified model will still hold when startup transients of the pig and the surrounding fluid are included in the full 1D simulation.

7.2.2 LAB EXPERIMENTS AND FIELD DATA

Pull tests for oversized pigs were carried out with air and with water. It is recommended to perform similar pull tests also with other lubricants, such as with mineral oil.

It is also recommended to carry out further lab tests with a small-scale speed-controlled pig, using different controller algorithms. It is suggested to test a controller based on the simplified model in a laboratory environment while comparing the results with a 1D transient tool, as often these tools are used to predict the motion of a pig in a pipeline upfront. It is thus important that these 1D transient tools are able to capture the essential dynamics of a speed-controlled pig in a low-pressure pipeline. Based on these findings the controller can be further developed to take into account more physics, such as possible changes in friction while the pig is accelerating. In addition, the measurement of the pig velocity in reality will always contain a certain amount of noise. It is therefore recommended to investigate the sensitivity of the controller to a certain level of noise in a model environment first, before carrying out the experiment.

It would also be highly desirable to use field data for the validation of the model predictions of by-pass pigging. Dedicated campaigns would be required, in which a data logger is attached to the pig. That data logger can measure and register parameters like the local pig velocity, pressure, temperature, rotation and acceleration.

7.2.3 IMPLEMENTATION OF NEW RESULTS

Some work is still needed to make the results obtained in the present study available to the flow assurance engineer, process engineer, or pipeline engineer that is involved in preparing and supporting the pigging operations in the field. In particular the calculation of the friction between the pig and the pipe wall needs to be captured in a design protocol. The single disc deformation as simulated in the present study needs to be repeated for the multiple discs that are part of the actual pig configuration. This will provide the normal force on each of the (oversized) discs. The Coulomb friction coefficient (as obtained from the pull tests with lubrication) applied to the normal forces will provide the total friction force between the pig and the pipe wall. That value can be specified as input for the engineering pipeline simulations.

A

TWO SOLUTION REGION

The two solution region as found in the Fluent CFD results described in chapter 2 is explored by varying the initialization of the solver. Two different approaches are employed. In the first approach the steady state solver is initialized by the default initialization scheme in Fluent [24]. The second approach relies on running a transient simulation until steady state is reached. After the steady state is reached, this solution is used to initialize the transient simulation. In this way it can be verified that the steady state is stable. When these two approaches are applied within the two solution region, the first approach will trigger flow behaviour A, while the second approach will trigger flow behaviour B. This is shown in figure A.1, in which the results from figure 2.9b are taken as an example. The two solution region is indicated by the dashed lines. Figure A.1a shows that outside the two solution region the steady state approach yields the same result as the transient approach.

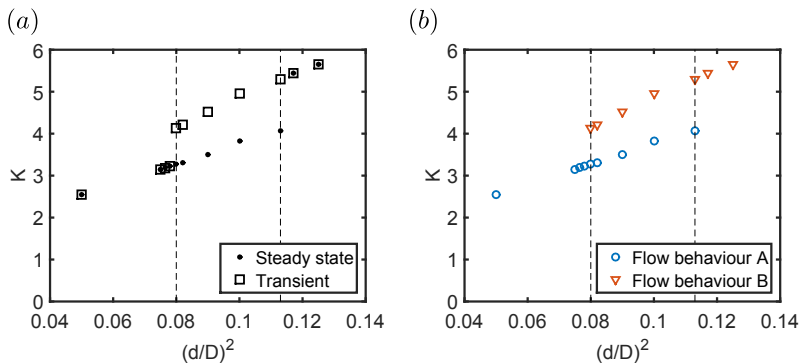


Figure A.1: Pressure loss coefficient. (a) Comparison between steady state and transient approach. (b) Comparison between flow behaviour A and B.

B

MATERIAL TESTS

The Shore hardness is a sealing disc material property. It is a measure of the resistance of a material to indentation. For sealing discs the ASTM D2240 type A scale is used to measure the Shore hardness. Typical values of the Shore hardness A of a sealing disc are in the range: 60 - 85 ([15]). The discs used in chapter 3 are specified by a Shore hardness of 75. The results are shown in Table B.1. The hardness tests were performed on the inner and outer diameters of the discs at ten different positions. The results for the disc A are within the specifications of the manufacturer, but the results for disc B are slightly higher.

An important input parameter for the deformation models discussed in this report is the Young's modulus, also called the elastic modulus or E-modulus; vendors of sealing discs do not specify the E-modulus. There are ways to obtain the E-modulus from the Shore hardness, for example by using Gent's relation. In this research, however, it was chosen to determine the E-modulus by stress-strain tests. From the sealing discs a dog bone is cut using a bandsaw. Each dog bone was tested five times with a universal testing machine, see Figure B.1. One test consists of the following steps:

1. Uniform extension of 10 mm in two minutes
2. Two minutes rest in extended position
3. Uniform compression of 10 mm in two minutes to starting position

During a test the tensile force F and the displacement ΔL are recorded with a frequency of 10 Hz. Using F and ΔL , the stress σ and strain ϵ are determined:

$$\sigma = \frac{F}{A}, \quad (\text{B.1})$$

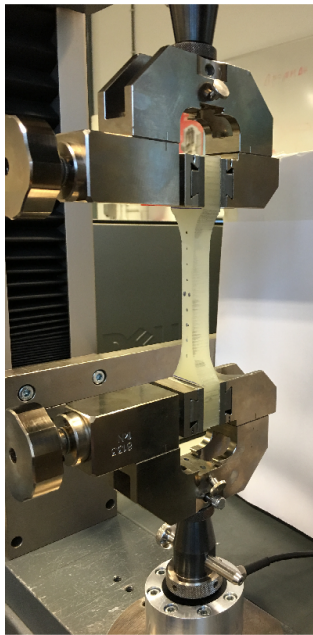
$$\epsilon = \frac{\Delta L}{L}, \quad (\text{B.2})$$

where A is the cross-sectional area in the thin region where the dog bone will stretch mostly and L is the starting length of the dog bone between the specimen holding jaws (here 11.2 cm). The E-modulus is determined by using Hooke's law:

$$E = \frac{\Delta \sigma}{\Delta \epsilon} \quad (\text{B.3})$$

Table B.1: Measured values of the Shore hardness A.

Sample #	Disc A		Disc B	
	Inner diameter	Outer diameter	Inner diameter	Outer diameter
1	75	76	81.5	81
2	75	75	80.5	79.5
3	74.5	74	80.5	79.5
4	74.5	74	80.5	79
5	74	74.5	80	78
6	76.5	75.5	79	80.5
7	76	75.5	79	79.5
8	75.5	75	79	79
9	75	74.5	79	78.5
10	75.5	75	79	79
Avg.	75.2	74.9	79.8	79.4
Std. Deviation	0.75	0.66	0.92	0.88



(a)



(b)

Figure B.1: Universal testing machine. (a) Dog bone disc A. (b) Dog bone disc B.

Figure B.2 shows the E-modulus as function of the tensile strain for disc A and disc B, respectively. The E-modulus of the disc B is significantly higher than that of disc A. Both

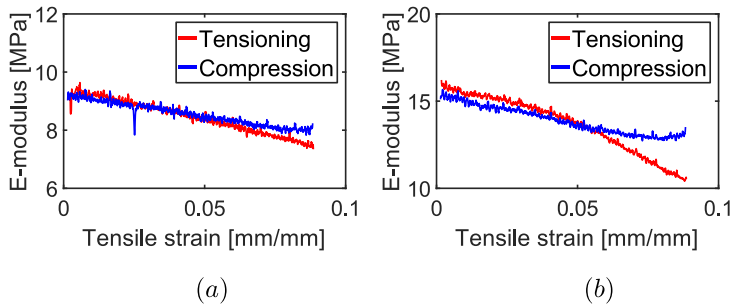


Figure B.2: The E-modulus as a function of the tensile strain. (a) Disc A. (b) Disc B.

materials show a non-linear behaviour and the E-modulus decreases as the strain increases. This non-linearity is most apparent for the disc B when the strains exceed 0.04 mm/mm.

The E-modulus is used as input parameter in the finite element model; it will be a constant, which is equal to the average value of the E-moduli obtained in the five stress-strain tests per dog bone. In our stress-strain tests the displacement increases to 9% of the starting length as higher strains are unlikely to be encountered.

C

DERIVATION OF AN ANALYTIC SOLUTION TO THE SIMPLIFIED MODEL

When substituting in the equation for s_{eq} (equation 4.8) into equation 4.11 we find:

$$\frac{p^*}{\rho^*} \frac{m}{(Ap_{out} + F_{fric})^2} \frac{d^2\delta s}{dt^2} = -\frac{\delta s}{M_0 + \dot{M}t}. \quad (C.1)$$

When defining α_1 and α_2 as:

$$\alpha_1 = \frac{p^*}{\rho^*} \frac{m}{(Ap_{out} + F_{fric})^2} M_0, \quad (C.2)$$

$$\alpha_2 = \frac{p^*}{\rho^*} \frac{m}{(Ap_{out} + F_{fric})^2} \dot{M}, \quad (C.3)$$

we can cast equation C.1 in a more general form:

$$\frac{d^2\delta s}{dt^2} = -\frac{\delta s}{\alpha_1 + \alpha_2 t}. \quad (C.4)$$

A solution to equation C.4 can be found by using Bessel functions:

$$\delta s(t) = C_1 k J_1(2k) - C_2 k Y_1(2k), \quad (C.5)$$

with

$$k(t) = \sqrt{\frac{\alpha_1 + \alpha_2 t}{\alpha_2^2}}. \quad (C.6)$$

Here J_1 is the Bessel function of the first kind with order 1 and Y_1 is the Bessel function of the second kind with order 1. C_1 and C_2 are integration constants. A solution for $\delta v(t)$ can be obtained by differentiating equation C.5:

$$\delta v(t) = \frac{1}{\alpha_2} (C_1 J_0(2k) - C_2 Y_0(2k)). \quad (C.7)$$

Here J_0 is the Bessel function of the first kind with order 0 and Y_0 is the Bessel function of the second kind with order 0. We now substitute the values of a_1 and a_2 into equation C.6 to obtain:

$$k(t) = \sqrt{\frac{a_1 + a_2 t}{a_2^2}} = \sqrt{\frac{1}{a_1 + a_2 t} \left(\frac{a_1}{a_2} + t \right)} = \sqrt{\frac{(A p_{out} + F_{fric})^2}{\frac{p^*}{\rho^*} m (M_0 + \dot{M} t)}} \left(\frac{M_0}{\dot{M}} + t \right). \tag{C.8}$$

When using the definition for s_{eq} , equation 4.8, and subsequently the definition of the local angular frequency ω , equation 4.14, we can further simplify equation C.8 and arrive at equation 4.13:

$$k(t) = \sqrt{\frac{(A p_{out} + F_{fric})}{s_{eq}(t) m}} \left(\frac{M_0}{\dot{M}} + t \right) = \omega(t) \left(\frac{M_0}{\dot{M}} + t \right). \tag{C.9}$$

Similarly, we can rewrite equation C.7 to obtain equation 4.15:

$$\begin{aligned} \delta v(t) &= \frac{1}{a_1 + a_2 t} \frac{a_1 + a_2 t}{a_2} (C_1 J_0(2k) - C_2 Y_0(2k)) \\ &= \omega^2(t) \left(\frac{M_0}{\dot{M}} + t \right) (C_1 J_0(2k) - C_2 Y_0(2k)). \end{aligned} \tag{C.10}$$

D

TWO-FLUID MODEL DETAILS

D.1 GEOMETRY

Referring to the simulations described in chapter 5 and 6, the following geometric identities are used to express the wall perimeters, interfacial perimeter, and liquid height in terms of the wetted angle γ_l :

$$P_{gl} = D \sin \gamma_l, \quad (\text{D.1})$$

$$P_l = D\gamma_l, \quad (\text{D.2})$$

$$P_g = D(\pi - \gamma_l), \quad (\text{D.3})$$

$$h = \frac{1}{2}D(1 - \cos \gamma_l). \quad (\text{D.4})$$

We use Biberg's approximation [10] to express α_l in terms of γ_l (this avoids the iterative solution of a nonlinear equation):

$$\gamma_l = \pi\alpha_l + \left(\frac{3\pi}{2}\right)^{\frac{1}{3}} \left(1 - 2\alpha_l + \alpha_l^{\frac{1}{3}} - \alpha_g^{\frac{1}{3}}\right). \quad (\text{D.5})$$

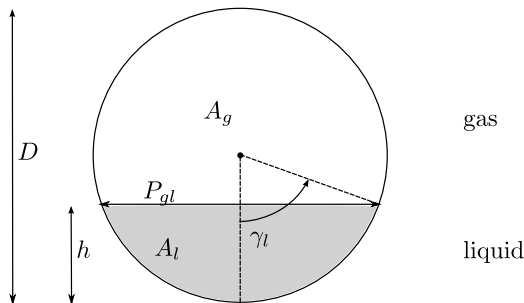


Figure D.1: Stratified flow layout and definitions.

D.2 FRICTION MODELS

The wall (subscript w) and interfacial (subscript gl) shear stress are expressed by the Fanning friction factor definition:

$$\tau = \begin{cases} \frac{1}{2} f_{\beta} \rho_{\beta} u_{\beta} |u_{\beta}| & \text{wall} \\ \frac{1}{2} f_{gl} \rho_g (u_{\beta} - u_{\gamma}) |u_{\beta} - u_{\gamma}| & \text{interfacial} \end{cases} \quad (\text{D.6})$$

The friction factor f_{β} of phase β with the pipe wall is modeled with the Churchill relation [13]:

$$f_{\beta} = 2 \left(\left(\frac{8}{\text{Re}_{\beta}} \right)^{12} + (A + B)^{-1.5} \right)^{\frac{1}{12}}, \quad (\text{D.7})$$

$$A = \left(2.457 \ln \left(\left(\left(\frac{7}{\text{Re}_{\beta}} \right)^{0.9} + 0.27 \frac{\varepsilon}{D_{h\beta}} \right)^{-1} \right) \right)^{16}, \quad (\text{D.8})$$

$$B = \left(\frac{37530}{\text{Re}_{\beta}} \right)^{16}. \quad (\text{D.9})$$

Here ε is the hydraulic pipe roughness, Re_{β} is the Reynolds number,

$$\text{Re}_{\beta} = \frac{\rho_{\beta} u_{\beta} D_{h\beta}}{\mu_{\beta}}, \quad (\text{D.10})$$

and $D_{h\beta}$ is the hydraulic diameter:

$$D_{h\beta} = \begin{cases} \frac{4A_l}{P_{lw}} & \text{if } \beta = l \\ \frac{4A_g}{P_{gw} + P_{gl}} & \text{if } \beta = g \end{cases} \quad (\text{D.11})$$

The interfacial friction factor f_{gl} is calculated by [55]:

$$f_{gl} = \max\{f_g, 0.014\}. \quad (\text{D.12})$$

REFERENCES

- [1] Central Intelligence Agency. *The world Factbook - Country Comparison to the World*. <https://www.cia.gov/library/publications/the-world-factbook/fields/2117.html>. Retrieved July 12, 2019.
- [2] A. H. Akselsen. “A linear stability analyses of discrete representations of the two-fluid model for stratified two-phase flow.” In: *ICMF - 9th International Conference on Multiphase Flow, 2016, Firenze, Italy*.
- [3] A. H. Akselsen. “Efficient Numerical Methods for Waves in One-Dimensional Two-Phase Pipe Flows.” PhD thesis. NTNU, 2016.
- [4] J. E. Azpiroz. “CFD modelling of by-pass pigs.” MSc thesis. Delft University of Technology, 2014.
- [5] J. E. Azpiroz, M. H. W. Hendrix, W.-P. Breugem, and R. A. W. M. Henkes. “CFD modelling of bypass pigs with a deflector disk.” In: *17th Int. Conf. on Multiphase Technology* (2015), pp. 141–155.
- [6] D. Barnea and Y. Taitel. “Kelvin-Helmholtz stability criteria for stratified flow: viscous versus non-viscous (inviscid) approaches.” In: *International Journal of Multiphase Flow* 19.4 (1993), pp. 639–649.
- [7] D. Barnea and Y. Taitel. “Interfacial and structural stability of separated flow.” In: *International Journal of Multiphase Flow* 20.94 (1994), pp. 387–414.
- [8] K. Bendiksen, D. Malnes, R. Moe, and S. Nuland. “The dynamic two-fluid model OLGA. Theory and application.” In: *SPE Production Engineering* 6.2 (1991), pp. 171–180.
- [9] R. A. Berry, L. Zou, H. Zhao, H. Zhang, J. W. Peterson, R. C. Martineau, S. Y. Kadioglu, and D. Andrs. *RELAP-7 Theory manual - INL/EXT-14-31366*. 2015.
- [10] D. Biberg. “An explicit approximation for the wetted angle in two-phase stratified pipe flow.” In: *The Canadian Journal of Chemical Engineering* 77.3 (1999), pp. 1221–1224.
- [11] J. C. Butcher. *Numerical Methods for Ordinary Differential Equations*. John Wiley & Sons, Ltd., 2003. ISBN: 9780470868270.
- [12] M. H. P. Carvalho and E. Rotava. “Planning and Execution of Pigging Procedure for Gas Pipeline.” In: *Offshore Technology Conference* 28063 (2017), pp. 1–8.
- [13] S. W. Churchill. “Friction-factor equation spans all fluid flow regimes.” In: *Chem. Eng.* 84 (24) (1977), pp. 91–92.

- [14] J. Cordell. *Conventional pigs - what to use and why*. Pipes and Pipelines International. 1992.
- [15] J. Cordell and H. Vanzant. *The pipeline pigging handbook*. 3rd. ISBN: 0-9717945-3-7. Clarion Technical Publishers & Scientific Surveys Ltd., 2003.
- [16] T. J. Danielson, K. M. Bansal, R. Hansen, and E. Leporcher. "LEDA: the next multiphase flow performance simulator." In: *BHR Group 2005 Multiphase Production Technology 12*. 2005, pp. 477–492.
- [17] R. Davidson. *An introduction to pipeline pigging*. Gulf Professional Publishing, 1995.
- [18] P. G. Drazin. *Introduction to Hydrodynamic Stability*. Cambridge University Press, 2002.
- [19] D. A. Drew and S. L. Passman. *Theory of Multicomponents Fluids*. Springer, 1998. ISBN: 0387983805.
- [20] F.-J. Elmer. "Nonlinear dynamics of dry friction." In: *Journal of Physics A: Mathematical and General* 30.17 (1997), pp. 6057–6063.
- [21] A. Entaban, A. Ismail, M. Jambari, P. Ting, K. M. Amin, C. Ping, S. Zou, and G. van Spronsen. "By-Pass pigging - A 'simple' technology with significant business impact." In: *Society of Petroleum Engineers - International Petroleum Technology Conference 2013, IPTC 2013*. Vol. 5. 2013, pp. 3666–3671.
- [22] F. Esmaeilzadeh, D. Mowla, and M. Asemani. "Mathematical modeling and simulation of pigging operation in gas and liquid pipelines." In: *Journal of Petroleum Science and Engineering* 69.1-2 (2009), pp. 100–106.
- [23] A. B. Figueiredo, R. M. Baptista, F. B. D. Freitas Rachid, and G. C. R. Bodstein. "Numerical simulation of stratified-pattern two-phase flow in gas pipelines using a two-fluid model." In: *International Journal of Multiphase Flow* 88 (2017), pp. 30–49.
- [24] *Fluent Theory Guide*. 14th ed. Ansys Inc.
- [25] W. D. Fullmer, V. H. Ransom, and M. A. Lopez de Bertodano. "Linear and nonlinear analysis of an unstable, but well-posed, one-dimensional two-fluid model for two-phase flow based on the inviscid Kelvin-Helmholtz instability." In: *Nuclear Engineering and Design* 268 (2014), pp. 173–184.
- [26] A. Gent. "On the relation between indentation hardness and Young's modulus." In: *Rubber Chemistry and Technology* 31.4 (1958), pp. 896–906.
- [27] H. Goedecke. "Ultrasonic or MFL Inspection: Which Technology Is Better for You?" In: *Pipeline and Gas Journal* 230 (Oct. 2003), pp. 34–41.

- [28] A. Goldszal, J. I. Monsen, T. J. Danielson, K. M. Bansal, Z. L. Yang, S. T. Johansen, and G. Depay. “LedaFlow 1D: Simulation results with multiphase gas/condensate and oil/gas field data.” In: *13th International Conference on Multiphase Production Technology* (2007), pp. 17–31.
- [29] C. M. Graafland. “Frictional behaviour of pigs.” MSc thesis. Delft University of Technology, 2017.
- [30] G. A. Groote, P. B. J. van de Camp, P. Veenstra, G. Broze, and R. A. W. M. Henkes. “By-pass pigging without or with speed control for gas-condensate pipelines.” In: *Society of Petroleum Engineers - Abu Dhabi International Petroleum Exhibition and Conference, ADIPEC 2015*. 2015.
- [31] E. Hairer, S.P. Norsett, and G. Wanner. *Solving Ordinary Differential Equations I*. Springer, 2008. ISBN: 978-3-540-56670-0.
- [32] A. den Heijer. “Frictional behaviour of pigs in motion.” MSc thesis. Delft University of Technology, 2016.
- [33] M. H. W. Hendrix, I. E. Smith, J. S. B. van Zwieten, and B. Sanderse. “Comparison of numerical methods for slug capturing with the two-fluid model.” In: *ICMF - 9th International Conference on Multiphase Flow 2016, Firenze, Italy*. 2016.
- [34] M. H. W. Hendrix, A. den Heijer, W.-P. Breugem, and R. A. W. M. Henkes. “Frictional forces during pigging of multiphase pipelines.” In: *BHR Group - 10th North American Conference on Multiphase Technology 2016* (2016), pp. 103–114.
- [35] M. H. W. Hendrix, X. Liang, W.-P. Breugem, and R. A. W. M. Henkes. “Characterization of the pressure loss coefficient using a building block approach with application to by-pass pigs.” In: *Journal of Petroleum Science and Engineering* 150 (2017), pp. 13–21.
- [36] M. H. W. Hendrix, H. P. IJsseldijk, W.-P. Breugem, and R. A. W. M. Henkes. “Development of speed controlled pigging for low pressure pipelines.” In: *18th International Conference on Multiphase Production Technology, MPT 2017* 2017-June (2017), pp. 501–509.
- [37] M. H. W. Hendrix, H. P. IJsseldijk, W.-P. Breugem, and R. A. W. M. Henkes. “Experiments and modelling of by-pass pigging under low pressure conditions.” In: *Journal of Process Control* 17 (2018), pp. 1–13.
- [38] M. H. W. Hendrix, H. P. IJsseldijk, W.-P. Breugem, and R. A. W. M. Henkes. “Simulation of slug propagation for by-pass pigging in two-phase stratified pipe flow.” In: *19th Int. Conf. on Multiphase Technology* (2019), pp. 317–330.
- [39] R. A. W. M. Henkes. *Guidelines for the Hydraulic Design and Operation of Multiphase Flow Pipeline Systems*. Shell Global Solutions, 2019.
- [40] C. Hirsch. *Numerical Computation of Internal and External Flows - Volume I, Fundamentals of Numerical Discretization*. Wiley, 1994.

- [41] H. Holmås. “Numerical simulation of transient roll-waves in two-phase pipe flow.” In: *Chemical Engineering Science* 65.5 (2010), pp. 1811–1825.
- [42] S. M. Hosseinalipour, A. Zarif Khalili, and A. Salimi. “Numerical simulation of pig motion through gas pipelines.” In: *16th Australasian Fluid Mechanics Conference*. 2007, pp. 971–975.
- [43] W. Hundsdorfer and J. Verwer. *Numerical Solution of Time-Dependent Advection-Diffusion-Reaction Equations*. Vol. 33. Springer, 2007. ISBN: 978-3-642-05707-6.
- [44] H. P. IJsseldijk. “By-pass pigging - Experiments and simulations.” MSc thesis. Delft University of Technology, 2016.
- [45] I. E. Idelchik. *Handbook of Hydraulic Resistance*. 2nd ed. Hemisphere Publishing Corporation, 1987.
- [46] R. I. Issa and M. H. W. Kempf. “Simulation of slug flow in horizontal and nearly horizontal pipes with the two-fluid model.” In: *International Journal of Multiphase Flow* 29.1 (2003), pp. 69–95.
- [47] B. Jamshidi and M. Sarkari. “Simulation of pigging dynamics in gas-liquid two-phase flow pipelines.” In: *Journal of Natural Gas Science and Engineering* 32 (2016), pp. 407–414.
- [48] G. W. Johnson. “A Study of Stratified Gas-Liquid Pipe Flow.” PhD thesis. University of Oslo, 2005.
- [49] J. Kjølås, A. De Leebeek, and S. T. Johansen. “Simulation of hydrodynamic slug flow using the LedaFlow slug capturing model.” In: *16th International Conference on Multiphase Production Technology, 12-14 June, Cannes, France* (2013).
- [50] K. Kohda, Y. Suzukawa, and H. Furukawa. “New method for analyzing transient flow after pigging scores well.” In: *Oil and Gas Journal* 86.19 (1988), pp. 40–47.
- [51] P. K. Kundu, L. M. Cohen, and D. R. Dowling. *Fluid mechanics*. 5th ed. Academic Press, 2012.
- [52] Z. Lan, S. Liu, H. Xiao, and D. Wang. “Frictional Behavior of Wax–Oil Gels Against Steel.” In: *Tribology Letters* 65.3 (2017), p. 88.
- [53] H. S. Lee, D. Agustawan, K. Jati, M. A. H. Aulia, S. A. Thomas, and S. P. Apleyard. “By-pass pigging operation experience and flow assurance study.” In: *Offshore Technology Conference* (2012), pp. 1–10.
- [54] X. Liang. “Numerical study of flow around by-pass pigs.” MSc thesis. Delft University of Technology, 2015.
- [55] J. Liao, R. Mei, and J. F. Klausner. “A study on the numerical stability of the two-fluid model near ill-posedness.” In: *International Journal of Multiphase Flow* 34.11 (2008), pp. 1067–1087.

- [56] H. Liu. *Pipeline Engineering*. ISBN: 0-58716-140-0. Lewis Publishers, 2003.
- [57] R. W. Lyczkowski, D. Gidaspow, C. W. Solbrig, and E. D. Hughes. “Characteristics and stability analyses of transient one-dimensional two-phase flow equations and their finite difference approximations.” In: *Nuclear Science and Engineering* 66.3 (1978), pp. 378–396.
- [58] C. M. Graafland M. H. W. Hendrix and R. van Ostayen. “Frictional forces during pipeline pigging.” In: *Journal of Petroleum Science and Engineering* 171 (2018), pp. 905–918.
- [59] J. M. Masella, Q. H. Tran, D. Ferre, and C. Pauchon. “Transient simulation of two-phase flows in pipes.” In: *International Journal of Multiphase Flow* 24.5 (1998), pp. 739–755.
- [60] B. S. Massey. *Mechanics of Fluids*. 9th ed. Spon Press, 2012.
- [61] K. Minami and O. Shoham. “Pigging dynamics in two-phase flow pipelines: Experiment and modeling.” In: *SPE Production and Facilities* 10.4 (1995), pp. 225–231.
- [62] M. Mirshamsi and M. Rafeeyan. “Speed control of pipeline pig using the QFT method.” In: *Oil and Gas Science Technology* 67.4 (2012), pp. 693–701.
- [63] N. Money, D. Cockfield, S. Mayo, and G. Smith. “Dynamic speed control in high velocity pipelines.” In: *Pipeline and Gas Journal* 239(8) (2012), pp. 30–38.
- [64] M. Montini. “Closure Relations of the One-Dimensional Two-Fluid Model for the Simulation of Slug Flows.” PhD thesis. Imperial College, 2011.
- [65] A. Morin, T. Flåtten, and S. T. Munkejord. “A Roe scheme for a compressible six-equation two-fluid model.” In: *International Journal for Numerical Methods in Fluids* 72 (2013), pp. 478–504. DOI: 10.1002/fluid.
- [66] K.W. Morton and D. Mayers. *Numerical Solution of Partial differential Equations*. Cambridge University Press, 2005. ISBN: 9780521607933.
- [67] T. T. Nguyen, S. B. Kim, H. R. Yoo, and Y. W. Rho. “Modeling and simulation for PIG with bypass flow control in natural gas pipeline.” In: *KSME International Journal* 15.9 (2001), pp. 1302–1310.
- [68] T. T. Nguyen, H. R. Yoo, Y. W. Rho, and S. B. Kim. “Speed control of pig using bypass flow in natural gas pipeline.” In: *IEEE International Symposium on Industrial Electronics* 2 (2001), pp. 863–868.
- [69] A. O. Nieckele, A. M. B. Braga, and L. F. A. Azevedo. “Transient pig motion through gas and liquid pipelines.” In: *Journal of Energy Resources Technology, Transactions of the ASME* 123.2-4 (2001), pp. 260–268.
- [70] A. F. O’Donoghue. “On the steady motion of conventional pipeline pigs using incompressible drive media.” PhD thesis. Cranfield University, 1996.

- [71] R. Olsen. “Time Dependent Boundary Conditions for Multiphase Flow.” PhD thesis. NTNU, 2004.
- [72] B. N. J. Persson. *Sliding Friction*. ISBN: 3-540-63296-4. Springer, 1998.
- [73] A. Prosperetti and G. Tryggvason. *Computational Methods for Multiphase Flow*. Cambridge University Press, 2007. ISBN: 9780521847643.
- [74] J. Quarini and S. Shire. “A review of fluid-driven pipeline pigs and their applications.” In: *Journal of Process Mechanical Engineering* 221.1 (2007), pp. 1–10.
- [75] C. Ramella et al. “A novel smart caliper foam pig for low-cost pipeline inspection - Part B: Field test and data processing.” English. In: *Journal of Petroleum Science and Engineering* 133 (2015), pp. 771–775.
- [76] J. D. Ramshaw and J. A. Trapp. “Characteristics, stability, and short-wavelength phenomena in two-phase flow equation systems.” In: *Nuclear Science and Engineering* 66 (1978), pp. 93–102.
- [77] B. W. Righolt, S. Kenjereš, R. Kalter, M. J. Tummers, and C. R. Kleijn. “Dynamics of an oscillating turbulent jet in a confined cavity.” In: *Physics of Fluids* 27 (2015).
- [78] Z. Rui, G. Han, H. Zhang, S. Wang, H. Pu, and K. Ling. “A new model to evaluate two leak points in a gas pipeline.” In: *Journal of Natural Gas Science and Engineering* 46.36 (2017), pp. 491–497.
- [79] Z. Rui, X. Wang, Z. Zhang, J. Lu, G. Chen, X. Zhou, and S. Patil. “A realistic and integrated model for evaluating oil sands development with Steam Assisted Gravity Drainage technology in Canada.” In: *Applied Energy* 213.7 (2018), pp. 76–91.
- [80] B. Sanderse, I. E. Smith, and M. H. W. Hendrix. “Analysis of time integration methods for the compressible two-fluid model for pipe flow simulations.” In: *International Journal of Multiphase Flow* 95 (2017), pp. 155–174.
- [81] H. J. Sheen, W. J. Chen, and J. S. Wu. “Flow patterns for an annular flow over an axisymmetric sudden expansion.” In: *Journal of Fluid Mechanics* 350 (1997), pp. 177–188.
- [82] A. Singh and R. A. W. M. Henkes. “CFD modelling of the flow around a bypass pig.” In: *8th North American Conference on Multiphase Technology* (2012), pp. 229–243.
- [83] H. B. Stewart and B. Wendroff. “Two-phase flow: models and methods.” In: *Journal of Computational Physics* 56 (1984), pp. 363–409.
- [84] G.-B. Tan, D.-G. Wang, S.-H. Liu, and S.-W. Zhang. “Frictional behaviors of rough soft contact on wet and dry pipeline surfaces: With application to deepwater pipelaying.” In: *Science China Technological Sciences* 56 (2013), pp. 3024–3032.

- [85] G.-B. Tan, D.-G. Wang, S.-H. Liu, and S.-W. Zhang. “Probing tribological properties of waxy oil in pipeline pigging with fluorescence technique.” In: *Tribology International* 71 (2014), pp. 26–37.
- [86] G.-B. Tan, S.-H. Liu, D.-G. Wang, and S.-W. Zhang. “Spatio-temporal structure in wax-oil gel scraping at a soft tribological contact.” In: *Tribology International* 88 (2015), pp. 236–251.
- [87] R. G. Teyssandier and M. P. Wilson. “An analysis of flow through sudden enlargements in pipes.” In: *Journal of Fluid Mechanics* 64.1 (1974), pp. 85–95.
- [88] K. W. Thompson. “Time dependent boundary conditions for hyperbolic systems.” In: *Journal of Computational Physics* 68.1 (1987), pp. 1–24.
- [89] U. Thuenemann and J. Wegjan-Kuipers. “Control your speed.” In: *World Pipelines* 3(3) (2003), pp. 31–32.
- [90] J. N. H. Tiratsoo. *Pipeline pigging technology*. 2nd. ISBN: 0-8720142-6-6. Gulf Professional Publishing, 1992.
- [91] S. T. Tolmasquim and A. O. Nieckele. “Design and control of pig operations through pipelines.” In: *Journal of Petroleum Science and Engineering* 62.3-4 (2008), pp. 102–110.
- [92] M. J. Tummers, A. W. Hübner, E. H. van Veen, K. Hanjalić, and Th H. van der Meer. “Hysteresis and transition in swirling nonpremixed flames.” In: *Combustion and Flame* 156.2 (2009), pp. 447–459.
- [93] K. P. Vanoverberghe, E. V. van den Bulck, and M. J. Tummers. “Confined annular swirling jet combustion.” In: *Combustion Science and Technology* 175.3 (2003), pp. 545–578.
- [94] Q. Wang, C. Sarica, and M. Volk. “An experimental study on wax removal in pipes with oil flow.” In: *Journal of Energy Resources Technology, Transactions of the ASME* 130.4 (2008), pp. 0430011–0430015.
- [95] M. White, K. Pierce, and T. Acharya. “A Review of Wax-Formation/Mitigation Technologies in the Petroleum Industry.” In: *Society of Petroleum Engineers* 189447 (2017), pp. 1–10.
- [96] H. L. Wu and G. van Spronsen. “Slug reduction with high by-pass pigs - a mature technology.” In: *12th International Conference on Multiphase Production Technology, Barcelona* (2005), pp. 313–325.
- [97] X.-X. Xu and J. Gong. “Pigging simulation for horizontal gas-condensate pipelines with low-liquid loading.” In: *Journal of Petroleum Science and Engineering* 48.3-4 (2005), pp. 272–280.

- [98] H. Zhang, C. Sanchez, S. Liu, S. Zhang, and H. Liang. “Wear of a polyurethane rubber used in dry gas pipeline as inspection gauges.” In: *Journal of Natural Gas Science and Engineering* 41 (2017), pp. 40–48.
- [99] X. Zhu, D. Wang, H. Yeung, S. Zhang, and S. Liu. “Comparison of linear and non-linear simulations of bidirectional pig contact forces in gas pipelines.” In: *Journal of Natural Gas Science and Engineering* 27 (2015), pp. 151–157.
- [100] X. Zhu, S. Zhang, X. Li, D. Wang, and D. Yu. “Numerical simulation of contact force on bi-directional pig in gas pipeline: At the early stage of pigging.” In: *Journal of Natural Gas Science and Engineering* 23 (2015), pp. 127–138.
- [101] X. Zhu, W. Wang, S. Zhang, and S. Liu. “Experimental Research on the Frictional Resistance of Fluid-Driven Pipeline Robot with Small Size in Gas Pipeline.” In: *Tribology Letters* 65.2 (2017).
- [102] L. Zou, H. Zhao, and H. Zhang. “Applications of high-resolution spatial discretization scheme and Jacobian-free Newton-Krylov method in two-phase flow problems.” In: *Annals of Nuclear Energy* 83 (2015), pp. 101–107.
- [103] J. S. B. van Zwieten, B. Sanderse, M. H. W. Hendrix, C. Vuik, and R. A. W. M. Henkes. *Efficient simulation of one-dimensional two-phase flow with a new high-order Discontinuous Galerkin method, Report 15-07*. Tech. rep. Delft University of Technology, 2015.

ACKNOWLEDGMENTS

First of all I would like to thank my promotor Ruud Henkes for giving me the opportunity to embark on this exciting project. The combination of fundamental research with a clear practical application provided an interesting project to work on. You helped me to apply the right focus to take all the steps that are needed to finish a PhD project: from writing up the very first results in a paper, to keeping me motivated until the very end when I was writing the draft of this thesis. I also would like to thank you for the very fast and detailed feedback on my draft papers and thesis chapters, which usually took no longer than a day or two!

I would like to thank my daily supervisor and promotor Wim-Paul Breugem. You always take enough time during scientific discussions to thoroughly analyze a problem to the very core. This is a quality that I greatly appreciated in working together. I also enjoyed assisting in the turbulence course that you lectured - a course that is very well received by students. I quickly understood why!

I would like to thank both my promotors for having the patience with me to complete all the chapters and papers which are part of this thesis. I want to emphasize that I appreciate the constructive and inspiring conversations we have had, which have led to the sharpening and completion of this thesis.

During my PhD I had the pleasure to share an office with Andries and Daniele, and later on also Tariq. Thanks for the fun moments we have had! I also would like to thank all other lab members for providing a very nice working environment. In particular I enjoyed the Christmas festivities and of course the group outings that were organized by the laboratory. I would also like to thank the *GoT* group for many very well organized movie nights!

The PhD project has been carried out in collaboration with Shell. I regularly visited Shell Technology Centre Amsterdam. I would like to thank Peter Veenstra, who was closely involved during the course of this project and has continuously provided valuable practical feedback. Also I would like to give a big thanks to the involvement of various people from the Flow Assurance team in Shell. In particular, I would like to thank Benjamin Sanderse. Our paths crossed early on and it was a pleasure to work on our joint publications. I learnt a lot from your rigorous mathematical approach, and your two-fluid model solver was the starting point for the numerical simulations that led to the results of chapter 5 and 6. Also I would like to thank Gijs Groote and Maurice Fransen for their involvement regarding the practical implications of this work.

I would like to thank Ivar Smith and Joost van Zwieten for pleasant collaboration on our joint publications.

I want to thank Caroline for all the administrative support during my PhD.

I have had the pleasure to work with five master students: Javier, Xiaoyun, Arie, Harm, Chris, your work has all contributed to this thesis and I am grateful for that. I also had the pleasure to work with four bachelor students for their final project. Your project stood out, as it had created some very visible results. Thanks, Daan, Luuk, Sytse, and Tim! I would like to thank Jasper and Jan for supporting the experiments which were part of the student projects.

A final word of gratitude goes to my family and friends and my girlfriend Roza for their continuous support!

Maurice Hendrix
Delft, August 2019

CURRICULUM VITÆ

PERSONAL INFORMATION

FULL NAME: Maurice Hans Willem Hendrix

BIRTH DATE: 30 September 1988

NATIONALITY: Dutch

EDUCATION AND EMPLOYMENT

2017-NOW: Instrumentation Engineer, Shell Pernis, The Netherlands.

2013-2017: PhD Researcher in the Laboratory for Hydro & Aerodynamics,
Process & Energy Department, Delft University of Technology, The Netherlands.

2011-2013: MSc in Applied Physics, Universiteit Twente, The Netherlands;
Exchange Student, Nanyang Technological University, Singapore (in 2011, for four
months).

2007-2011: BSc in Applied Physics, Universiteit Twente, The Netherlands.

LIST OF PUBLICATIONS

JOURNAL PUBLICATIONS

- [1] M.H.W. Hendrix, H.P. IJsseldijk, W.-P. Breugem, and R.A.W.M. Henkes, "Experiments and modelling of by-pass pigging under low pressure conditions.", *Journal of Process Control*, vol. 71, pp. 1-13, 2018.
- [2] M.H.W. Hendrix, C.M. Graafland, and R. van Ostayen, "Frictional forces for disc-type pigging of pipelines.", *Journal of Petroleum Science and Engineering*, vol. 171, pp. 905-918, 2018.
- [3] B. Sanderse, I.E. Smith, and M.H.W. Hendrix, "Analysis of time integration methods for the compressible two-fluid model for pipe flow simulations.", *International Journal of Multiphase Flow*, vol. 95, pp. 155-174, 2017.
- [4] M.H.W. Hendrix, X. Liang, W.-P. Breugem, and R.A.W.M. Henkes, "Characterization of the pressure loss coefficient using a building block approach with application to by-pass pigs.", *Journal of Petroleum Science and Engineering*, vol. 150, pp. 13-21, 2016.

CONFERENCE PUBLICATIONS AND CONTRIBUTIONS

- [1] M.H.W. Hendrix, B. Sanderse, W.-P. Breugem, and R.A.W.M. Henkes, "Simulation of slug propagation for by-pass pigging in two-phase stratified pipe flow.", *BHR Group - 19th International Conference on Multiphase Technology*, pp. 317-330, 2019.
- [2] M.H.W. Hendrix, H.P. IJsseldijk, W.-P. Breugem, and R.A.W.M. Henkes, "Development of speed controlled pigging for low pressure pipelines.", *BHR Group - 18th International Conference on Multiphase Technology*, pp. 501-509, 2017.
- [3] M.H.W. Hendrix, A. den Heijer, W.-P. Breugem, and R.A.W.M. Henkes, "Frictional forces during pigging of multiphase pipelines.", *BHR Group - 10th North American Conference on Multiphase Technology*, pp. 103-114, 2016.
- [4] J.E. Azpiroz, M.H.W. Hendrix, W.-P. Breugem, and R.A.W.M. Henkes, "CFD modelling of bypass pigs with a deflector disk.", *BHR Group - 17th International Conference on Multiphase Technology*, pp. 141-158, 2015.

JOURNAL PUBLICATIONS OUTSIDE THIS THESIS

- [1] J.S.B van Zwieten, B. Sanderse, M.H.W. Hendrix, C. Vuik, and R.A.W.M. Henkes, "Efficient simulation of one-dimensional two-phase flow with a high-order h-adaptive space-time Discontinuous Galerkin method.", *Computer and Fluids*, vol. 156, pp. 34-47, 2017.
- [2] M.H.W. Hendrix, W. Bouwhuis, D. van der Meer, D. Lohse, and J.H. Snoeijer, "Universal mechanism for air entrainment during liquid impact.", *Journal of Fluid Mechanics*, vol. 789, pp. 708-725, 2016.
- [3] W. Bouwhuis, M.H.W. Hendrix, D. van der Meer, and J.H. Snoeijer, "Initial surface deformations during impact on a liquid pool.", *Journal of Fluid Mechanics*, vol. 771, pp. 503-519, 2015.
- [4] E. Klaseboer, R. Manica, M.H.W. Hendrix, C.-D. Ohl, and D.Y.C. Chan, "A force balance model for the motion, impact, and bounce of bubbles.", *Physics of Fluids*, vol. 26, pp. 092101-01 - 092101-12, 2014.
- [5] R. Manica, M.H.W. Hendrix, R. Gupta, E. Klaseboer, C.-D. Ohl, and D.Y.C. Chan, "Modelling bubble rise and interaction with a glass surface.", *Applied Mathematical Modelling*, vol. 38, pp. 4249-4261, 2014.
- [6] R.C.A. van der Veen, M.H.W. Hendrix, T. Tran, C. Sun, P.A. Tsai, and D. Lohse, "How microstructures affect air film dynamics prior to drop impact.", *Soft Matter*, vol. 10, pp. 3703-3707, 2014.
- [7] R. Manica, M.H.W. Hendrix, R. Gupta, E. Klaseboer, C.-D. Ohl, and D.Y.C. Chan, "Effect of film hydrodynamic boundary condition on bubble-wall impact.", *Soft Matter*, vol. 9, pp. 9755-9758, 2013.
- [8] M.H.W. Hendrix, R. Manica, E. Klaseboer, D.Y.C. Chan, and C.-D. Ohl, "Spatiotemporal evolution of thin liquid films during impact of water bubbles on glass on a micrometer to nanometer scale.", *Physical Review Letters*, vol. 108, pp. 247803-01 - 247803-04, 2012.
- [9] P.A. Tsai, M.H.W. Hendrix, R.R.M. Dijkstra, L. Shui, and D. Lohse, "Microscopic structure influencing macroscopic splash at high Weber number.", *Soft Matter*, vol. 7, pp. 11325-11333, 2011.